Aix Marseille Université
Institut Fresnel
École Doctorale 352: Physique et sciences de la matière

Endoscopie non-linéaire : instrumentation et applications

Thèse pour obtenir le grade universitaire de docteur
Discipline : Optique, photonique et traitement d'image
Présentée par:

Vasyl MYTSKANIUK

Soutenue le 19 Décembre 2018 devant le jury :

Marloes GROOT	Vrije Universiteit, Amsterdam	Rapporteuse
Andreas ZUMBUSCH	Universität Konstanz	Rapporteur
Alexandre KUDLINSKI	Université de Lille	Examinateur
Frédéric LOURADOUR	Université de Limoges	Examinateur
Hervé RIGNEAULT	Institut Fresnel	Directeur de thèse
Rosa COSSART	Institut de neurobiologie de la méditeranée	Co-directrice de thèse

Aix Marseille University
Fresnel Institute
Doctoral school 352: Physics and science of matter

Nonlinear endoscopy : instrumentation and applications

A thesis submitted for the degree of Doctor of Philosophy
Specialty: Optics, photonics and image processing
Defended on the 19th of December 2018 by:

Vasyl MYTSKANIUK

Defense commitee:

Marloes GROOT	Vrije Universiteit, Amsterdam	Reviewer
Andreas ZUMBUSCH	Universität Konstanz	Reviewer
Alexandre KUDLINSKI	Université de Lille	Examiner
Frédéric LOURADOUR	Université de Limoges	Examiner
Hervé RIGNEAULT	Institut Fresnel	Supervisor
Rosa COSSART	Institut de neurobiologie de la méditeranée	Co-supervisor

PUBLICATIONS

- A. Lombardini, V. Mytskaniuk, S. Sivankutty, E. R. Andresen, X. Chen, J. Wenger, M. Fabert, N. Joly, F. Louradour, A. Kudlinski, and H. Rigneault, "High-resolution multimodal flexible coherent Raman endoscope", Light: Science & Applications 7, 10 (2018).
- V. Mytskaniuk, A. Lombardini, M. Fabert, F. Louradour, A. Kudlinski, F. Rigneault, "Multimodal flexible endoscope using a negative curvature hollow core fiber", in preparation.
- V. Mytskaniuk, A. Lombardini, M. Fabert, F. Louradour, A. Kudlinski, M. Picardo, R. Cossart, F. Rigneault, "In vivo miniature flexible two-photon endoscope for brain activity recording", in preparation.

Related work (not presented in this PhD manuscript):

- Mytskaniuk, V., Bardin, F., Boukhaddaoui, H., Rigneault, H., Tricaud, N. "Implementation of a Coherent Anti-Stokes Raman Scattering (CARS) System on a Ti: Sapphire and OPO Laser Based Standard Laser Scanning Microscope". J. Vis. Exp. (113), e54262, doi: 10.3791/54262 (2016).

CONFERENCES

- Vasyl Mytskaniuk, Alberto Lombardini, Xueqin Chen, Siddharth Sivankutty, Jérôme Wenger, Rémi Habert, Coralie Fourcade-Dutin, Esben Ravn Andresen, Alexandre Kudlinski et Hervé Rigneault. Developement d'un endoscope pour l'imagerie Raman cohérente. Journées Nationales d'Optique Guidée (JNOG). Bordeaux, 2016.
- Vasyl Mytskaniuk, Alberto Lombardini, Xueqin Chen, Siddharth Sivankutty, Jérôme Wenger, Marc Fabert, Esben Ravn Andresen, Frédéric Louradour, Alexandre Kudlinski et Hervé Rigneault. Endomicroscope non-linéaire multimodale utilisant des fibres à coeur d'air. Journées Nationales d'Optique Guidée (JNOG). Limoges, 2017.
- Vasyl Mytskaniuk, Alberto Lombardini, Xueqin Chen, Siddharth Sivankutty, Jérôme Wenger, Marc Fabert, Esben Ravn Andresen, Frédéric Louradour, Alexandre Kudlinski et Hervé Rigneault. CARS endoscopy using hollow core fibers. Focus On Microscopy (FOM). Bordeaux, 2017.
- Vasyl Mytskaniuk, Alberto Lombardini, Xueqin Chen, Siddharth Sivankutty, Esben Ravn Andresen, Jérôme Wenger, Marc Fabert, Nicolas Joly, Frédéric Louradour, Alexandre Kudlinski et Hervé Rigneault. High resolution multimodal flexible coherent Raman endoscope. Photonics West. San-Francisco, 2018.
- Vasyl Mytskaniuk, Alberto Lombardini, Xueqin Chen, Siddharth Sivankutty, Esben Ravn Andresen, Jérôme Wenger, Marc Fabert, Nicolas Joly, Frédéric Louradour, Alexandre Kudlinski et Hervé Rigneault. High-resolution multimodal flexible miniaturized endoscope for non-linear imaging. Photonics West. San-Francisco, 2019.

To my mother

ACKNOWLEDGEMENTS

This thesis reports the work which was carried out in Aix-Marseille University at Institute Fresnel from November 2015 till December 2018.

I was a master student finishing Europhotonics program, when I first met my supervisor. That time this was my master's thesis internship which I did in Montpelier collaborating with the MOSAIC group led by Hervé Rigneault. I had never thought that one day I would become a doctor of philosophy or a doctor of anything...These thoughts, however, started to change when seeing doctoral students working on very interesting projects at Fresnel Institute. So, when I got a proposal from Hervé to apply for a PhD position, I gladly accepted it.

Time passes very fast, so soon after the beginning I am already writing my acknowledgements...Here I would like to thank the people without whom my PhD degree would have not become true. First of all, it is my supervisor Hervé Rigneault. Right on the first day he stroke me with his energy, motivation and curiosity for science. From the very first day of my PhD journey, Hervé has been a patient mentor, expressing only positive vibes, seeing only good things in my sometimes very modest results and achievements. His optimism has been always pushing me forward to work harder and become who I want to be.

Alberto Lombardini. The first thing which I always recall is his charming and friendly smile. Alberto has introduced me to his little world of nonlinear endoscopy that he had created. He has not only showed me how to cleave fibers and make samples, and how to treat images and program in LabView, but he has become my first role model for a scientist.

Victor Tsvirkun and Sid Sivankutty. Those are our amazing postgods. I cannot call them differently as they pretend to have understood the true meaning of life – research. With them I had the pleasure to share the lab and my life. This is because they have been an important part of it, either during working hours (if such exist in the burden of a PhD student) or beyond Fresnel's Institute.

Marc Fabert and Frédéric Louradour. I want to express my gratitude to these people for their collaboration in endoscope probes assembling. With their experience in the domain of scanning endoscopy, they made the course of our work much more efficient, and thus improved the final results. Besides, I particularly enjoyed coming to Limoges and to XLIM Institute with a very friendly atmosphere and hospitable people.

I would like to thank Alex Kudlinski and Damien Labat for their amazing fibers and for the work we did together. In this three years our collaboration with IRCICA Institute has been very fruitful. Let it continue like that.

I cannot forget here my co-supervisor Rosa Cossart, director of INMED Instute, as well as Thomas Tressard, Michel Picardo and Sophie Brustlein. We have had an exciting time working together on in-vivo measurements of calcium flow in mouse hippocampus.

I would like to say thank you to Barbara Sarri for the tissue samples she was providing us

and for her valuable advises.

Simon, Camille, Hadrien, Matthias, Sandro and Caio, Misha, Sasha, Elena - for they humour and support. Xavier, my frère, we made it! I hope you still remember that important Ukrainian and Russian phrases I taught you.

Naveen, Hilton, Juan, Satish, Simona, Raju, Johan, Susmita..all those people have already left Fresnel, but they all must be mentioned here, as they all made my PhD study easier, funnier and cooler. They made my life spicier...oh, I remember that food Satish used to make for us.

Finally, my dear girlfriend. Oksana, I have to thank you a million times for you love, patience and belief.

Contents

Introduction

In the last 20 years, the field of nonlinear optical microscopy (NLOM) has developed significantly. With the emergence of stable and versatile pulsed laser sources, generating ultrashort pulses ($10^{-12} - 10^{-13}$ s), it has become possible to excite different nonlinear contrasts and even combine them in a single setup. High peak power ultrashort pulses are required to provide a dense flux of photons needed to efficiently excite nonlinear processes and retain low average power to avoid photo-bleaching and sample damage. Such NLOM techniques as 2-photon excitation fluorescence (TPEF), second and third harmonic generation (SHG and THG) and coherent Raman scattering (CRS) have overcome the conventional wide field (WF) and confocal microscopy. Besides high spatial resolution, these nonlinear contrasts using IR beams provide intrinsic axial sectioning, deeper penetration depths (TPEF, SHG, THG) and chemical specificity (CRS).

Many endogenous fluorescent markers akin elastin and flavoproteins are naturally present in cells and tissues, thus enabling label-free TPEF imaging. Collagen type I residing abundantly in the connective tissue, emits a strong SHG radiation. Coherent anti-Stokes Raman and stimulated Raman scattering (CARS and SRS) imaging allows chemical selectivity and have been successfully applied for the visualisation of lipids in cells and tissues due to the resonant Raman response of CH_2 vibration bond. Recently NLOM proved to be a possible alternative to traditional histology cancer optical imaging and diagnostics.

The availability of Green Fluorescent Protein (GFP) facilitates tissue staining and offers a large variety of fluorescent markers. Genetically encoded calcium indicators in combination with TPEF microscopy have enabled high resolution, deep penetration optical imaging of mouse brain. However, the penetration depth of TPEF is still limited by tissue scattering and absorption ($\sim$200-300 μm), and does not allow to image deep in the mouse hippocampus. Alternatively, 3-photon excitation (3PE) has demonstrated unprecedented depths of the order of 1 mm. Although with appealing benefits, TPEF and 3PE fluorescence microscopy requires head-fixed and/or anaesthetized mouse conditions. Most of the hippocampus function discoveries have been done in head-restrained mice. Most of hippocampal neurons activity recording in freely behaving animals has so far been performed with one photon excitation (OPE) miniaturized GRIN lens microscopes and there is just a recent work which reports brain activity imaging using

a miniature TPEF microscope. TPEF fibered devices for the recording of hippocampal neurons activity should allow stable and reliable imaging, and are expected to lead to new discoveries of the brain function.

There is a necessity of a miniature, portable probe capable to perform fast, high resolution, multimodal imaging for the translation of NLOM to hospitals and biomedical laboratories. The main challenge lies in the delivery of ultrashort pulses via optical fibers. Conventional solid core fibers induce temporal and spectral effects to the ultrashort pulse profile, which in turn degrades the nonlinear excitation efficiency. There exist different pre-compensation schemes which keep the pulses short, however these methods are limited to a very narrow operational bandwidth. Moreover, a strong four wave mixing (FWM) spurious background is generated in the fiber silica core, which overwhelms the CARS signal coming from the sample. All of this presents a complex obstacle for the development of a nonlinear, multimodal fiber-coupled endoscope.

The invention of photonic crystal fibers (PCF) has revolutionized the concept of ultrashort pulse delivery. First of all because of the possibility to transfer high peak power pulses of a short duration without temporal and spectral broadening. PCFs are composed of a hollow core surrounded by a silica structure with air holes. Using Kagomé lattice fibers, the lowloss transmission spectral bandwidth has been extended to some 500-600 nm. We will show in this PhD work that the nonlinear effects generated in the fiber HC are three orders lower than in conventional solid core fibers because it is mostly filled with air, thus the CARS nonresonant background from Kagomé fibers becomes negligible. An additional pure silica double-clad (DC) can be fabricated around the air-filled silica structure, to enable the collection of the back-scattered signal generated by nonlinear contrasts.

A new type of HC-PCFs based on antiresonance reflection (AR) and inhibited coupling (IC) between the core and clad modes, has recently drawn a particular attention. This HC fiber with a modified design as compared to Kagomé fibers, has only one ring of silica tubes instead of the complex Kagomé structure. The tubes curvature is pointed inward, therefore this HC-fiber has been called negative curvature fiber (NCF). Such optical fiber is easier to fabricate thanks to its simple design. In this work, we have designed and fabricated HC-PCFs with tailored NCF core transmission window to perform TPEF and CARS endoscopy. Moreover, using the same strategy as for Kagomé fibers, we have fabricated NCFs featuring a double cladding for an efficient NLO signal collection.

A significant part of the work has been to integrate the new NCF into a fast scanning (8 frames/sec), flexible, miniaturized (2.2 mm diameter, 40 mm rigid length) portable probe. The beam scanning mechanism is based on the resonant spiral motion of the fiber free-standing tip threaded through a piezo-electric tube. We have demonstrated the applicability of the NCF endoscope for *in-vivo* TPEF calcium indicators imaging of hippocampal neurons in transgenic mice. Along with demonstrated TPEF, we have shown the capability of the NCF endoscope to perform CARS and SHG label-free inspection of fresh tissues *ex-vivo*. The multimodality with

high scanning speed in combination with the miniature size make the NCF-coupled endoscope a truly unique device for nonlinear imaging of live specimens.

This manuscript is organized as follows:

- **Chapter 1**: In this chapter we introduce the field of NLOM and its advantages for live cells imaging as compared to conventional optical microscopy. We discuss the origin of nonlinear optical effects which occur in presence of high intensity radiation. We describe the basic principles of TPEF, SHG, CARS nonlinear contrasts and their applications for advanced biomedical imaging. In the last section, we initiate the discussion on nonlinear endoscopy and consider the issue of ultrashort pulse delivery through solid-core optical fibers.

- **Chapter 2**: We first review the challenges of CARS micro-endoscopy and the state-of-art methods to improve the performance of such devices. After a brief description of typical scanning-tip endoscope probes, we present our CARS setup which is based on a Kagomé fiber. We introduce the Kagomé fibers and characterize a specifically designed hollow-core DC-Kagomé fiber for ultrashort pulse delivery. The fiber hollow core with an NA of 0.02 is combined with a 30 μm silica microsphere, providing a tight focal spot (1.2 μm) at the fiber exit. We show a custom-designed mini-objective lens based on four achromatic doublets, which relays the focal spot from the fiber end onto the sample. We demonstrate the capability of a scanning-tip, Kagomé fiber based endoscope to perform high contrast CARS and SHG imaging of fresh, unstained tissues. We conclude discussing possible improvements of the Kagomé fiber design to increase the signal collection, especially for TPEF coming from GFP-labelled tissues.

- **Chapter 3**: We present a new class of hollow-core fibers called negative curvature fiber (NCF). We describe its working principle based on inhibited coupling between the fiber core mode and the clad modes, and on destructive interference between the reflected and transmitted waves at the fiber core boundary. A study on ultrashort pulse delivery including FWM background generation, is also carried out in this chapter. We conclude with a comparison of the signal collection efficiency achievable with the DC-NCF and the DC-Kagomé fiber.

- **Chapter 4**: We employ the NCF presented in Ch.3 for the implementation of a new high speed hollow-core endoscope. This chapter is devoted to a detailed description of the mechanical properties and behaviour of the NCF fixed at one side in the piezo-element and with a free-standing tip resonantly scanned by the piezo in a spiral pattern. We develop and exploit an active resonant braking of the fiber tip motion to reduce the period of the fiber free relaxation and minimize the time between two successive scan cycles, thus

increasing the imaging rate. Lastly, we describe the custom-written software for signal acquisition, display and image reconstruction, as well as the dedicated hardware.

- **Chapter 5**: We show a protocol for the integration of the NCF endoscope described in Ch.4 in a flexible, miniaturized probe with a 2-times thinner distal part as compared to the Kagomé one. We use a CO_2 laser to seal the focusing microsphere to the fiber core output facet and describe possible constraints during the probe assembly. The performance of the assembled probe is verified on calibrated samples, and by CARS imaging of polystyrene beads and ex-vivo mouse spinal cord.

- **Chapter 6**: We describe the application of the NCF endoscope for in-vivo TPEF imaging of GFP-labelled neurons in the mouse hippocampus. In the perspective of the neuronal circuits activity recording in freely-behaving mice, we address the principle demands for robustness, stability and imaging performance of a miniature endoscope. In this chapter we perform time-lapsed TPEF imaging of a group of hippocampal neurons and measure the signal intensity change with time. Raw TPEF images acquired at 8 frames/sec are analysed and the corresponding time traces are shown.

Chapter 1

Nonlinear optical microscopy : transfer into endoscopy

This chapter, broken in two parts, will deal with the basic principles of nonlinear optics processes which lead to very interesting phenomena used in nonlinear optical microscopy (NLOM). In Sec.1.1, we will briefly discuss the nature of the nonlinear light-matter interaction with the consequences on resulting optical properties. The need to use ultrashort pulses for nonlinear excitation challenges the translation of NLOM to endoscopy through optical fiber and will be addressed in Sec.1.2.

1.1 Nonlinear microscopy

Applications of optics and photonics in biology and medicine have led to a new branch of science called biophotonics. Lasers in combination with a variety of other optoelectronic devices have been a powerful tool for observing and modifying biological processes, occurring in cells of either living organisms or cultivated specimens. Microscopes have shown their important role in cell studies. Nowadays, it is hard to imagine a biomedical research lab without a microscope. Over the last years, the majority of biological studies and discoveries have been done in cultured specimens. However, in order to investigate true biological dynamic changes in cells, their functionality as whole living systems, live imaging methods have emerged to be of high importance.

Such a well-known microscopy technique as laser scanning confocal microscopy appears to be hardly applicable for deep penetration live cells imaging because of its high excitation energy and short wavelengths applied to a specimen, thus leading to photo-bleaching of the specimen and strong scattering by tissues [1]. Alternatively, two-photon excitation fluorescence (TPEF) microscopy has been introduced as a good solution for live cell imaging [2]. This type of microscopes, based on the nonlinear nature of multi-photon absorption, allows a sub-micron

resolution. Also, there is no need for the pinholes, since the TPEF signal is uniquely generated from focal volume, thus providing intrinsic sectioning. Furthermore, due to longer excitation wavelengths, the penetration depth is increased significantly. Many endogenous fluorophores (keratine, elastin, NAD(P)H, flavoproteins) present in cells and tissues enable label-free imaging.

However, TPEF microscopy as all fluorescence based imaging techniques, often requires specific staining of specimens. Dyes may cause photo-toxicity and induce harm to the specimen. Moreover, labelling is time consuming and depends on the suitable fluorophores availability. Recently, due to the discovery of Green Fluorescent Protein (GFP), fluorescent staining has become much easier to perform [3]. However, for some purposes scientists prefer to have other methods that do not require labelling. As an example, several of them can be named: second and third harmonics generation (SHG, THG) developed for clinical imaging, based on nonlinear properties of certain materials; stimulated Raman scattering (SRS) and coherent anti-Stokes Raman scattering (CARS) spectroscopy which exploit the molecular vibrations in cells and tissues [4–10]. The majority of important advantages of CARS over SHG and THG lie in the ability of CARS to provide molecular specificity at low average power applied to specimens.

1.1.1 Nonlinear behaviour of light

Optical properties of a medium depend on the relation between the electric field $\vec{E}$ and the electric polarization $\vec{P}$. Positive and negative charges are organized in a certain manner by an applied electric field $\vec{E}$. This organization defines the behaviour of light in irradiated media. In a linear medium, the relation between $\vec{E}$ and $\vec{P}$ is considered to be linear. A linear superposition of two different electric fields $b_1\vec{E}_1 + b_2\vec{E}_2$ creates a polarization pair $b_1\vec{P}_1 + b_2\vec{P}_2$. However, in presence of high intensity fields, the linear dependence does not hold anymore. The relationship between the electric field and polarization becomes nonlinear. As a result, new optical phenomena can occur in nonlinear media.

The material response is described by its susceptibility χ, which relates the electric field and the polarization. For a homogeneous, isotropic medium the instantaneous linear polarization P_{L} can be expressed as,

$$P_{\mathrm{L}}(z,t) = \epsilon_0 \chi^{(1)} E(z,t) \tag{1.1}$$

where $\chi^{(1)}$ is the first order susceptibility with E for the electric field. The total polarization can be given by the equation:

$$P(z,t) = P_{\mathrm{L}}(z,t) + P_{\mathrm{NL}}(z,t) \tag{1.2}$$

where the nonlinear polarization contribution $P_{\mathrm{NL}}(z,t)$ can be further expanded to:

$$P_{\mathrm{NL}}(z,t) = \epsilon_0 \chi^{(2)} E^2(z,t) + \epsilon_0 \chi^{(3)} E^3(z,t) + ... \tag{1.3}$$

where $\chi^{(2)}$, $\chi^{(3)}$ and further are the material susceptibilities of the second order, third order and

so on.

Each nonlinear medium characterized by its order of nonlinearity (nonlinear polarization) is responsible for the generation of new spectral components. SHG, for instance, can occur only in nonlinear media with non-centrosymmetric organization. This is due to the fact, that all even orders of nonlinear susceptibility χ disappear in the materials with inversion symmetry. On the other hand, third-order nonlinear processes like CARS can occur both in centro-symmetric and non-centrosymmetric media [11].

1.1.2 TPEF and SHG contrasts

SHG and two-photon absorption (TPA) are defined as a second and third-order nonlinear processes respectively. A simultaneous [1] interaction of two photons (with identical or different frequencies) with a molecule may lead to an absorption of both photons at the same time. SHG occurs in a parametric [2] process which requires a simultaneous absorption of two identical photons. The SHG emission is coherent and highly directional. Moreover, this process is instantaneous, mediated only by the virtual states of a molecule.

Contrary to SHG, TPEF radiation is incoherent and occurs between the ground and excited states [2]. A portion of the absorbed energy goes to non-radiative transitions between the molecule's virtual states. Thus, the TPEF emission is not equal to the frequency sum of the two absorbed photons.

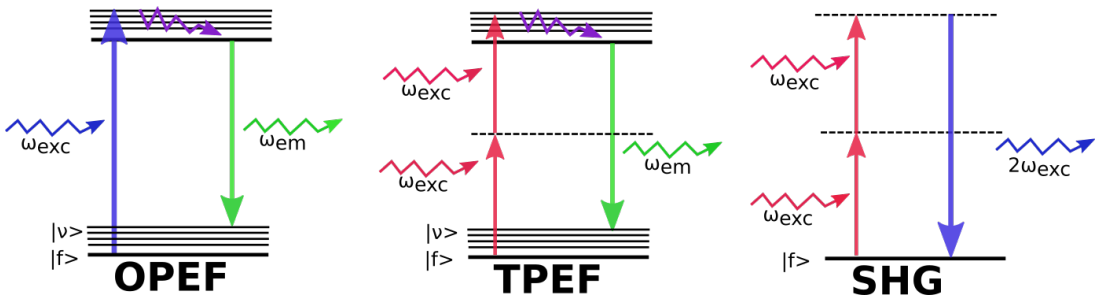

Figure 1.1 Perrin-Jablonski diagram of the energy transitions between electronic (and vibrational) states of a molecule. The depicted processes are: one and two-photon excited fluorescence and second harmonic generation.

Two-photon excitation fluorescence TPA can occur if two photons, with the energy sum matching the gap between the ground and excited states, interact *simultaneously* with a molecule or an atom. In this process, the molecule is excited from the ground state to an excited state (with many vibrational levels) from which it quickly relaxes to the lowest excited state defined

[1] A fraction of a femtosecond ($< 10^{-15}$ s) when a molecule resides in a virtual state

[2] The energy and angular momentum are preserved during the transition process, no energy is transferred to the medium

by a longer fluorescence lifetime of 10^{-9} s (Fig.1.1). A single photon is emitted by the molecule returning to the ground state. The quantum description of this process was done by Maria Göppert-Mayer in 1931 [12]. The probability of TPA is quantitatively defined by the two-photon cross-section σ_{2p}, measured in $\mathrm{cm}^4\mathrm{s}$ with $10^{-50}\ \mathrm{cm}^4\mathrm{s} = GM$ in honour of Göppert-Mayer. TPEF emission after an TPA event depends on the *quantum yield* ϕ_F. A product of the absolute two-photon cross-section (σ_{2p}) by ϕ_F is called the two-photon "action" cross-section [13].

TPE process requires a dense flux of photons incident on the sample. Pulsed lasers enhance the TPE process by a factor of $1/(\tau \mathrm{f_R})$ (τ and $\mathrm{f_R}$ are the pulse temporal width and repetition rate respectively) in comparison to continuous wave (CW) lasers with the same average power. The highest excitation efficiency is usually achieved using pulsed lasers with short temporal width (<100 fs), high peak power (500 kW) and repetition rate (80 MHz), tightly focused with high NA (>1.0) objectives [2]. The number of photons absorbed per pulse and per fluorophore is described as [14],

$$n_a \approx \frac{p_0^2 \delta}{\tau_p f_p^2} \left(\frac{(NA)^2}{2\hbar c \lambda} \right)^2 \tag{1.4}$$

where δ represents the TPA of the fluorophore at wavelength λ, p_0 is the average intensity, τ_p corresponds to the pulse duration, f_p is the laser's repetition rate, NA – focusing objective's numerical aperture, c and $\hbar$ stand for the speed of light and Planck's constant. From Eq.$(1.1.2)$ one can retrieve the dependence of the excitation probability (with constant average power and repetition rate) on the NA and the pulse duration τ_p. With increasing NA of the focusing objective, the focal spot becomes tighter and the excitation power is confined into a smaller focal volume. On the other hand, decreasing pulse duration allows for temporal concentration of photons distribution across an individual pulse, improving therefore the TPA probability. In TPEF the excitation probability and thus the fluorescence signal depend quadratically on the average intensity of the excitation light.

Second harmonic generation SHG is an example of a nonlinear optical interaction, which occurs in a second-order nonlinear media (Fig.1.1). This process is mediated by the second-order material susceptibility $\chi^{(2)}$ [11]. The electric field generated by a laser beam can be expressed as

$$\tilde{E}(t) = E \cdot e^{-i\omega t} + c.c. \tag{1.5}$$

If a material is characterised by $\chi^{(2)} \neq 0$, the incident electric field will generate a second order nonlinear polarization term (Eq.(1.3)):

$$\tilde{P}^{(2)}(t) = 2\epsilon_0 \chi^{(2)} E E^* + \left(\epsilon_0 \chi^{(2)} E^2 e^{-i2\omega t} + c.c. \right) \tag{1.6}$$

The first contribution in Eq.(1.6) with a frequency equals to zero creates a static electric field in the material (called optical rectification). The second term is responsible for SHG radiation and

contains an oscillation at frequency 2ω.

SHG emission can be generated in a process of annihilation of two photons with energy ω creating a new photon 2ω, as shown in Fig.1.1. The solid line corresponds to the molecular/atomic ground state, whereas the dashed lines represent virtual levels. The transition process mediated by virtual levels must obey to the law of energy and momentum conservation. Which implies two conditions: one for energy $\omega_{\mathrm{s}} = 2\omega_{\mathrm{i}}$ and the second one for momentum, which requires the *phase matching* condition:

$$\vec{k}_{\mathrm{s}} = 2\vec{k}_{\mathrm{i}} \tag{1.7}$$

where ω_{s} and ω_{i} correspond to the frequencies of the scattered and incident photons, respectively. The corresponding wavevectors are: $\vec{k}_{\mathrm{s}}$ and $\vec{k}_{\mathrm{i}}$. This condition can be relaxed when using high NA objectives which focus tightly the excitation beam and generate a wide distribution of $\vec{k}$ vectors. The SHG signal depends quadratically on the excitation power as follows from Eq. (1.6) :

$$I_{\mathrm{SHG}} \propto \left|\tilde{P}^{(2)}(2\omega)\right|^2 \propto I_{\mathrm{exc}}^2 \tag{1.8}$$

TPEF and SHG microscopy NLOM has become a powerful tool for biomedical imaging due to the unique features that it offers as compared to traditional wide field and confocal microscopy. More specifically, TPEF and SHG can be excited in the same imaging setup with a single pulsed laser [15]. TPEF microscopy using IR light is particularly valuable for live tissue imaging, since it provides an intrinsic z-sectioning and high penetration depth at low average powers. In comparison to one-photon excitation (OPE) process, when the fluorescence intensity decays with 1/z (z = distance from the focus) rate, TPEF signal intensity decreases much faster ($1/z^2$) as it depends quadratically on the excitation light intensity (Fig.1.2). The probability of nonlinear effects is the highest in the focal volume. Thus in TPEF, as well as in all other NLOM technique, the nonlinear signal comes only from the focal point. Besides, the excitation beam used for TPE operates at higher wavelengths as compared to OPE, which decreases tissue scattering and water absorption, leading to unprecedented penetration depths of the order of few hundred micrometers [2].

SHG provides a valuable information on tissues which do not possess inversion symmetry. Thus, only well-ordered protein assemblies like collagen, microtubules and muscle myosin can generate a strong SHG signal [15–19]. Moreover, forward generated SHG emission needs to be back-scattered to the collection objective from the excited tissue. Both transmission and reflection signal collection schemes, including numerous applications of SHG microscopy have been considered by Campagnola and colleagues [20].

Besides SHG, third harmonic generation (THG) features an additional microscopy tool for nonlinear imaging of unstained tissues. THG waves interfere destructively in homogeneous media; thus, a measurable THG signal can only be generated from the pulsed beam focused on the interface between two different media [11]. Starting from initial demonstration in 1997

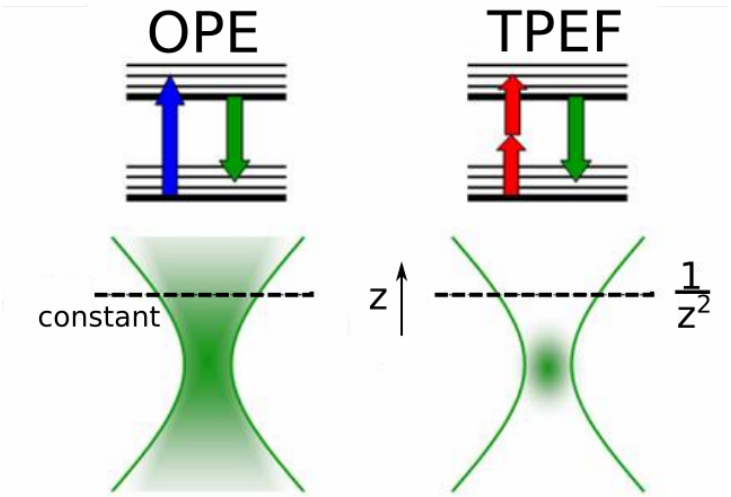

Figure 1.2 Intrinsic optical sectioning provided by TPEF contrast [http://biomicroscopy.bu.edu].

[21, 22], THG microscopes have been used for label-free, non-toxic, high resolution imaging of biological specimen [10, 23–25], intact and/or living tissues [26–28]. THG mediated inspection of live brain tissue has shown the potential to compete and possibly replace standard biopsy techniques [29,30]. With the use of optical fibers and micro-electro-mechanical system (MEMS) mirrors, a hand-held THG microscope was developed [31]. A miniaturized, portable, fiber-coupled probe will enable THG imaging in clinical applications.

TPEF, SHG and THG microscopy represent most of the developed NLOM, however another important contrast capable of chemical selectivity shall be introduced. The development of Coherent Raman microscopy techniques has enabled a fast, chemically specific, high resolution imaging with 3D sectioning capability. The first CARS microscope of this kind was demonstrated by A. Zumbusch and co-workers in 1999 [32] that implement a fs-CARS setup in a collinear geometry with the use of a high NA objective meant to relax the phase matching condition and to improve the axial resolution.

1.1.3 Coherent Raman scattering

Coherent Raman scattering (CRS) which consists of SRS and CARS, provides a means to inspect live tissues in label-free modality. CRS relies on a coherent excitation of chemical bonds with a frequency matching their mechanical vibration. Each individual chemical bond responds to the excitation field in a unique manner. In CRS process those molecular bonds can be probed individually, making this technique chemically selective.

Two pulsed-laser beams called a pump (ω_p) and Stokes (ω_S), with a frequency shift equal to the mechanical resonance frequency ($\Omega_R = \omega_p - \omega_S$) of the molecules of interest, are involved in CARS and SRS processes. The transition mechanism of SRS relies on a simultaneous excitation of a molecule or an atom by the two beams to a virtual state (Fig.1.3). An energy transfer occurs

between the pump and the Stokes pulses leading to an intensity loss for the pump beam and an intensity gain for the Stokes beam. Depending on the detected beam, a stimulated Raman loss (SRL) or stimulated Raman gain (SRG) can be observed using a lock-in detection.

CARS is a parametric nonlinear process which combines four waves interacting coherently. The first one called the pump (ω_{p}), brings the molecule from the ground state to a virtual level (Fig.1.3) from which it is de-excited by the Stokes beam to the vibrational state corresponding to a so-called beating or molecular vibration frequency (Ω_R). The combined action of the Stokes and pump beams brings the molecule into coherent superposition: the ground and the excited vibrational states become coupled. The third wave called probe (ω_{pr}) promotes the molecule to a virtual state, from which the molecule falls instantaneously to the ground state, emitting a photon which has the anti-Stokes frequency ($\omega_{AS} = 2\omega_p - \omega_S$).

The four waves interfering amongst them can also arrange in a process called four-wave mixing (FWM). This process is spectrally flat and limits the contrast in CARS imaging.

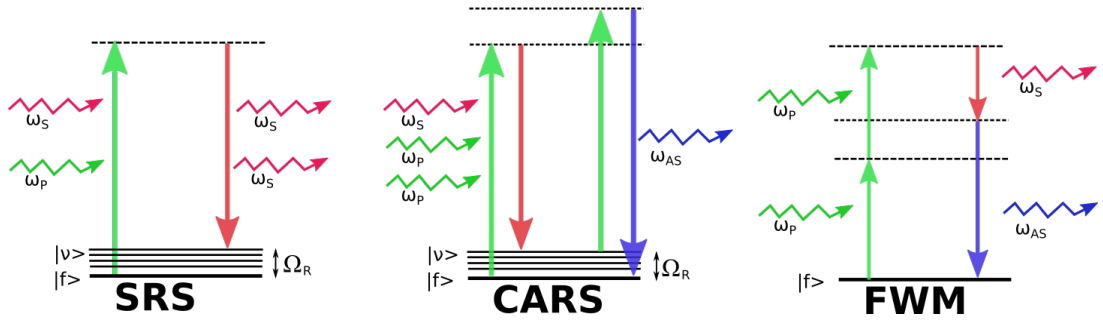

Figure 1.3 Perrin-Jablonski energy diagram describing the mechanisms of Stimulated Raman Scattering, Coherent anti-Stokes Raman scattering and Four Wave Mixing.

CARS microscopy The third-order susceptibility $\chi^{(3)}$ which causes the nonlinear response of a material is described as [33] :

$$\chi^{(3)} = \frac{A_R}{\Omega_R - (\omega_p - \omega_S) - ß\Gamma_R} + \chi^{(3)}_{NR} + \frac{A_t}{\omega_t - 2\omega_p - ß\Gamma_t} \tag{1.9}$$

where Ω_R is the molecular vibrational frequency. A_R and A_t denote the Raman scattering and the TPA cross-section constants. Γ_R with Γ_t represent the half-width at half-maximum of the Raman vibration line and of the electronic transition of the TPA [34]. The first term in Eq.(1.9) corresponds to the resonant contribution sensitive to molecular vibrations. The second term is a non-resonant spectrally flat CARS contribution responsible for the generation of FWM (Fig.1.3). The third term comes from another non-resonant contribution due to the two-photon electronic resonance. The two non-resonant contributions impair CARS microscopy; thus, different schemes for background elimination have been proposed: by modulating the frequency difference between the pump and the Stokes beam [35], using time-resolved and heterodyne [36]

detection schemes [37] or by performing polarization controlled CARS [38].

In CARS microscopy the condition of phase-matching has to be fulfilled:

$$\Delta\vec{k} = 2\vec{k}_p - \vec{k}_S - \vec{k}_{AS} \tag{1.10}$$

However, this condition is relaxed when a high NA objective is used to tightly focus the pump and Stokes beams on the sample [32].

CARS microscopy has flourished over the last decade and still has a potential to develop; however, its application in nonlinear endoscopy remains very challenging [39]. In Ch. 2, we will address this issue using several innovations developed in our group.

1.2 Ultrashort pulse delivery through optical fibers

The capability of NLOM has enabled a fast, high resolution imaging of unprocessed and/or specifically stained samples. The increased excitation wavelengths allowed deeper penetration due to the lower scattering and provided intrinsic sectioning inside different biological tissues. CRS has opened the door for chemically specific inspection of molecular vibration signatures. Although very powerful, NLOM remains complex for *in-vivo* applications due to the physical size of typical tabletop setups and/or necessary tissues extraction.

There has been a significant effort to miniaturize and simplify the complex, bulky NLOM schemes with the use of optical fibers. Despite important achievements, nonlinear imaging through miniaturized, fiber-coupled probes remains challenging. The reason for that lies in the behaviour of the ultrashort pulse in dispersive media such as solid core optical fibers. Some of these effects can be compensated or avoided, but the potential shown in NLOM has not been realized yet in fibered endoscopes.

In this section we will describe important optical phenomena responsible for the temporal and spectral broadening of the ultrashort pulse in solid core fibers.

Group velocity dispersion Light propagation in media or in a waveguide such as a fiber is described by the propagation constant. Often defined as γ, it determines the phase and amplitude variations along the propagation axis. In lossless media, γ is imaginary: $\gamma = \mathrm{i}\beta$ with the (real) phase constant β, which is the product of the effective refractive index and the vacuum wavenumber [40].

The normalized propagation constant β is wavelength dependent. Thus, different spectral components travel with a different speed. This dependency describes the phenomenon of group velocity dispersion (GVD). Femtosecond pulses have a large spectrum reaching up to tens of nanometer. When coupled into a silica fiber some parts of this spectrum propagate faster, some

- slower which results in the pulse temporal broadening. The GVD can be defined by:

$$\beta_2 = \frac{\partial \beta}{\partial \omega^2} = \frac{\partial}{\partial \omega}\frac{1}{\nu_g} = \frac{\partial \beta_1}{\partial \omega} \tag{1.11}$$

$\beta = \beta(\omega)$ stands for frequency dependent propagation constant of the fiber. $\nu_{\mathrm{g}} = \beta_1^{-1} = (\frac{\partial \beta}{\partial \omega})^{-1}$ represents the *group velocity*, which is the propagation speed of the wavepacket center. Generally, the GVD parameter β is given in $[\mathrm{s}^2/\mathrm{m}]$. Whereas in optical fibers this parameter is expressed as a derivative with respect to wavelength, with the dispersion parameter $\mathrm{D}_\lambda < 0$ in units of [ps/(nm km)]:

$$D_\lambda = -\frac{2\pi c}{\lambda^2} \cdot \beta_2 = -\frac{2\pi c}{\lambda^2} \cdot \frac{\partial^2 \beta}{\partial \omega^2} \tag{1.12}$$

Since a longer wavelength corresponds to a smaller frequency, β_2 and D_λ have opposite sign.

The GVD is generally classified as normal or anomalous depending the sign of β_2. When $\beta_2 > 0$ ($D_\lambda < 0$), longer wavelengths propagate faster than the shorter ones - this regime is called **normal dispersion**. In contrary, when $\beta_2 < 0$ ($D_\lambda > 0$) it is the **anomalous dispersion** regime.

Nonlinear spectral broadening Self-phase modulation (SPM) is a nonlinear optical effect which results in temporal and spectral broadening of the ultrashort pulse propagating through dispersive nonlinear media [11] such as an optical fiber. This nonlinear phenomenon becomes particularly important for pulses characterized by high peak intensity and very short pulse duration.

SPM occurs as a response of a nonlinear dispersive medium to high intensity fields which alter the properties of the medium through intensity dependent nonlinear contribution of the refractive index [41], given by the equation:

$$n(T) = n_0 + n_2 I(T) \tag{1.13}$$

In this equation, n_0 and n_2 are the linear and nonlinear refractive indices, and $I(T)$ stands for the field instantaneous intensity. As a result the propagating pulse experiences a nonlinear phase shift ϕ_{NL} because of the SPM:

$$\phi_{\mathrm{NL}}(T) = n_2 I(T) \omega_0 L/c \tag{1.14}$$

The strongest phase shift $\phi_{\max}$ depends on the peak power P_0 which can be calculated through average power P_{avg}, which can be expressed as:

$$P_0 = \frac{P_{\mathrm{avg}}}{f_{\mathrm{R}} \cdot \tau} \tag{1.15}$$

where τ is the pulse duration and f_R the repetition rate. Hence, the maximum phase shift

induced by the SPM after a propagation path z, is proportional to the propagation constant γ:

$$\phi_{\mathrm{NLmax}}(z) = \gamma P_0 z \tag{1.16}$$

It is possible to describe the nonlinear spectral broadening by representing the concept of the instantaneous frequency $\omega(\mathrm{t})$, described as

$$\omega(t) = \omega_0 + \delta\omega(t) \tag{1.17}$$

where $\delta\omega(t)$ corresponds to the variation of $\omega(\mathrm{t})$, represented as:

$$\delta\omega(t) = \frac{d}{dt}\phi_{\mathrm{NL}}(\mathrm{t}) \tag{1.18}$$

If we consider a $sech^2$ shape pulse with the intensity:

$$I(t) = I_0 \sec^2(t/\tau_0) \tag{1.19}$$

From Eq.(1.14) the nonlinear phase shift is:

$$\phi_{\mathrm{NL}}(t) = n_2 \frac{\omega_0}{c} L I_0 \sec^2(t/\tau_0) \tag{1.20}$$

If we introduce the instantaneous frequency change given in Eq.(1.18), then:

$$\delta\omega(t) = 2n_2 \frac{\omega_0}{c\tau_0} L I_0 \sec^2(t/\tau_0) \tanh(t/\tau_0) \tag{1.21}$$

An illustration given by Fig.1.4 shows the processes behind the described equations. Where the short pulse intensity (a) after propagation in a nonlinear medium along the z-axis ((b), n_2>0), the pulse experiences an instantaneous frequency shift (c) which results in a pulse spectral spread (d). The SPM becomes very strong when $\delta\omega_{\max} \geq \Delta\omega$, where $\Delta\omega$ is the spectral width of the incident pulse. Thus an important SPM is expected [11] whenever $\Delta\phi_{\mathrm{NL}}^{\max} \geq 2\pi$.

The situation of the pulse temporal (caused by GVD and SPM) and spectral (SPM only) spreading is true for transform-limited or positively chirped pulses propagating through media with normal dispersion regime ($\beta_2 > 0$). However, this condition does not hold for the case when a negative chirp is added to the pulse or if the propagation medium is characterized by the anomalous dispersion. The latter allows the GVD and SPM to cancel out each other, thus preserving the pulse transform-limited along propagation. This phenomenon called optical solitons has been studied in silica fibers [42, 43] and hollow-core fibers [44].

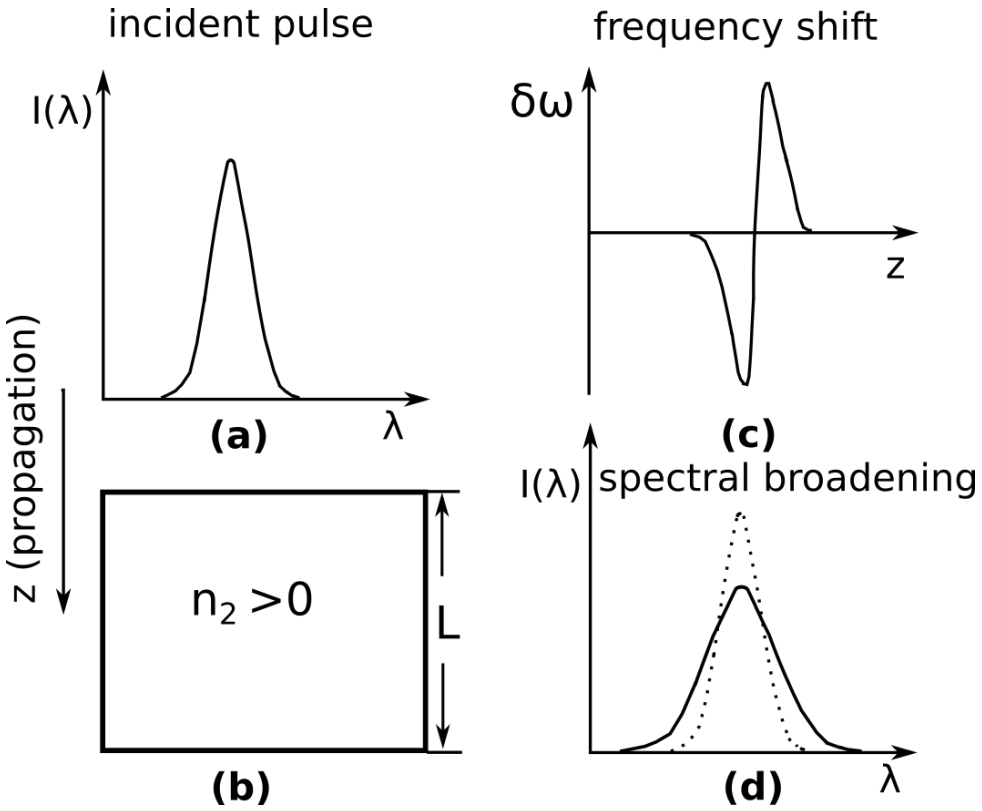

Figure 1.4 Self-phase modulation in nonlinear media. Spectral dependence of the incident pulse (a). Pulse propagation in a nonlinear medium with a length L (b) Frequency shift of the pulse after the propagation (c). Spectral broadening of the transmitted pulse (d).

1.3 Conclusions

The variety of NLOM contrasts have been developed to improve the conventional optical inspection methods used for the imaging of biological specimens. The problem of tissue bleaching, phototoxicity and low penetration depths has been addressed by the use of long excitation wavelengths. Intrinsic sectioning combined with label-free, chemically specific imaging have further strengthen the field of NLOM. However, there still remains the challenge to apply efficiently these fabulous achievements in miniaturized schemes mainly because of the short laser pulse delivery.

In the next chapter, we will show how CARS, SHG and TPEF can be implemented in a miniaturized, fiber-based, scanning endoscope.

Chapter 2

Multimodal endoscopy with Kagome fibers

This chapter deals with our high resolution multimodal (CARS and SHG) Kagomé fiber based scanning endoscope. This project was first developed in the framework of A. Lombardini's PhD thesis with my active participation in the endoscope development and applications. I have built an optical setup for CARS with a mechanical delay-line, into which the endoscope developed by A. Lombardini was integrated. I was also responsible for the exploration of the endoscope applicability for CARS imaging of CH (human colon and skin; mouse brain, spinal cord and liver) and CD bonds (skin samples with deuterated glycerol, not presented in this work).

An introduction to the field of nonlinear CARS endoscopy will be given in Sec.2.1. We will briefly discuss the scanning piezotube mechanism and consider the optical setup in Sec.2.2 and Sec.2.3, respectively. Herein we address the challenge of FWM background-free short pulse delivery by means of Kagomé fibers Sec.2.4. The working principle of the endoscope will be described in detailed in Ch.4. In Sec.2.5, we demonstrate CARS *ex-vivo* human colon high contrast images with sub-cellular resolution. Besides, we show SHG images of collagen fibers from human colon and rat tail tendons. The results that will be presented in Sec.2.5 manifest the possibility to perform CARS imaging in a simple and robust setup over large FOVs.

2.1 Nonlinear endoscopy for medical diagnostics

Histological inspection of biopsy tissues has been the gold standard in cancer diagnostics. The removed tissue must be firstly sectioned in some dozens of microns thick slices and then stained with HE (hematoxylin and eosin) markers. This inspection method is time-consuming and requires significant labour. The development of CARS and SRS, gives new insights on the early stage cancer diagnosis. These nonlinear imaging techniques are label-free, chemically specific and very fast [45,46], providing new solutions for intra-operative histopathology [47–49]. How-

ever, this highly advanced technology so far have been efficiently employed only in microscopy, limiting therefore the imaging depth to several hundred micrometers due to tissue absorption and scattering [50].

Despite all the efforts, CARS imaging through a fiber endoscope remains challenging [51–57]. The main technical difficulties arise at the stage of short pulse laser delivery and signal collection. Excitation beams delivery for CARS/SRS endoscopy is more complicated than in case of SHG and TPEF [58–60], since two beams must be temporally and spatially overlapped. In solid-core fibers, these two co-propagating pulses generate a strong spurious signal in the fiber core in a nonlinear FWM (valid only for CARS) [51]. As an attempt to suppress the CARS background, two fibers were employed: one for the excitation and the second one for signal collection [51, 55, 57]. At the same time, polarization control and large mode area fibers were exploited to reduce the parasitic FWM [52, 53]. However, this leads to an unavoidable increase of the endoscope size and/or a loss in optical contrast and resolution.

Furthermore, in solid-core fibers, the GVD and SPM can broaden the pulse temporal width and reduce the pulse peak intensity [41]. For CARS imaging therefore, all these propagation issues should be solved for two different frequencies, further complicating the design of fiber based endoscope.

Another interesting approach of a combined laser scanning microscope (LSM) and GRIN lens rigid endoscope for CARS imaging, has been demonstrated very recently by the group of Prof. Zumbusch [61]. Importantly, this rigid endoscope makes use of pico-second pulses which increases spectral resolution, but at the same time the excited vibrational signal is lower than in fs-second regime. The reduced FWM background coming from the GRIN lens is achieved by the combination of a low NA (<0.1) scanning lens and a distal lens assembly. The first one decreases the FWM generation in the GRIN lens due to phase-matching condition and the second one introduces a small shift between the pump and the Stokes beams, thus lowering the FWM from the optical system.

In this work, we present a high resolution, fully integrated and compact endoscope based on a hollow-core double-clad Kagomé lattice fiber. The excitation beams are delivered through the hollow core, while the signal (CARS and SHG) is collected by the double cladding of the same fiber.

2.2 Fiber resonant scanning

Piezo-electric tube based fiber resonant scanning has been widely used in optical microendoscopy. Starting from the pioneering work of Eric Seibel [62], resonant scanners have become an inexpensive and robust solution for scanning on the sample compared, for instance to MEMS. Many research groups have worked with the technique of fiber resonant scanning [63–66], including the recent work on TPEF and SHG combined scanning endoscope [60]. A classical setup

for nonlinear endoscopy is shown in Fig.2.1. In this example, the fiber end is fixed in a voltage driven piezo-electric tube. In order to obtain high fiber deflection the applied voltage drives the piezo with the mechanical resonance frequency of the free-standing fiber tip. The commonly used raster (with a slow and fast axes) scanning cannot be adopted for these scanners, since both axes (x and y) must be driven at resonance. However, using a sinusoidal shape driving waveform with a $\pi/2$ phase shift between the x-y axes, a circular scan pattern can be produced. A GRIN lens is used for the excitation light delivery and excited signals detection. All these components are integrated in a metal tube.

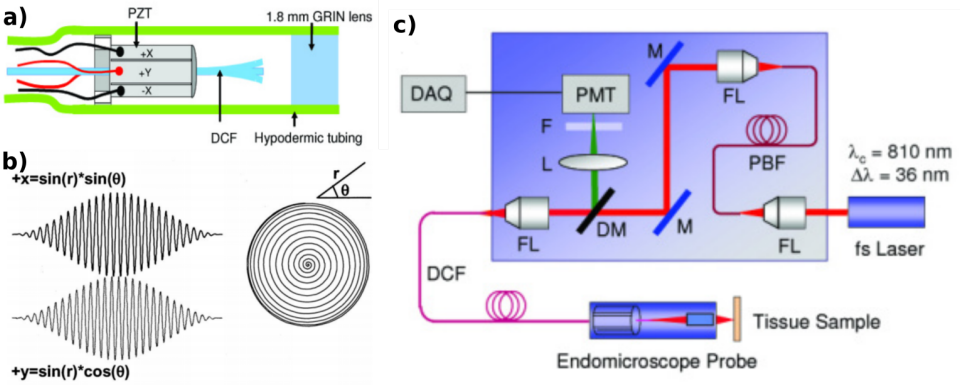

Figure 2.1 An example of fiber resonant scanning endoscopes [67, 68].

In Ch.4 I will present in detail the aspects and principles of fiber resonant scanning, as simultaneous driving of y and x axes, quality factor definition of a scanner and scan corrections. These processes and parameters were very well described in Alberto Lombardini's manuscript [69]. In this work, I will introduce a different, much smaller piezotube (1.5 mm outer diameter and 10 mm length), which has replaced the one used in Alberto Lombardini's thesis. Further, I developed the fiber resonant braking for fast endoscope scanning.

2.3 CARS imaging setup

The two trains of laser pulses required for CARS imaging are provided by a Discovery (Coherent, USA) laser system. It combines a fixed wavelength (1040 nm, $\tau = 140$ fs) Ytterbium fiber laser feeding a tunable optical parametric oscillator (OPO: 680-1300 nm, $\tau = 100$ fs). The repetition rate is 80 MHz. The fixed 1040 nm beam serves as $\lambda_{\mathrm{Stokes}}$, whereas λ_{Pump} will be tunable depending on the targeted vibrational levels wavenumber Λ. The Stokes beam is send through a delay line (computer controlled) in order to change the temporal delay between the pump and Stokes beams. The two beams are spatially overlapped on a Notch filter which reflects a very narrow band (10 nm) with $\lambda_{\mathrm{central}} = 1040$ nm, while passing the Pump. The two beams are then coupled into the Kagomé hollow fiber core (0.02 NA) with help of a microscope objective

(40x, 0.6 NA). We have embedded two telescopes – one for each beam – to efficiently control the beams' divergence and size. The focal spot is then relayed by an assembly of minilenses (Edmund Optics) onto the sample plane. Sample generated signal can be either epi-collected by the double-clad of the fiber and reflected by a long pass filter (Semrock, $\lambda_{\text{cutoff}} = 720$ nm), or forward-collected by another microscope objective and detected by a photomultiplier tube (H7421-40, Hammamatsu). A custom-written Labview software (National Instruments) performs synchronized fiber scanning and image acquisition. Our flexible endoscope probe due to a very simple configuration with only one fiber for excitation and collection becomes much smaller (4.2 mm — outer diameter, 40 mm — rigid length) compared to reported CARS endoscopes [55, 70].

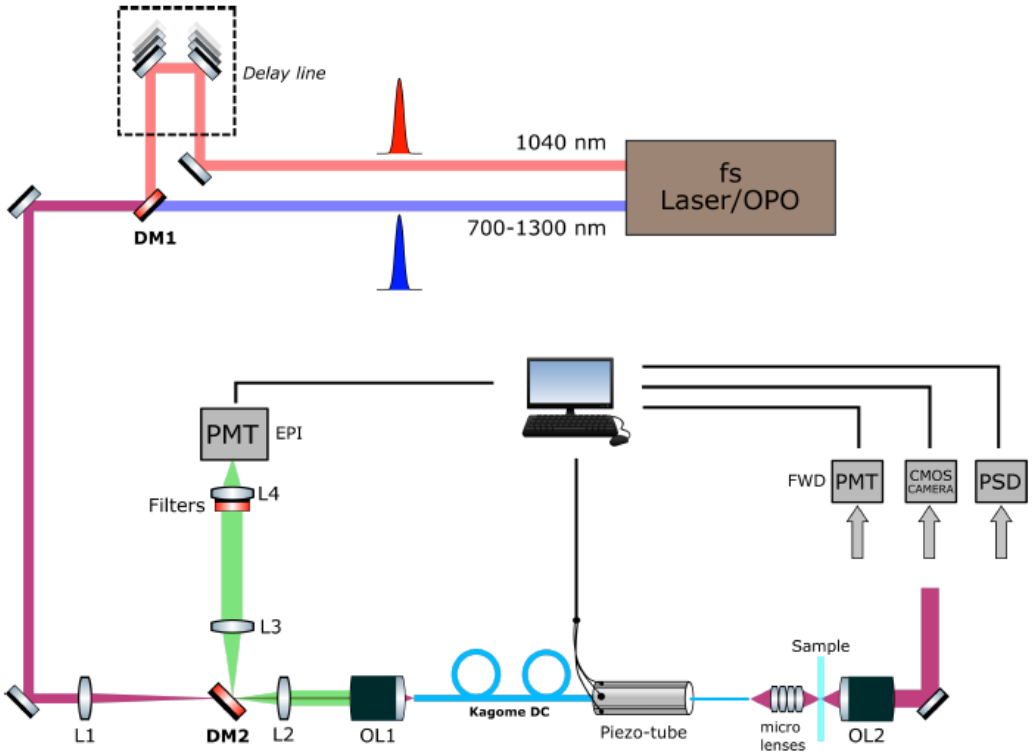

Figure 2.2 The setup for nonlinear endoscopic imaging. The optical elements: L1: f=400 mm; L2: f=40 mm; L3: f=100 mm; L4: f=50 mm; OL1 and OL2: 60x Olympus, NA=0.6. Dichroic mirror (DM), longpass (LP) 650 nm. Filters: shortpass 690 nm. Photomultiplier tube (PMT). Position sensitive detector (PSD).

Mini-objective for the multimodal endoscope In fiber scanning endoscopy, the focusing optics plays a vital role. Beside, the signal collection efficiency depends on the sample side NA of the focusing optics. Generally, in scanning endoscopes the beam is focused on the sample either by a GRIN lens or by an assembly of mini-lenses. Despite the advantageous miniature size, GRIN lenses are known to suffer from strong chromatic aberration, which shifts longitudinally

the focal spot up to 1 mm at (λ ~750-900 nm) [68].

A modern strategy for GRIN lens chromaticity compensation has been proposed [60]. Liang *et al.* developed a TPEF/SHG endoscope probe with a custom-made achromatic miniature objective combined with 2 commercial GRIN lenses (GRINTECH GmbH, Germany). This miniature objective consists of a plano-convex lens and a phase diffraction grating [71]. The diffractive grating introduces a negative chirp which compensates the positive dispersion induced by the GRIN lenses. The researchers reported 10 μm sample-side and <230 μm fiber-side longitudinal shift of the focal spot with a 0.8 collection NA. Although the development of such GRIN-miniature objective coupled units is improved compared to standard GRIN lenses, their complicated design and limited working distance (<300 μm) may require an alternative solution.

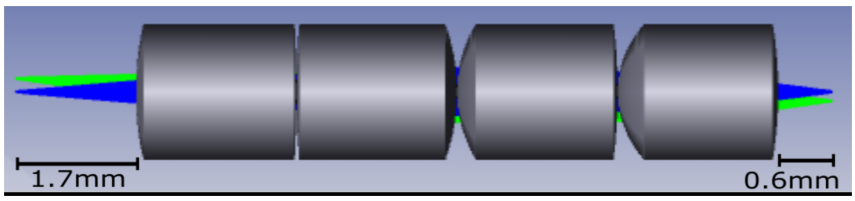

Figure 2.3 Lens assembly for the endoscope probe. Image taken from [69].

In this work, we stick to a custom-designed mini-objective (Fig.2.3). It has been shown that such assemblies are optimal for CARS probes [57, 72, 73]. Our focusing mini-objective (Fig.2.3) consisting of 4 achromatic doublets was designed in Zemax by Alberto Lombardini during the course of his PhD thesis. The mini-objective lenses have different focal lengths: 9 mm (EO #83-338), 6 mm (EO #65-569), 4 mm (EO #65-568) and 3 mm (EO #65-567) (Edmund Optics). A MgF_2 coating on the lenses minimizes the reflection in the visible range. The main characteristics of the mini-objective are the following:

- Working distance in air: WD=600 μm
- Sample-side magnification: M=0.63
- Sample-side numerical aperture: NA=0.45
- Fiber-side numerical aperture: NA=0.3

2.4 Kagomé fibers

Hollow core fibers (HCF) draw attention for several reasons. Firstly, light guidance in such fibers is altered as compared to conventional total internal reflection (TIR) based waveguides. HCF's central capillary is filled with air and surrounded by a silica photonic structure clad. HCF can be divided in two main groups depending on the way they guide light. The first group relies on photonic bandgap guidance, hence called photonic bandgap fibers (HC-PBGFs, see

Fig.2.4 a) [74, 75]. HC-PBGFs exhibit the lowest loss amongst hollow core fibers at around 1-2 dB/km [76], but the price to pay is its narrow transmission window (less than 100 nm) and strong GVD as the wavelength moves away from the center of the transmission band ($\Rightarrow$ they can be efficiently used with femtosecond pulses with spectral bandwidth of <10 nm). Kagomé lattice hollow core fiber (Fig. 2.4 b) characterized by a so called David Star pattern guides light due to its weak coupling between the core mode and cladding modes. This fiber is lossier (< 5 dB/m) as compared to PBGFs, however it provides a much broader transmission window (400-500 nm). Importantly, the GVD in the Kagomé is low over the whole transmission window (few ps/nm/km).

New HCFs designs have been proposed that reduce transmission losses: antiresonant simplified photonic structure fiber (Fig. 2.4 c), and a new Kagomé fiber design (Fig. 2.4 d), with reduced transmission losses. There exists another type of HCFs, called negative curvature (NC) or inhibited coupling (IC) fibers, which will be discussed in detail in the Chapter 3.

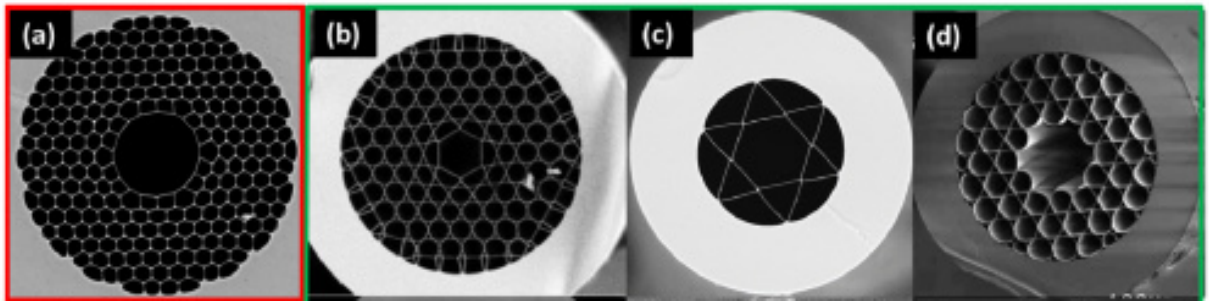

Figure 2.4 Scanning Electron Micrographs of different hollow core fibers: PBGF (a) [77]; Kagomé cladding with a straight hollow core (b), antiresonant fiber (c) [78] represented with a hexagram [79], and Kagomé hypocycloid core (d) [80]. Rearranged from [81].

2.4.1 A new double-clad Kagomé fiber

Pulse temporal width, as we have already discussed in Ch. 1, defines how efficiently we can excite non-linear signals from the sample. Hollow-core fibers represent a pertinent solution for dispersion-less short laser pulse delivery. Furthermore, the non-linear refractive index in the hollow core of such a fiber scales down by three orders of magnitude as compared to solid core fibers. Hence these fibers are interesting for CARS beams delivery without the generation of spurious FWM non-resonant background inside the fiber core. Remains the problem of the CARS signal back collection efficiency.

Our collaborators at Institut de Recherche sur les Composants logiciels et matériels pour l'Information et la Communication Avancée (IRCICA, Lille, France) have designed and fabricated a Kagomé hollow core fiber (Fig.2.5) having a 0.02 NA. They have also made a silica double-cladding around the photonic crystal structure. The double-clad has an NA of 0.5 and is intended

to collect the generated CARS signal which gets scattered and reflected by the sample. The second ring with air holes confines the epi-scattered signal in the collection clad.

The sophisticated design of the Kagomé fiber renders its optical properties to be uniquely beneficial for the ultrashort pulse delivery. The dispersive and spectral effects seen in solid-core fibers are expected to be negligible even for femtosecond pulses with high peak power, propagated over a piece of 2-3 meters long Kagomé fiber. The fiber core can transmit excitation wavelengths range of 680-1100 nm with lower than 5 $\mathrm{dB} \cdot \mathrm{m}^{-1}$ attenuation (Fig.2.5 c). Such transmission characteristics allow to deliver pump and Stokes beams that can cover a large range of vibrational wavenumbers, until 4000 cm^{-1}. At the same time, ultrashort laser pulses keep their narrow temporal width due to a very low GVD in this spectral range (5 $\mathrm{fs} \cdot \mathrm{nm}^{-1} \cdot \mathrm{m}^{-1}$, see Fig.2.5d).

We have measured the pulse duration (setup presented in Fig.2.2) after propagation in the Kagomé fiber core to remain nearly unchanged even at 50 mW output power (see Fig.2.6a). Moreover, due to the anomalous dispersion of the Kagomé fiber, ultrashort pulses can even be slightly compressed (because it compensates the positive dispersion acquired by the pulses in the optical elements before the fiber). The ultrashort pulse despite the high peak power does not generate new spectral components, when delivered through the Kagomé fiber core (Fig.2.6b).

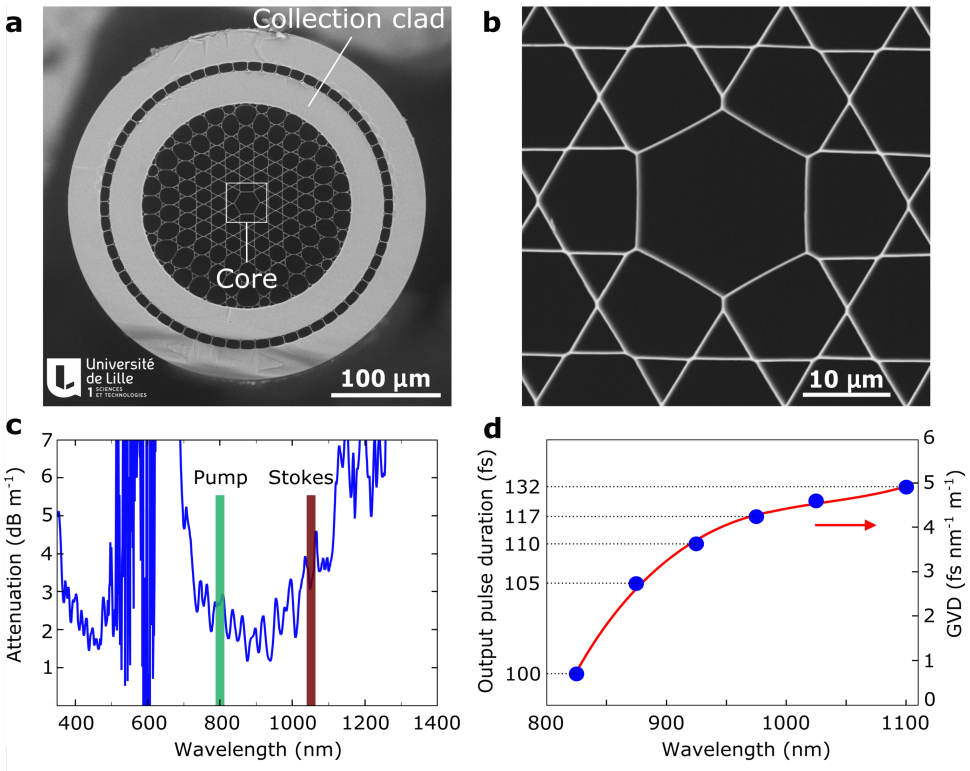

Figure 2.5 Kagomé fiber SEM image (a), zoom on the fiber core (b), fiber core attenuation curve and output pulse temporal width with the fiber imposed GVD (c) and (d).

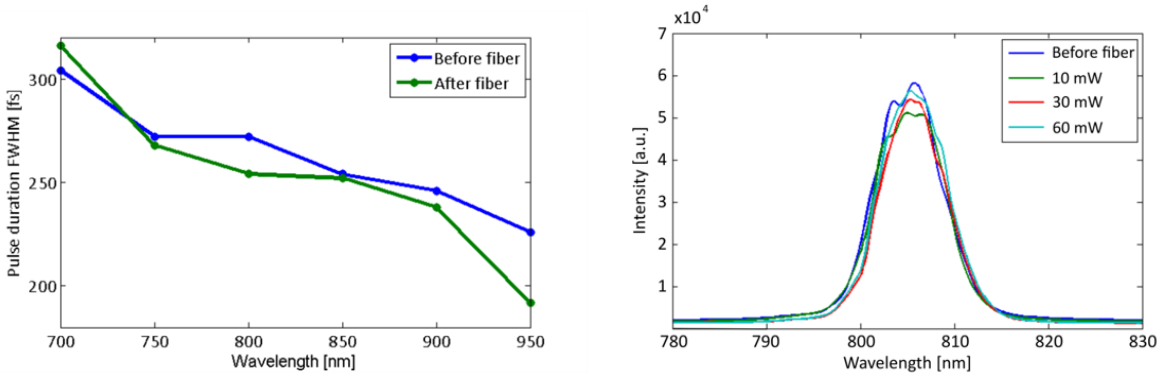

(a) (b)

Figure 2.6 Pulse duration measured (autocorrelator) for different wavelengths (Ti : Sa laser) (a). The pulse temporal width measured before (blue curve) and after (green curve) the Kagomé fiber (1 meter). Pulse spectral measurement (805 nm center) for different power levels, before and after the pulse propagation in 1 m of Kagomé fiber (b). Image taken from [69].

2.4.2 Focusing microsphere

The Kagomé fiber's modal area is around 18 μm, that corresponds to a 0.02 NA. This NA had to be increased, before integrating the Kagomé fiber into a scanning endoscope. The miniature objective (described in Sec.2.3) was used to relay the beam exiting the fiber core onto the sample plane. However, the mini-objectives demagnification was only 0.63, which could have led to $\sim$11 microns spot on the sample. If further demagnified, the scan amplitude would have been reduced proportionally. We addressed this challenge by introducing a focusing microsphere on the Kagomé fiber core output facet (Fig.2.7). A silica microsphere sealed in the fiber core renders the 18 μm modal area into $\approx$1.2 μm focal spot on the sample. The silica microsphere placement and sealing will be described in Ch.3, when talking about a new hollow-core fiber, and in Ch.5, dealing with the integration procedure of a portable endoscope probe.

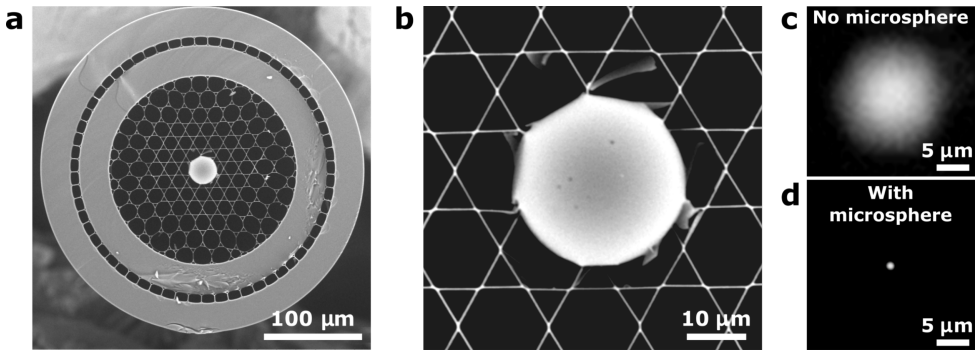

Figure 2.7 Kagomé fiber and the silica microsphere on the fiber core. SEM image of the fiber with the attached microsphere (a), zoom on the fiber core (b), field modal area through the core (c), focal spot made by the microsphere (d).

2.4.3 CARS beams delivery by Kagomé fiber

FWM as a parametric process generates a non-resonant signal at the CARS wavelength:

$$\lambda_{\mathrm{CARS}} = (\frac{2}{\lambda_{\mathrm{pump}}} - \frac{1}{\lambda_{\mathrm{Stokes}}})^{-1} \tag{2.1}$$

where λ_{pump} and $\lambda_{\mathrm{Stokes}}$ correspond to the pump and Stokes wavelengths. The non-resonant part of the third-order nonlinear susceptibility coefficient χ^3_{NR} causes this FWM background in CARS.

In order to study the non-resonant FWM generation in the Kagomé fiber, we have implemented the setup shown in Fig.2.8. We scan the delay between the pump and Stokes beams and compare the olive oil CARS signal with the FWM background. The Coherent Discovery generated pump (800 nm) and Stokes (1040 nm) beams were superposed spatially and temporally. The forward generated CARS signal was back-reflected from the sample glass cover slip and collected by the fiber. Olive oil contains an abundance of carbon hydrogen (C-H) vibration bonds generating a very strong CARS signal at $\Omega_{\mathrm{R}} = 2885\ \mathrm{cm}^{-1}$. In this study, we want to assure that the CARS signal generated from the olive oil is much stronger (with SNR>10) than the background FWM generated in the focusing microsphere or elsewhere in the fiber. By changing the temporal delay between the beams, the position where they are temporally overlapped changes, and the generated CARS and FWM are detected by the PMT.

We scan the Stokes beam with respect to the pump beam with help of a mechanical delay line over 2 picoseconds. The sample is placed in the focal plane of the mini-objective lens and the generated CARS signal is collected by the Kagomé fiber double-clad (red curve in Fig. 2.9). The high peak from the red curve indicates the CARS signal from the olive oil sample. The smaller intensity peak corresponds to the FWM originating from the glass microsphere, but it is shifted by a temporal delay of more than 400 fs from the sample temporal overlap. Thus, if the pump and Stokes beams are temporally superposed on the sample, there is no more overlap on the focusing microsphere. Next, to check if there is no FWM background generated from the fiber itself, the olive oil sample is removed and the experiment with the delay is repeated. In Fig.2.9, the blue curve denotes the FWM generated from the Kagomé fiber, while sweeping the delay between the two beams (2 ps). Only a marginal FWM contribution due to the focusing microsphere can be seen from the blue curve, but even this spurious FWM is successively separated by the temporal delay.

We can conclude that only a negligible FWM background is created when the pump and Stokes overlap temporally on the sample. The explanation of this difference in temporal delay lies in the fact that the GVD of the mini-objective induces an additional delay between the excitation beams, thus separating the temporal overlap for the sample and the microsphere. This method works perfectly for femtosecond CARS endoscopic imaging, contrary to all fiber-delivered CARS probes developed for the moment. The femtosecond CARS enables for high

speed, strong signal, very low background and low average powers contrast imaging. However, if high spectral resolution is desired, pico-second sources have to be used and this method might need to be improved.

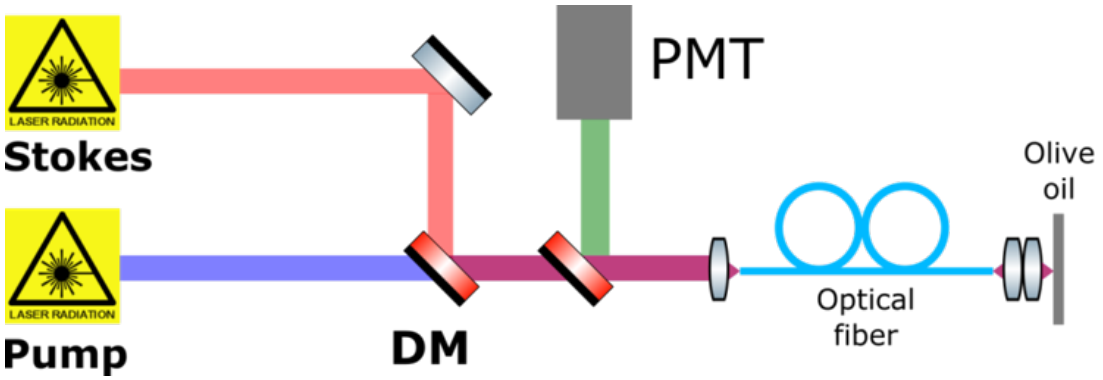

Figure 2.8 FWM measurements setup. λ_{Stokes} and λ_{Pump} overlap on a dichroic mirror (DM) and are coupled into 1-m long Kagomé fiber. The CARS signal generated by olive oil is then collected by the double-clad and redirected by a short-pass filter to a PMT.

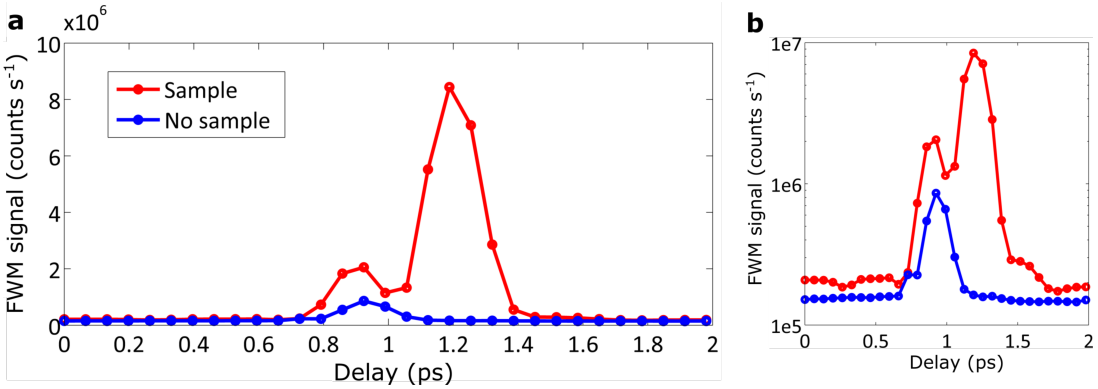

Figure 2.9 Kagomé fiber generated FWM and olive oil CARS signal versus the delay between the pump and Stokes beams (a). Logarithmic scale of the two curves (b).

2.5 CARS and SHG imaging *ex-vivo*

The portable endoscope probe consists of the hollow core DC-Kagomé fiber threaded in a piezoelectric tube (Physik Instrumente, OD=3.2 mm), integrated together with a custom-made mini-objective into a stainless metal tube (Fig.2.10). The excitation beams (Coherent Discovery) are coupled into the fiber core with a microscope objective. A circular pattern (∼320 μm) is produced on the sample. The back-scattered signal is collected by the Kagomé fiber double-clad and sent to the detector (PMT).

We demonstrate the imaging capabilities of the Kagomé fiber endoscope using 5 μm polystyrene

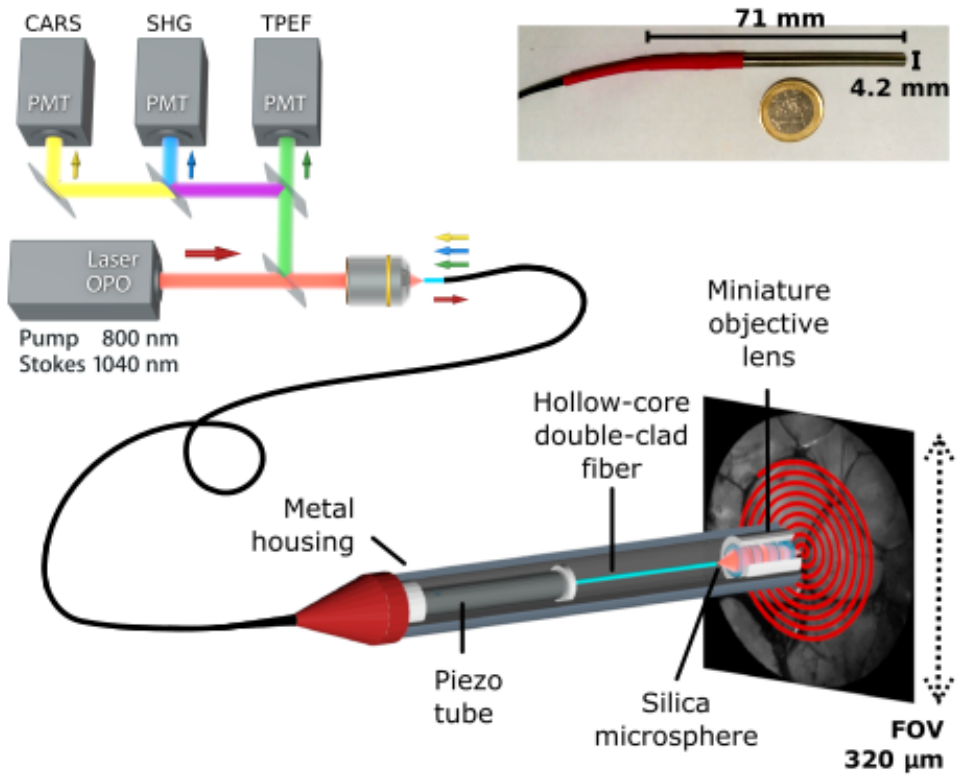

Figure 2.10 A schematic, simplified illustration of the Kagomé endoscope. A photograph of the portable probe is shown in the inset.

beads deposited on a glass coverslip. CARS image of the beads looks uniform with a very low FWM background (Fig.2.11 a). The driving voltage applied to the piezotube was decreased by 50 %, resulting in a twice smaller FOV=155 μm. This allowed to zoom on the polystyrene beads (Fig.2.11 b).

The lateral resolution of the imaging system was measured using 200 nm fluorescent beads. The excited TPEF signal ($\lambda_{\text{exc}} = 800$ nm) from the beads was forward detected. We retrieved the size of the point spread function (PSF), its full width at half-maximum (FWHM) from TPEF images of the fluorescent beads. The achieved TPEF lateral resolution was around 0.83 μm. The axial resolution of 5.9 μm was measured.

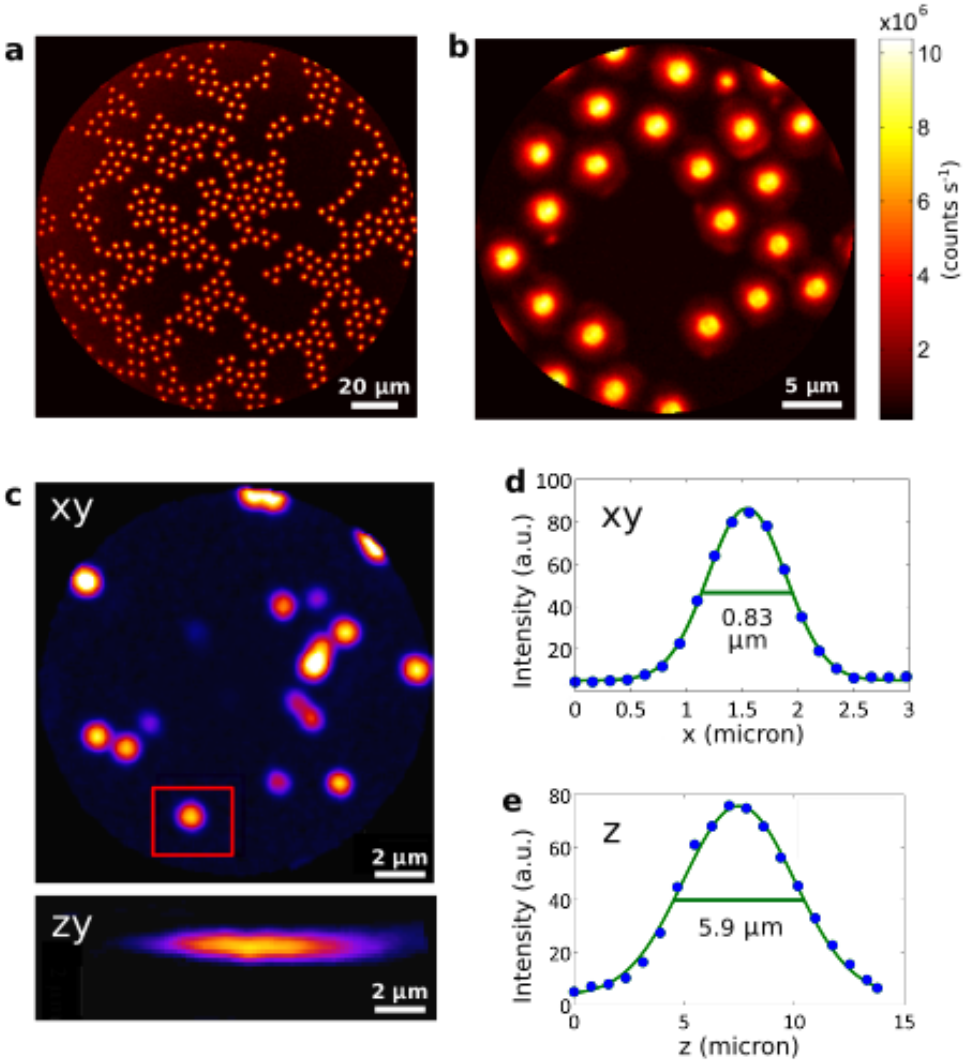

Figure 2.11 CARS images of 5 μm polystyrene beads deposited on a coverslip: 320 μm FOV (a) and 155 μm (b), respectively. Powers: 10 mW (λ_{pump}=800 nm) and 5 mW (λ_{Stokes}=1040 nm). TPEF image of 200 nm fluorescent beads (c). The estimated lateral and axial resolution (d) and (e), respectively.

Next we performed CARS and SHG endoscopy imaging of fresh human colon fatty tissues providing a strong CARS signal from C-H bonds (2850 cm^{-1}), and rat tail tendon (SHG from collagen fibers). The tissues were sandwiched in water between two coverslips (100 μm thick) with a 1-mm adherent spacer and placed vertically in front of the endoscope. A high contrast CARS signal was generated by the human colon sample with only 30 mW average power (Fig.2.12 a). SHG signal generated by collagen fibers from the rat tail tendon demonstrated the high performance of the flexible endoscope (Fig.2.12 b). The 0.8 μm lateral resolution is confirmed with a close-look on collagen fibrils (Fig.2.12 c). The superposed CARS (lipids) and SHG (collagen) images demonstrate the capability of the Kagomé fiber based endoscope to perform nonlinear, multimodal imaging of fresh, unstained tissues. All images (Fig.2.12) were acquired at 0.8 frame/sec, 5 times averaged, along with 350 μm field-of-view (FOV).

Such endoscopic performance renders intraoperational label-free imaging and diagnostics one step closer to reality. Proteins and lipids proliferation rate can be a remarkable sign of malignant or early-stage cancerous tissues [82–84]. Thus bringing the developed flexible probe to the hospital would help practitioners to identify cancerous tissues and assist him/her to take intra-operative decisions.

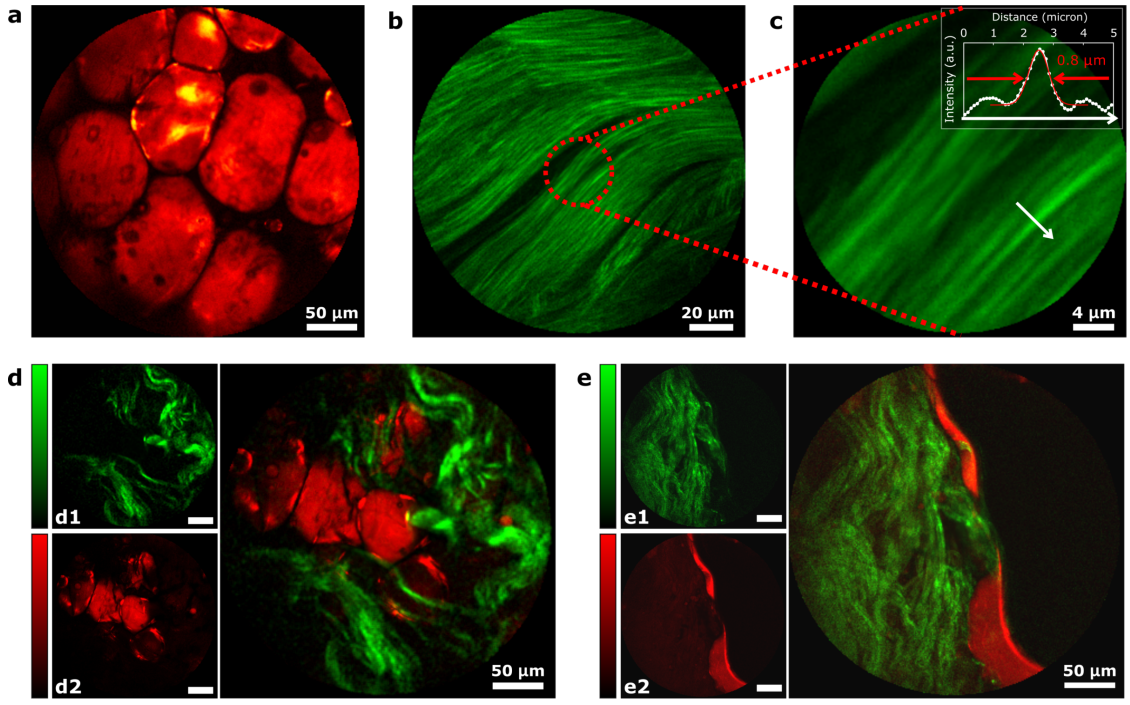

Figure 2.12 CARS (CH_2) bonds at 2850 cm^{-1} human colon (a), SHG rat tail tendon collagen fibers (b), SHG rat tail tendon magnified (c). Human colon (d) superposed CARS (2850 cm^{-1}) and collagen SHG (e) images. Powers on sample: P_{Stokes} =10 mW, P_{Pump} =20 mW and P_{SHG} =60 mW.

2.6 Conclusions

In this chapter, we reported on the development of a high resolution, flexible, compact endoscope for CARS and SHG imaging. We have addressed the challenge of the two temporally and spatially overlapped beams delivery through optical fibers by means of a Kagomé hollow core, double-clad fiber. The Kagomé fiber enables background-free, dispersion-less femtosecond pulse delivery over a broad spectral range. The innovation represented by the silica focusing microsphere allowed for sub-micron resolution imaging with FOVs over 350 μm. The obtained CARS and SHG high-contrast images confirm the potential of the developed endoscope for label-free, low excitation power optical imaging and diagnostics.

2.7 Kagomé fiber limitations

Despite all the advantages of the Kagomé fiber, such as its broad transmission window, very low dispersion and negligible FWM, it still has some limitations. We will see in the following chapter (Ch.3), that it is possible to overcome these limitations using a novel negative curvature fiber (NCF).

Signal collection through the Kagomé fiber To study the collection efficiency of the Kagomé fiber, we conducted a simple experiment. A homogeneous fluorescein (FITC) solution was excited at 800 nm, and the generated TPEF signal was epi-collected by the fiber distal end (detection band 500 to 600 nm). A small area avalanche photodiode (APD, 160×180 μm) was conjugated with the fiber proximal end (Fig.2.13 a). The image of the 250 μm double clad was magnified on the APD's plane by a factor of 4.5. This magnification resulted in a 1.1 mm collection clad's image, which was sufficient to spatially resolve the collection clad, the photonic structure and the core (Fig.2.13 b).

In this experiment, we wanted to mimic the situation when the sample is weakly or strongly scattering. The TPEF signal was collected by the fiber in two modalities: with a scattering layer behind the sample and without. A thin layer of Titanium dioxide (TiO_2) was placed behind the FITC solution. TiO_2 is known as a strong scatterer which does not absorb in the visible range. We scanned a small sensor area APD along the x-axis with and without a scattering medium behind the sample. In absence of the scattering medium, the TPEF signal from fluorescein was mostly collected by the hollow core of the fiber (blue curve in Fig.2.13 c), since the TPEF signal without being scattered is usually back-collected by the fiber core in the same geometrical scheme as it was excited. However, in presence of the scattering layer, the fluorescence photons scatter strongly; thus as a result, the silica double-clad started to collect the scattered photons (red curve).

We conclude, that the double clad collects most of the back-scattered photons from strongly

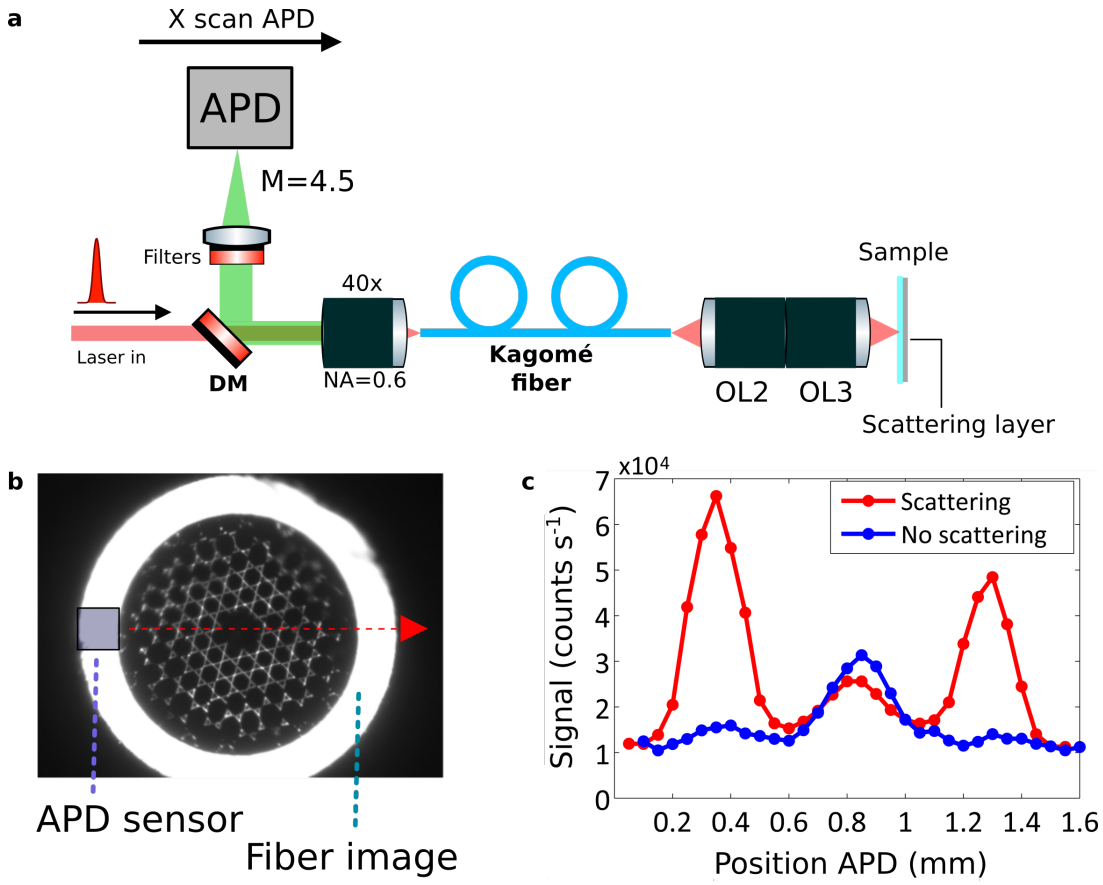

Figure 2.13 An experimental setup used for the signal collection study (a). Kagomé fiber profile laterally scanned by a small area APD detector (b). TPEF signal from a fluorescein solution collected by the Kagomé fiber core (centre) and the double-clad (edges), in presence of a scattering layer (red curve) and without the scatterer (blue curve) (c).

scattering samples. *Therefore, the size of the double-clad's collection surface area plays a very important role*. Given the inner and outer diameters of the collection ring (180 and 250 μm respectively), we calculated the collection area to be 24000 $\mu\mathrm{m}^2$. Thus, one could think of decreasing the Kagomé structure size to increase the fiber collection surface. Beside, as shown in Figure2.13 c), poor transmission of the Kagomé core in 450-650 nm spectral range causes high losses of the signal collected by the fiber core.

To summarize, the two main hurdles of the Kagomé fiber: poor transmission of the fiber core in the typical emission spectral range of TPEF and CARS (450-650 nm) and a limited collection surface of the silica double-clad (DC). We want to address these limitations in the next chapter with the design of a new fiber whose guiding mechanism is based on antiresonant coupling, also known as negative curvature fiber.

Chapter 3

Negative curvature fiber improved signal collection

This chapter introduces a new type of hollow core fibers named Negative Curvature fiber (NCF). We will measure the signal collection through the NCF double-clad and investigate whether the properties of this fiber can meet the requirement of an increased sensitivity. Furthermore, the fabricated fiber presents a lowloss core transmission band around 500-600 nm suitable for green fluorescent protein (GFP) TPEF fluorescence collection. The fiber was fabricated at IRCICA in Lille by Prof. Kudlinski and other collaborators. A general overview on anti-resonant NCFs will be given in Sec.3.1. Where we will firstly discuss the principles of antiresonant inhibited coupling light guiding in the NCF, and discover its applications in imaging. We will also report on ultrashort pulse broadening and nonlinear interaction in the NCF in Sec.3.2. Finally, we will summarize the NCF's novelty and improvements compared to our previously used Kagomé double clad fiber (Sec.3.3).

3.1 HC-NCFs overview

In the previous chapter (sec.2.4), we have introduced the concept of hollow core fibers. So far, we have only considered Kagomé fibers. However, another class of inhibited coupling (IC) antiresonant (AR) fibers known as negative curvature fiber (NCF) has recently attracted considerable attention [85].

Research on AR reflection waveguides has yielded a new category of HCFs called NCF [78, 86–89]. The name roots from the fact that NCF consists of a hollow core and of one ring of tubes around it (Fig.3.1a). Hence, having the core wall curvature pointing inward, which is by convention the negative axis (Fig.3.1b).

The first AR optical waveguide was fabricated in 1986 [90, 91]. In this work the authors report on a new waveguiding technique with a loss of 0.4 dB/cm for the TE mode. Many other

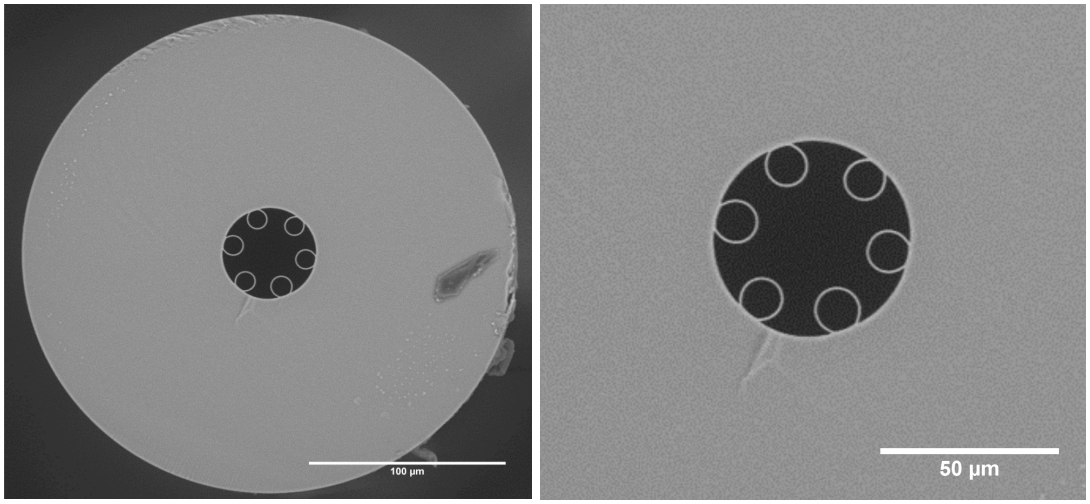

(a) **(b)**

Figure 3.1 SEM photograph of a 6-tube double-clad NCF (a). Zoom on the 30 μm hollow core, surrounded by silica tubes for inhibited mode coupling between the core and the clad (b).

different AR designs have been proposed, including Kagomé fibers [92, 93]. Light guiding in NCFs is based on two optical effects: antiresonant reflection and inhibited coupling. The effect of antiresonance can be explained by the light destructive interference between the fiber core mode and cladding modes (described in detail in subsec.3.1.3)

However, antiresonance at the core boundary is not the only condition for an efficient low-loss guidance. A wavenumber mismatch between the clad and core modes is needed to inhibit the coupling between the two. The clad modes may exist inside the silica tubes, in the gaps between the tubes and in the outer silica clad-ring. The combined effects of AR and IC have led to transmission losses of the order of < 10 dB/km [85, 94].

Fabrication ease of NCFs has allowed developments of interesting fibers. Such as non-silica glass fibers for mid-infra-red (IR) [95, 96], where chalcogenide glasses replace silica [97, 98]. This opens up the possibility to create fiber lasers operating in mid-IR regime and other tools for very precise, minimally invasive micro-surgeries.

3.1.1 NCF nonlinear imaging and spectroscopy tools

Whilst this is the first report of endoscopic imaging with an NCF, this fiber has already found applications due to its capability of delivering high-power, ultrashort pulses with minimal distortion. An NCF has been exploited for TPEF fibre-coupled microscopy imaging by Sherlock *et al.* [99]. When propagating 200 fs laser pulses through 1.5 m custom-fabricated NCF, the authors show that the pulses remain quasi-unchanged with the fiber GVD calculated to be around -175 fs^2/m. The authors perform TPEF excitation through the NCF in a scanning microscope setup, and demonstrate the collection of the excited signal from ex-vivo mouse skin sample by

a multimode fiber bundle.

Another application of the NCF has been reported by Popenda et al [100]. In this work, the NCF fiber is proved to have a very low GVD (5 $\mathrm{ps} \cdot \mathrm{nm}^{-1} \cdot \mathrm{km}^{-1}$) across 680-750 nm, resulting in only 0.5-0.9 fs pulse broadening in 1.5 m NCF at 80 mW output power (pulse width before the fiber: τ_{input}=161 fs). The authors present a sensor for multiphoton spectroscopy, where an NCF is used only for light delivery. It can record emission spectra from endogenous flurophores as NADH (nicotinamide adenine dinucleotide) and FAD (flavin adenine dinucleotide). However, the collected autofluorescence signals is coming from very concentrated solutions of NADH and FAD (that are not representative of biological samples) by means of conventional solid core step-index fibers.

3.1.2 NCF based microsurgery

Lasers can be applied for material removal with a very high precision in a process called laser ablation. At low incident powers, the irradiated part of a material is evaporated or sublimated. However, laser ablation is commonly performed with high intensity lasers, which generate plasma from the ablated zone. In medicine, for laser surgery ultrashort pulses with high peak power are used. Hollow core photonic crystal structure (PCS) fibers can efficiently deliver those pulses without temporal broadening and spectral profile alteration. Optical surgeries are mostly performed in aqueous environment which absorb well in IR, such that a portion of heat generated by a laser pulse can remove a desirable piece of tissue. A significant challenge remains to deliver optical pulses in this spectral range as they are also well absorbed by silica - the main constituent of conventional fibers.

Urich *et al.* [101] proposed the application of NCFs for a flexible, small size tool for soft and hard tissues ablation. The tool operates at 3 μm wavelength (225 μs pulse width), around which biological tissues in aqueous solution absorb extensively. An NCF fiber transmitted these pulses at 3.05 μm with 34 dB/km losses. The fiber distal end was protected from contamination with a sapphire cover window mounted with help of a heat shrinking tube (see Fig.3.2). This optical surgery tool could generate 30 mJ at 2.94 μm at the surface of the distal tip with an energy density exceeding 500 J/cm^2 at the contact point. Such level of energy density surpasses the energy required for biological tissues ablation. In spite of this, the tool withstands well these energies, because of high damage threshold of the NCF. In Fig.3.2 b), the ablation of bovine bone in air is shown. The cut depth reaches 220 μm along with the width of 300 μm.

3.1.3 Guidance mechanism

AR and IC phenomena decribed above are both involved in the low-loss guidance mechanism in NCF. We will analyse both of them, starting from the simple model of a slab waveguide.

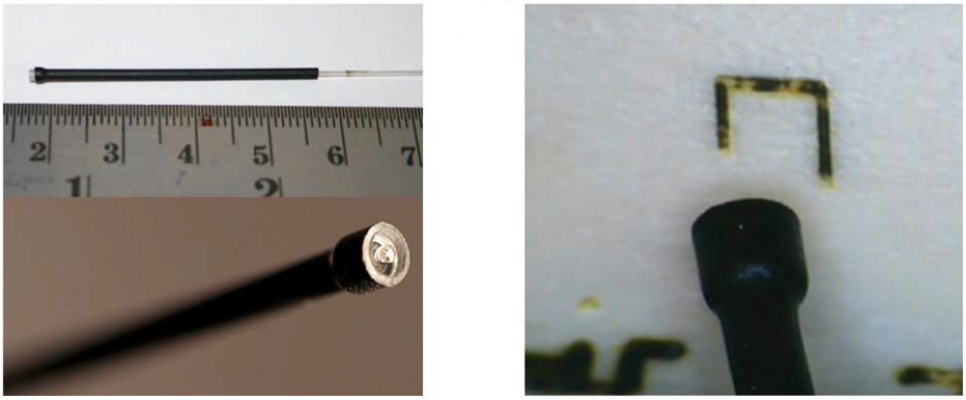

Figure 3.2 NCF mounted operating tool with a heat sink (a). Laser ablation of ovine bone in air (b). Adapted from [101].

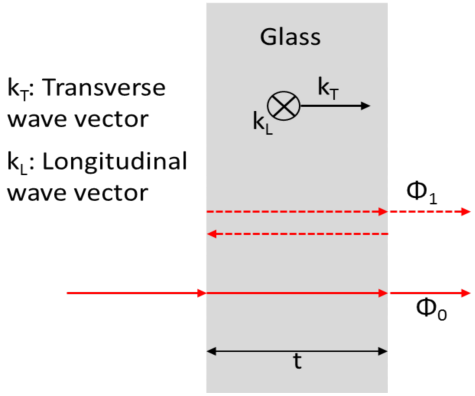

Figure 3.3 Schematic presentation of the resonance and antiresonance conditions in a slab waveguide. The resonance condition applies when the phase difference is a multiple of 2π, with m being any positive integer [90]. For certain values of t the condition of antiresonance ($\Delta\phi = \pi$) will apply. Redrawn from [102].

Antiresonant (AR) reflection In a slab waveguide (thickness, t) with core width W $>> \lambda_0$, the longitudinal ($\tilde{\mathrm{k}}_\mathrm{L}$) and transverse ($\tilde{\mathrm{k}}_\mathrm{T}$) vectors can be approximated to $n_0 k_0$ and $k_0(n_1^2 - n_0^2)^{1/2}$ in the glass region, where $k_0 = 2\pi/\lambda$ defines the wave vector in the air and n_0, n_1 - refractive indices of air and glass.

$$\Delta\phi = 2\mathrm{tk}_0(\mathrm{n}_1^2 - \mathrm{n}_0^2)^{1/2} \tag{3.1}$$

Where $\Delta\phi$ is a phase shift between two waves: one which has directly passed the glass slab and the second one, which has been reflected from the slab surface (Fig.3.3). Resonant and AR regimes can be described by the following equations:

- **Resonance condition**:

$$\Delta\Phi = \Phi_1 - \Phi_0 = 2m\pi \tag{3.2}$$

$\Delta\Phi$ represents the phase difference between the reflected and transmitted waves (m=0,1,2..n). This phase shift will eventually establish the conditions of resonance and antiresonance. From 3.2 and 3.1 we can find the thickness t of the material to be:

$$t = m\lambda/[2(n_{glass}^2 - n_{air}^2)^{1/2}] \tag{3.3}$$

- **Antiresonance condition**:

$$\Delta\Phi = \Phi_1 - \Phi_0 = (2m-1)\pi \tag{3.4}$$

where t is now given as

$$t = (m-0.5)\lambda/[2(n_{glass}^2 - n_{air}^2)^{1/2}] \tag{3.5}$$

To conclude, the reflected and transmitted waves can be put in resonance or in antiresonance by carefully selecting the waveguide thickness t. Depending on t, the two waves can interfere constructively (resonance) or destructively (antiresonance).

In hollow core waveguides with a silica layer (cladding) around the core, a strong coupling occurs between the core and the clad modes when the resonance condition established. However, when these modes interfere destructively, a very good core mode confinement is achieved. The silica layer can be considered as a Fabry-Perot (FP) resonator [103]. The wavelengths corresponding to high transmission parts of the spectrum interfere destructively in the FP resonator, reducing dramatically the core mode leakage. NCF has a more complicated architecture of the AR surfaces. Generally, it is one ring of silica hollow tubes with or without spacing between them.

Let's discuss the principles of the NCF core fundamental mode behaviour. We consider a simple model of an NCF with 8 cladding tubes without gaps between the tubes (Fig.3.4a) [102]. Glass is depicted in gray, and the white zones represent air. The main NCF parameters are

related by the equation [104, 105]:

$$\mathrm{D_{core}} = (\mathrm{d_{tube}} + 2\mathrm{t})/\sin(\pi/\mathrm{p}) - (\mathrm{d_{tube}} + 2\mathrm{t}) \tag{3.6}$$

where t is the thickness of the tube wall, d_{tube} stands for the inner tube diameter, p gives the number of tubes, and D_{core} represents the core diameter. The fundamental core mode's normalized electric field intensity is shown in Fig.3.4b.

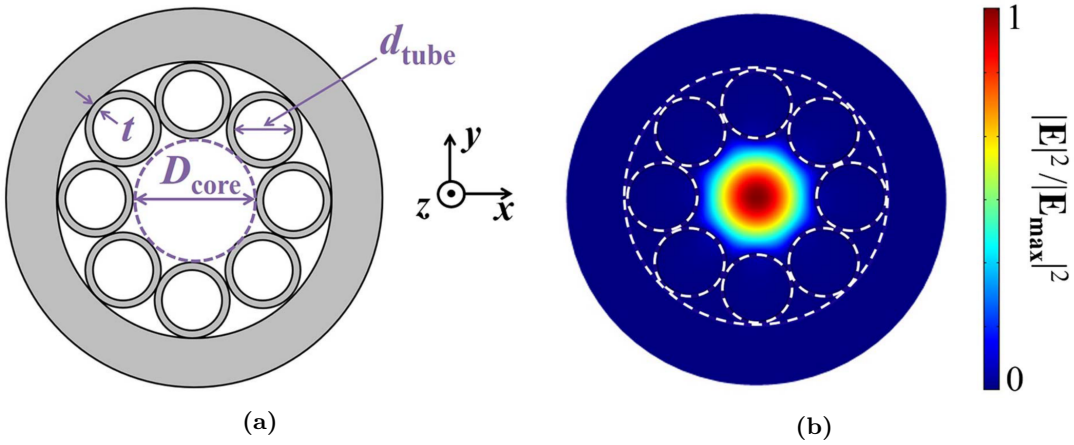

Figure 3.4 AR reflection principle in NCFs. Fiber geometry is given in (a). This is a general model without gaps between the tubes [102]. Normalized electric field distribution of the fundamental mode of the NCF core (b). The glass/air boundaries are depicted in white dashed curves. Adapted from [102].

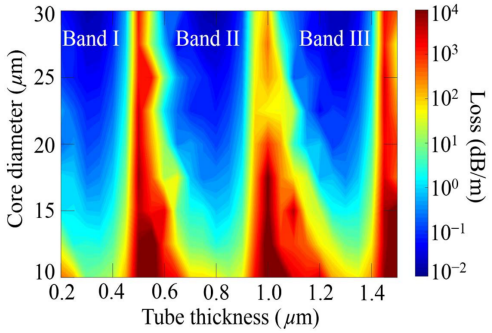

Figure 3.5 NCF fundamental core mode losses. As the air core diameter increases, the leakage loss decreases. However, the resonance condition does not change with different D_{core}. The tube thickness defines the resonant or AR regions. Leakage loss is very high at the resonance and low in AR regions. Taken from [102].

All these parameters define the losses of the core fundamental mode. It is possible to design a desirable effective index[1] of the fundamental core mode by changing the cladding tubes wall thickness d_{tube} or the fiber core diameter D_{core}. A specific d_{tube} thickness can lead to the AR

[1] Effective index is the ratio of the propagation constant in the waveguide to the free space propagation constant

condition. In this regime, the fundamental core mode's loss is very low (Fig.3.5). In contrary, these parameters can also be tuned to be in resonance, which will result in the highest leakage loss of the core fundamental mode.

Inhibited Coupling (IC) AR reflection suppresses the losses of the fundamental core mode. So, light can only weakly penetrate the silica structure which surrounds the core. Nevertheless, it is important to inhibit the coupling of the core and clad modes. The coupling reduction can be achieved by introducing the conditions for a small spatial mode overlap and a mismatch of the effective core and clad indices [85, 94].

As a model to describe IC between the core and the clad in NCF, a 6-tube fiber with 30 μm air core is taken (Fig.3.6).

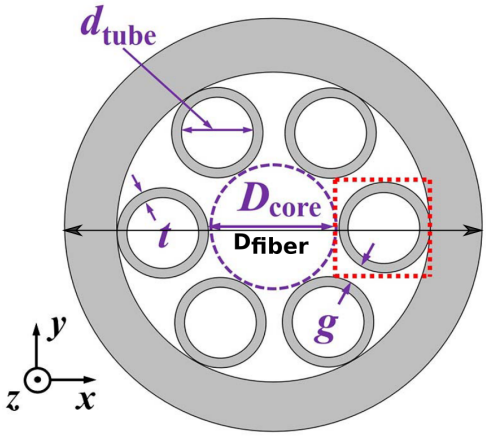

Figure 3.6 NCF with 6 cladding tubes. With a core diameter D_{core}, tube diameter and thickness: d_{tube} and t, and distance between two adjacent tubes g. Redrawn from [102].

A new parameter g stands for the distance between two adjacent clad tubes. The cladding modes will be considered in the red-dotted clad tube [102]. At certain thickness t of the glass tube, the core fundamental mode and the clad mode coupling will be strongly inhibited. Fig.3.7a) shows the dependence of the effective index (n_{eff}) of the true modes [2] on the tube diameter d_{tube} or on the gap distance g, when the diameter of the fiber core is 30 microns. The red and blue solid lines represent effective indices of the true cladding tube mode and the true fundamental core mode. We notice that those effective indices approach when the gap g is reduced or the cladding tube diameter d_{tube} is increased [102]. The true fundamental core mode in the NCF experiences higher losses when there is no gap between the cladding tubes, because of coupling to cladding modes (see Fig.3.7b). We can see that the minimum loss is located at $g = 5$ μm (distance between two adjacent cladding tubes). The losses become high when the

[2] True modes are the modes which solve Maxwell's equations in the whole waveguide. These modes are neither core modes, nor clad modes.

gap g is changed from 5 μm to 10 μm, because the core mode leaks through the increased air gap. Energy losses also increase for larger d_{tube} due to the induced mode coupling between the cladding and the core.

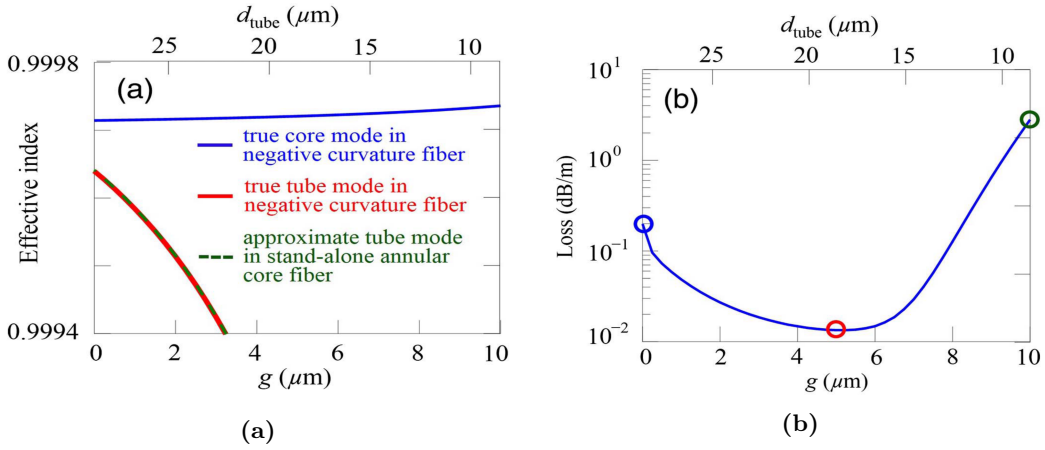

Figure 3.7 NCF geometry dependent modes coupling and effective indices mismatch. In the true core fundamental mode is given by the blue solid line (a). The red solid line depicts the effective index as a function of the true mode of the selected cladding tube. The approximate tube mode in stand-alone annular core fiber appears in green. Core fundamental mode losses as a function of the tube thickness and diameter is shown in (b). Adapted from [102]

3.2 Ultrashort laser pulses delivery via NCF

Non-linear mechanisms like CARS, SHG or TPEF excitation fluorescence require ultrashort pulses for efficient excitations. Ultrashort pulses broaden when propagating through conventional silica fibers. The positive dispersion generated in silica can be compensated by inducing a negative chirp (see Ch.1. However, in endoscopy this pre-compensation complicates significantly the setup and can work only in a very narrow spectral range [63]. Moreover, while trying to do CARS employing solid core fibers, things get even more complex. The strong FWM background generated in the silica core overwhelms the weak resonant CARS signal from the sample. In this section, we study ultrashort pulse propagation through NCF fibers. We consider here a DC-NCF optimized for the CARS beams delivery (800 and 1040 nm) designed and fabricated by Alexandre Kudlinski at IRCICA Lille. We show the autocorrelation measurement of the pulse duration before and after propagation in the NCF (Fig.3.10). Importantly, we show a 10-fold smaller fiber generated FWM as compared to the resonant CARS signal coming from an olive oil sample (Fig.3.12b).

3.2.1 Transmission

We show the attenuation curve of the NCF core presented in Fig.3.1a). This fiber has a broad transmission window: ∼750-1050 nm. It is suitable to perform CARS using IR pump and Stokes beams but also for the the delivery of TPEF (GFP at 920 nm) and SHG (rat tail 800 nm) excitation beams (Fig.3.9a). While in this fiber the core does not transmit well at the emission wavelengths of TPEF (usually in the green), CARS and SHG, the pure silica double-clad (0.5 NA) is made to collect most of the back-scattered photons.

The simple design of NCF fibers facilitates their fabrication and permits to tailor the NCF core transmission spectrum. An improved NCF with an additional transmission band at 500-550 nm (Fig.3.9b) of the fiber core will be exploited for in-vivo TPEF imaging of GFP-labeled neurons in mouse brain (Ch.6).

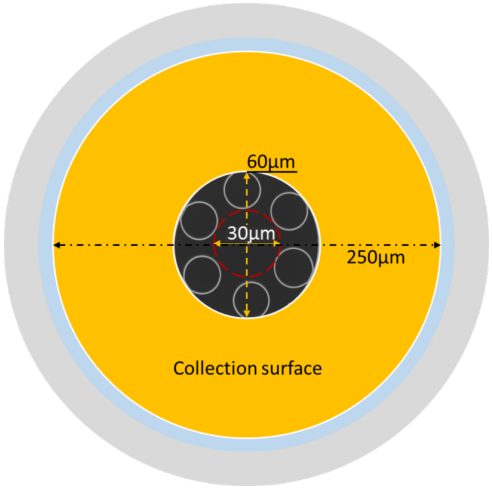

Figure 3.8 NCF used in this PhD thesis work. A 30 μm hollow core encircled by 6 glass tubes constitutes the inner part of the fiber. The pure silica double-clad of 250 μm diameter ensures an enhanced signal collection. Two additional polymer layers with low refractive (blue) and high refractive (gray) indices prevent light leaking from the silica double-clad and provide the fiber mechanical protection.

In optical fibers, as stated before, the GVD is usually normal for 800 nm-1100 nm wavelengths. However, in NCFs the GVD is anomalous [99, 100]. So, for positively chirped beam entering the fiber we expect a little compression of the short pulses after propagation through the NCF. We have measured the pulse duration before and after 1.5-meter long NCF with an auto-correlator (pulseCheck, APE). The Coherent Discovery laser generates 140 fs pulses at 1040 nm and 100-120 fs pulses for the tunable OPO (680-1300 nm). This laser contains an internal prisms-based system for group delay dispersion (GDD) compensation on the OPO output (up to GDD=-25000 fs^2 for certain λ).

Bulky optical elements like microscope objectives induce a positive dispersion chirp on ultrashort pulses. With the laser GDD compensation the pulse minimal duration can be restored. In Figure 3.10, we show the pulse duration measured before the NCF fiber (red curve) and after

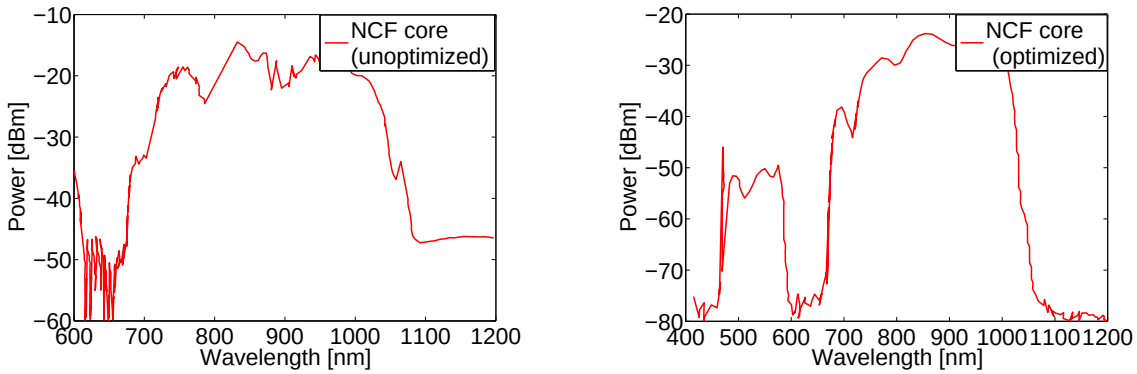

(a) (b)

Figure 3.9 The attenuation curve of the NCF core, unoptimized for the collection of typical CARS, TPEF, SHG emission wavelengths (a). The attenuation of the optimized NCF core with an additional transmission band (b).

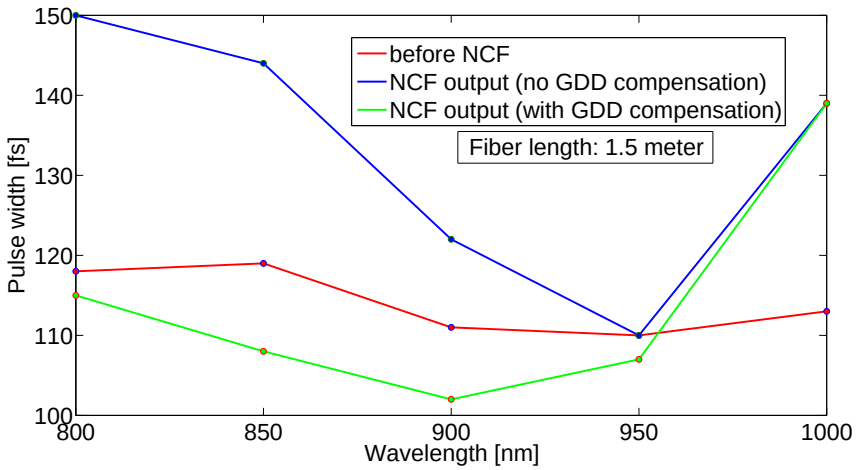

Figure 3.10 Pulse width as a function of wavelength. Initial pulse duration before the NCF (red curve); at the fiber output but without dispersion (induced by the coupling objective) compensation (blue curve) and at the NCF output with the GDD compensation (green curve).

propagating in the NCF (blue curve, green curve). The first set of pulse width measurements was done before a microscope objective used to couple into the NCF core (red curve). It is the microscope objective which broadens the ultrashort pulses measured after the NCF (blue curve). The objective's positive GVD could be successfully compensated by the Discovery system induced negative GDD (from -5000 to -500 fs^2 for 800-900 nm, green curve). The GDD at higher wavelengths (> 900 nm) could not be compensated, since no negative dispersion pre-chirp can be induced by this system in the given spectral range.

As a conclusion, we have shown that the NCF can deliver ultrashort pulses without temporal spreading in a broad spectral range (800-1000 nm). Next, we will discuss the nonlinear interaction of spatially and temporally overlapped the Stokes and pump beams propagated in the hollow core of the NCF.

3.2.2 Silica microsphere focusing

In fiber-scanning endoscopes the optical system's resolution and the FOV are related. A beam exiting the optical fiber has a certain diameter. This beam is relayed by a focusing unit on the sample plane. Thus, conjugating the fiber plane and the sample plane, a demagnification is commonly needed to provide a good optical resolution. However, the adjusted demagnification reduces the FOV. A scanning endoscope based on a lensed fiber was developed for high resolution big FOV microendoscopy [59].

We measured the field modal diameter around 25 μm (0.02 NA) of the NCF core output beam (Fig.3.11 a). For at least 2.5 μm lateral resolution on the sample plane, we would have to demagnify the hollow core output beam by 10 times. This would decrease the FOV on the sample by a factor of 10.

We address this issue by placing a transparent silica microsphere on the fiber core [69]. The microsphere increases the core NA from 0.02 to almost 0.4, focusing the beam into a tight spot ($\approx$1.2 μm) a few microns away from the fiber (Fig.3.11 b). This eliminates the need of a strong demagnification, preserving high FOVs. Silica beads (30 μm) from Thermo Scientific (9000 Series Glass Particle Standards) are used, since they can sustain very well beam powers higher than several hundreds of mW.

In this PhD thesis, the same approach has been successfully applied. The procedure of a microsphere placement remains the same as described by A. Lombardini [69] and presented in Ch.2. One needs a micro-metric precision translator, for example, the Nanomax stage (Thorlabs). A solution of silica microspheres is deposited on a glass coverslip (Fig.3.11c). After the coverslip dried up, we bring it in contact with the NCF fixed on the Nanomax. The frontal NCF structure surrounding the core gets slightly deformed by the microsphere. Electrostatic forces keep the bead in the fiber core. A silica microsphere of 30 μm diameter inserted on the DC-NCF core of the same diameter (30 μm), never falls down even at high deflection amplitudes of the resonantly driven fiber tip. However, to assure its proper fixation for the integration in a

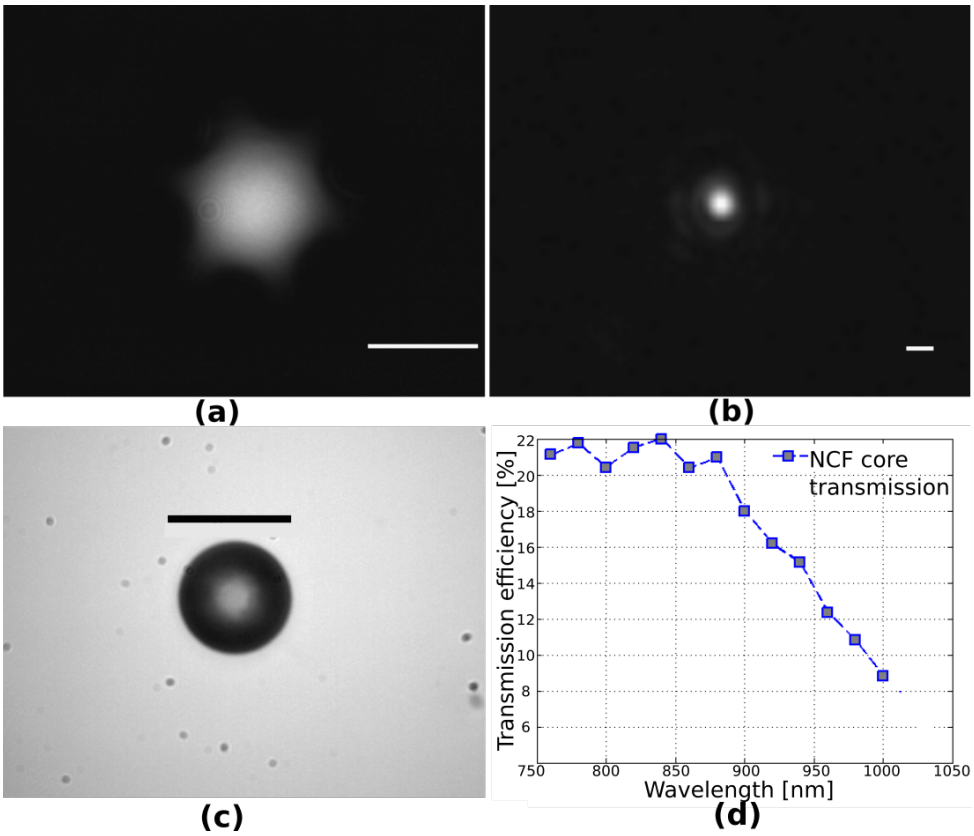

Figure 3.11 Silica microsphere focusing of the NCF core output beam. Field modal area of a beam exiting the fiber core (a), focal spot after the microsphere placement (b), a silica microsphere on a coverslip (c). Transmission efficiency (from the point of coupling until the sample plane) through the NCF with the microsphere and the mini-objective (d).

portable probe, we sealed it in the fiber core by means of a CO_2 laser. By heating up the fiber inserted microsphere, we preserve its focusing properties, as will be described in Ch.5. Lastly, we measured the transmission efficiency of the NCF core with the focusing microsphere and the mini-objective. Figure 3.11d shows the transmission of a 1.5m long NCF piece. A 40x Olympus objective with 0.6 NA was used to couple laser light in the fiber core. We measured the NCF input and output powers with a power meter (Coherent) in the spectral range of 760-1000 nm. The output to input ration varied from 22 $\%$ for 800 nm down to 9 $\%$ for 1000 nm. This difference in transmission efficiency is due to the mini-objective coating adapted for the emission spectrum (500-700 nm). Nevertheless, we conclude that this endoscope-like configuration enables the delivery of high power excitation beams.

3.2.3 Non-resonant CARS background

In the previous chapter (sec.2.4.3), we discussed the FWM generated by the pump and Stokes beams in the Kagomé fiber. It was therefore very important to perform the same study on the NCF. The setup for FWM measurements is the same as depicted in Fig.2.8 (except for the fiber). In this experiment, we sweep the delay over 2 ps and take the temporal overlap on the olive oil sample as the zero position delay. The fixed wavelength output from the Coherent Discovery laser beam serves as the Stokes (1040 nm) and an OPO generated 800 nm beam is used as the pump. A PMT detects the forward generated CARS signal from olive oil at 20 mW total average power on the sample ($P_{\mathrm{S}} = 10$ mW, $P_{\mathrm{p=10}}$ mW). In forward detection a neutral density (ND) filter passes only 0.1 $\%$ of the incident light. In Fig.3.12a), the red solid curve represents the CARS olive oil signal. The solid blue curve corresponds to the situation, when the olive oil sample is out of focus. In forward direction, we have found only a small peak of FWM generated most probably by the focusing microspere. This peak is well separated by $\sim$500 fs from the CARS olive oil signal due to the GVD of the relaying mini-objective lenses. A similar trend can be traced in the case of epi-detection (Fig.3.12b). Although invisible in forward detection, an additional FWM contribution appears at the sample temporal overlap, this FWM background is 10 times lower than the epi-CARS generated signal.

3.3 NCF's improved signal collection

In this section, we will compare signal collection efficiency of the NCF and the Kagomé fiber. When referring to the Kagomé limitations (Sec.2.7), we recall its collection area to be 24000 $\mu\mathrm{m}^2$. The NCF's collection surface can be calculated as well (Fig.3.8). This fiber has a 30 μm hollow core, with six glass cylinders around it. The nonlinear crystal structure with the glass tubes attains only 60 μm, so the silica double-clad could now be much closer to the core. This will enhance the collection of photons from scattering tissues. With the external

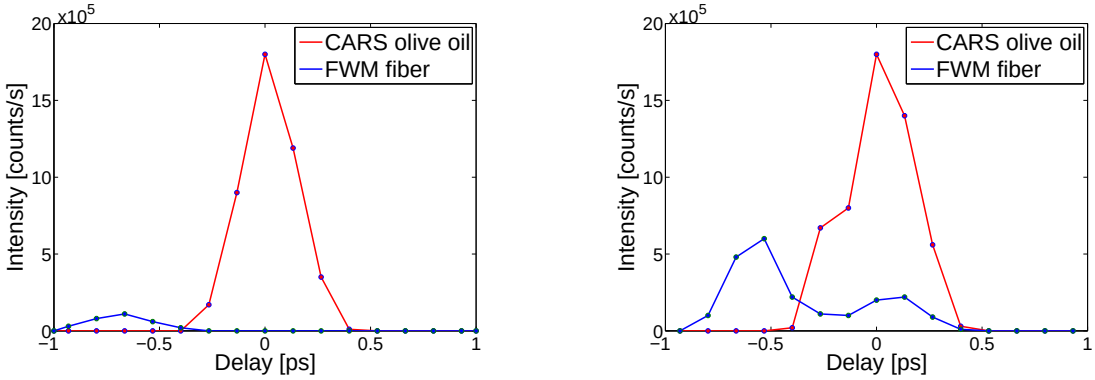

Figure 3.12 Fiber generated FWM and olive oil CARS forward (a) and epi (b) collected signal vs delay (the setup presented in Fig.2.8). The Stokes (1040 nm) and the pump (800 nm) beams were sent through the NCF (1.5 meter) with a 30 μm focusing microsphere inserted into its core. The focal spot is relayed on the sample plane by the miniature objective lens. Filters: 720 nm cut-off shortpass and 625/53 nm bandpass. Total power: 20 mW. The red curve represents the CARS signal from the olive oil sample. The blue curve corresponds to the FWM generated by the fiber and the microsphere.

diameter of the double-clad around 250 μm, we find the total collection area of this fiber: $S_{total} = \pi(R^2 - r^2) = 3.14(125^2 - 30^2) = 46237\mu m^2$. So, we have almost a 2-fold collection surface area increase with respect to the Kagomé.

The NCF and Kagomé collected SHG from rat tail tendon As the first indication of the enhanced collection, we compare the FWD and EPI detected TPEF signal from a cuvette filled with fluorescein solution (FITC). In Figure 3.13 we have illustrated a schematic of the setup built for this comparative study. The OPO (800 nm) beam was focused in the FITC cuvette by the relay mini-objective (WD=0.6 mm). A tight focal spot ($\sim 1\mu$m) was achieved with the focusing microsphere attached to the distal part of the fiber core. The TPEF signal emitted by the fluorescein sample was collected in the transmission-like scheme (FWD signal) and in reflection (EPI signal) by the fiber. In case of the Kagomé fiber the FWD/EPI signal ratio was around 200. With the 2-fold larger surface area provided by the NCF design, we have achieved this ratio to be $\sim$50. The results may seem somehow controversial since the sample was not scattering, so the emitted light must have been collected mostly by the hollow core. The latter is lossier in case of the Kagomé fiber. Another reason of NCF's collection improvement over the Kagomé could be the size of the silica structure (Kagomé mesh) around the fiber core. All the light incident on the Kagomé fiber mesh was lost (Fig.2.13). In contrary, the NCF design with minimal size of the mesh could have been in favour for better signal collection.

To inspect the improved collection, a strongly scattering sample was imaged in the same setup (Fig.3.13). This time the focal spot ($\lambda = 800$ nm) was circularly scanned over rat tail tendon (FOV$\approx$200 μm). We compared SHG images of collagen obtained with the Kagomé fiber

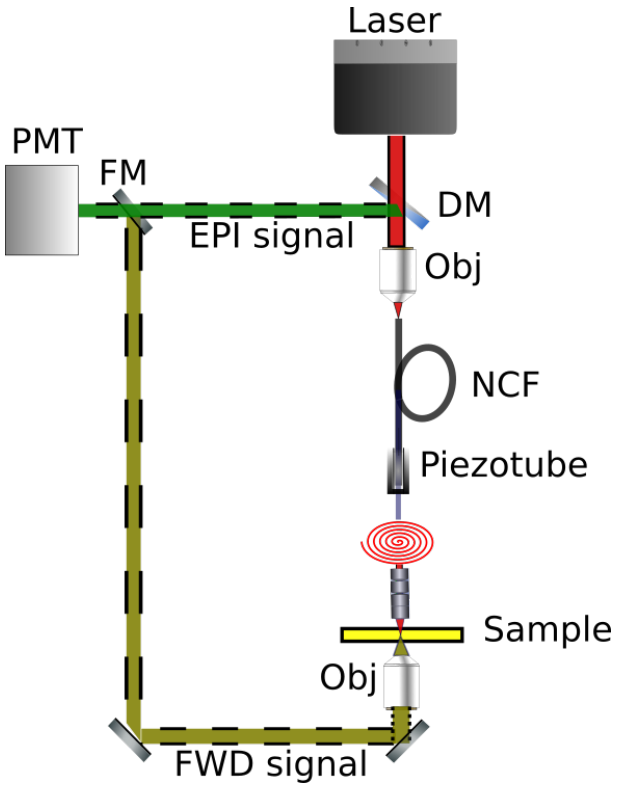

Figure 3.13 An illustration of the setup used to compare the collection efficiency of the Kagomé fiber to the NCF. The beam (Discovery, $\lambda = 800$nm) is coupled in 1 meter of NCF (with the focusing microsphere on the core) and resonantly scanned by the piezotube. The nonlinear signal (SHG, TPEF) is collected by the NCF double clad (EPI signal) and in transmission (FWD signal). DM: dichroic mirror ($\lambda_{\text{cut-off}} = 760$ nm, FM: flip mirror. Filters for SHG: shortpass (700 nm) and bandpass (400/10 nm). For TPEF: shortpass (700 nm) and bandpass (550/100 nm). Obj: 40x, 0.6 NA.

and with the NCF (Fig.3.14). Both images were taken at 40 mW average power on the sample with 1 frame/second rate. However, the selected zones on the sample were not the same for the NCF and the Kagomé collecting fibers. Thus, the forward generated SHG emission could have varied for different locations on the collagen sample.

The average intensity was measured from three areas of the sample (Tab.3.1). We observed a 2-fold SHG signal increase from the selected areas, when collecting with the NCF with respect to the Kagomé fiber case.

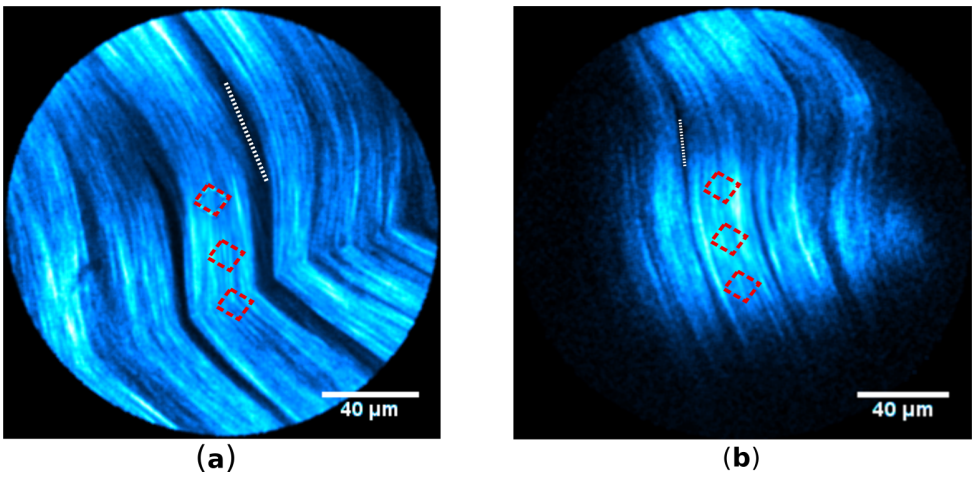

Figure 3.14 Qualitative study on the fiber collection efficiency of the Kagomé and the NCF. Collagen generated SHG images of rat tail tendon were obtained with two endoscope probes, Kagomé (a) and NCF (b) based. The locations where the SHG average intensity has been measured and reported in table 3.1 are delineated with the red squares (a), (b). The integrated background along the dash lines has been measured and reported in table 3.1. The awerage power on the samples is 40 mW. Images 10 times averaged.

Table 3.1 SHG rat tail images signal-to-noise (SNR) comparison of NCF vs Kagomé. I_{SHG} and I_{bgr} correspond to mean intensities of the SHG signal and the background. STD : standard deviation of the background (bgr).

Kagome	I_{SHG}, [a.u.]	75	75	65	I_{bgr}, [a.u.]	14	14	10	STD	3.2	4.0	3.9
NCF	I_{SHG}, [a.u.]	165	160	151	I_{bgr}, [a.u.]	21	20	21	STD	3.8	3.1	3.7

3.4 Conclusions

We have introduced a novel NCF with a large silica double-clad which replaced the Kagomé non-guiding structure around the fiber hollow core. We analysed the phenomena of antiresonance and inhibited coupling needed for lowloss light guidance in NCFs. The designed NCF enabled the delivery of SHG, CARS and TPEF excitation beams at high powers. The utrashort pulses

retained their short temporal width when delivered thorugh the NCF hollow core. We have demonstrated and supported by the FWM measurements, the applicability of the NCF for CARS imaging.

We have conducted a quantitative study on the signal collection improvement of the increased double-clad NCF. Firstly, we obtained a 4-fold increase in the collected TPEF signal generated from a fluorescein solution compared to the Kagomé fiber. Secondly, we performed a comparative SHG imaging of collagen tendons with the NCF and the Kagomé fibers. The SNR measurements also confirmed the NCF collection improvement. In the next chapter we will concentrate on the implementation of the NCF into a novel endoscope probe.

Chapter 4

Fast scanning endoscope development

In Ch.2, we have presented the Kagomé fiber based high resolution flexible multimodal endoscope and its application for ex-vivo CARS and SHG imaging. No dispersion precompensation mechanisms were needed to efficiently deliver ultrashort pulses through more than 1 meter of the fiber. Furthermore, due to the very low nonlinear refractive index of the air-filled Kagomé fiber core, CARS non resonant background from the fiber was found negligible, thus CARS imaging could be performed. However, there still was some room for possible improvements of the developed technology. We have identified the lack of signal collection efficiency of the double-clad (DC) Kagomé fiber for its application in TPEF imaging. In Ch.3 we have presented a novel double-clad negative curvature fiber (DC-NCF) with improved sensitivity in terms of signal collection due to its augmented collection surface area. On the other hand, for some applications we need to increase the scanning speed of the endoscope from 0.8 frame/sec to 8 frames/sec and more. This significant scanning speed increase will be used for in-vivo TPEF GFP-labeled neurons activity recording (see Ch.6). To this end, we will exploit a resonant braking of the fiber motion, in collaboration with Frederic Louradour and Pierre Leclerc from XLIM institute, who have gained an expertise in this domain. Due to the fiber resonant braking the time between two sequential scans will be strongly reduced. And by reducing the duration of a single scan from 800 ms to 125 ms, we will show in this chapter that we can reach the speed of 8 frames/sec.

We will explain the need of high frame rate imaging and describe the piezo-electric tube based fiber resonant scanning mechanism in Sec.4.1. The necessary hardware as an acquisition board and voltage amplifiers, as well as the appropriate custom-programmed software will be presented in Sec.4.2.

4.1 The scanning mechanism

A free standing cantilever of an optical fiber threaded in a piezo-electric tube behaves similarly to a driven harmonic oscillator. If a low voltage (<30V) is applied to the piezotube, the fiber tip lateral displacement attains only several micrometers. However, if driving this fiber tip at its mechanical resonance frequency, the displacement of the fiber tip can reach hundreds of microns. Thus, in order to maintain this high amplitude of the fiber tip deflection, and to make a symmetric 2D scan, x and y axes should be driven simultaneously close to their mechanical resonances. This condition excludes the possibility to exploit the standard raster sample scanning used in microscopy. In this section, we will describe the mechanisms of fiber resonant scanning and fast braking of this motion. This will also include a description of the new quartered piezo-electric tube, its application and performance for high frame-rate imaging.

4.1.1 Requirements for high frame rate imaging

In Ch.2, the mutimodal endoscope based on the DC-HC Kagomé fiber can scan at a speed defined by the fiber resonant expanding time (0.8 s) plus the time needed for the fiber to stop moving (0.5 s). This establishes 0.8 frames/sec imaging rate with the endoscope presented in Ch.2. However, this may not be sufficient for some applications requiring a faster image update. In neuroimaging, for instance, in order to record calcium bursts from activated neurons, it is inevitable to increase temporal resolution by at least 10 times [103].

The methods for resonant fiber braking have been described well by Seibel *et al.* [62]. On the other side, a very good practical application of fiber resonant braking was shown by Ducourthial [63]. Thus, during my PhD work we have collaborated with Pierre Leclerc from Frederic Louradour's group (XLIM institute) to implement this for our endoscope. The combination of our study on the theoretical aspects of fiber resonant scanning and braking on one hand, and the practical experience gained at XLIM on the other hand, allowed us to speed up the new endoscope to 8 images/sec. This speed can be further increased if the FOV is decreased. We will discuss in detail the braking principle and the relation between the scanning speed and the FOV in the following sections.

4.1.2 The piezo-electric tube

There exists a variety of quartered piezo-electric tubes on the market. We have made our choice in favor of a micro-tube from Physik Instrumente (PI). It is 10 mm long, with 1.5 mm outer (OD) and 0.9 mm internal diameter (ID). This choice was dictated first of all by the need of the endoscope probe miniaturization. On the other hand, we wanted to maintain high fiber deflection amplitudes as it was in case for the larger piezotube used in [69] (30 mm long with the outer and inner diameter: OD=3.2 mm and ID=2.2 mm). These piezotubes are made of the ceramic

type PIC255. It is a modified Lead Zirconate Titanate (PZT) based piezo-electric material. It is split in four isolated electrodes, which we use in pairs to generate desirable displacement in the two lateral directions (see Fig.4.1). The inner surface of the tube can be used as ground. The

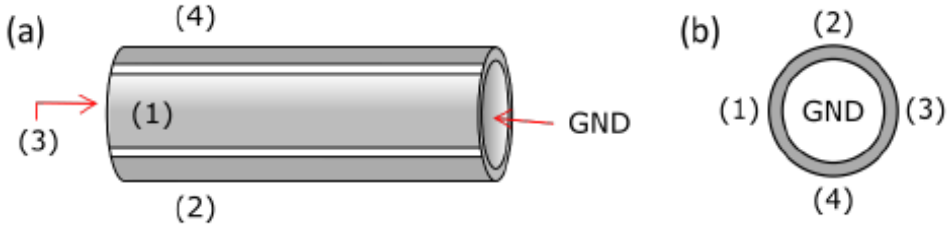

Figure 4.1 Piezotube basic scheme. Laterally (a) and axially (b) viewed piezotube are shown. The numbers indicate the isolated electrodes with ground inside of the tube. Image taken from [69].

working principle of a piezo-tube is based on its dilation or compression depending on the sign of the applied voltage. If a positive potential difference (with respect to the ground) is applied to one of the four electrodes, the tube will bend into the opposite side of the applied force. By changing the sign to negative, the piezotube will be bent towards the applied voltage (Fig.4.2). Thus, in order to maximize the deflection amplitude, one should drive a pair of opposite electrodes, say 1 and 3, 2 and 4 (Fig. 4.1) with opposite sign voltage waveforms. We can calculate the fiber lateral displacement knowing the geometrical and mechanical characteristics of the piezotube:

$$\Delta y(t) = V_y \frac{2\sqrt{2} d_{31} L^2}{\pi D h} \tag{4.1}$$

As an example we have picked the y axis piezotube displacement triggered by a voltage $\mathrm{V_y}$, where $\Delta y(t)$ corresponds to the induced displacement in y-axis, and d_{31} stands for the piezoelectric constant, which for the PIC255 ceramic becomes $\mathrm{d_{31}} = \mathrm{pC/N}$. The piezotube length L (10 mm), outer diameter D (1.5 mm) and the tube wall thickness h (0.6 mm). With a constant static voltage $\mathrm{V_y} = 30$ V applied, one can compute the piezotube deflection to be ~ 0.5 μm (whereas it was 1.2 μm with the big tube [69]). Therefore, with the new piezo, in theory we lose a factor of 2.5 in terms of the displacement amplitude, compared to the previously used big piezotube. So, first of all, the piezo applied voltage has to be doubled to compensate for the amplitude reduction. And more importantly, this piezotube should be driven at the resonant frequency of the combined piezotube and free-standing fiber tip.

4.1.3 Fiber spiral scanning

In nonlinear microscopy, a standard type of beam scanning is raster scan. The focused beam is translated from point to point in a line along x or y axis. Typically, in the case of resonant galvo-scanners, the beam moves quite fast at resonance in one axis and much slower in the other one. This scanning modality is hardly applicable for a piezotube-based scanner, because both

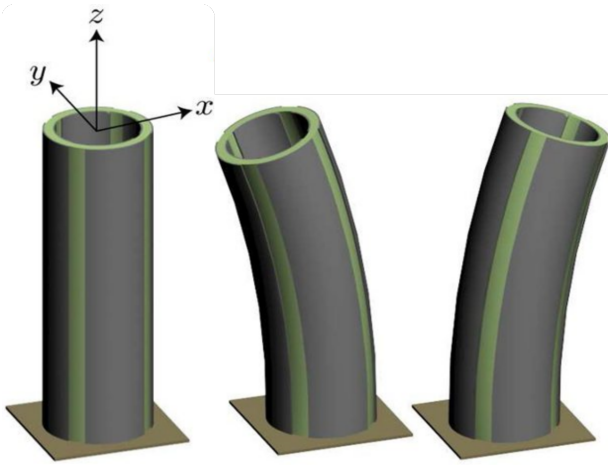

Figure 4.2 Piezotube deflection as a function of the applied voltage. Image taken from www.piezodrive.com.

the axes have to be driven at resonance for large FOV. In endoscopy using piezotube technology a spiral or circular scan can be implemented by applying a driving waveform with a sinusoidal envelope. A special attention should be payed to the scan pattern corrections, mainly because of asymmetric behaviour of the two axes of the piezotube scanner. Moreover, at resonance the two axes are coupled, which complicates the control of them.

We should consider several aspects inherent to fiber resonant scanning. One of the common concepts for scanning-tip endoscopy is a combination of three different parameters of resolution [106]:

- **mechanical resolution**
- **optical resolution**
- **numerical or sampling resolution**

The so-called **mechanical resolution** defines the distance between two adjacent circles, and is resonance frequency dependent (see Fig.4.3). In its turn, the resonant frequency is quadratically proportional to the length of a free standing fiber tip. In our case, at 11.0 mm length of the free standing NCF, the resonant frequency was around 1.6 kHz. Meaning, that 1600 circles can be produced in 1 second. To achieve 10 frames/sec imaging speed one would have 160 circles to complete one image frame and to stop the fiber. Thus, when increasing the diameter of a circular FOV, the distance between the adjacent circles increases as well, $\Delta\mathbf{res}_{\mathrm{m}}$ in Figure4.3. This can lead to an undersampling for large FOVs. The **optical resolution** is given by the optical system's PSF ($\Delta\mathbf{res}_{\mathrm{opt}}$ in Fig.4.3). We estimated it to be ~ 0.8 μm for the NCF endoscope. The detection sampling rate defines the distance between the two neighbouring points ($\Delta\mathbf{res}_{\mathrm{s}}$ in Fig.4.3). This **numerical resolution** depends merely on the acquisition card's sampling speed.

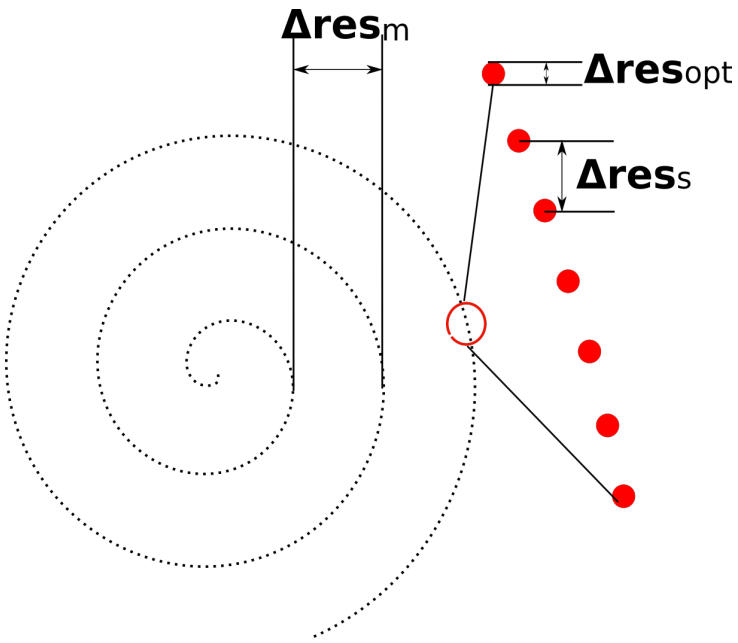

Figure 4.3 Three different concepts of circular scan resolution. Image redrawn from [106].

Free-standing tip An externally driven harmonic oscillator can be considered as a classical model for fiber resonant scanning. When driving a free standing cantilever Fig.4.4 at the resonance, its frequency response is characterized by a peak that has a Lorentzian shape [69]. The resonant frequency f_{res} of such an oscillator can be approximately estimated by the equation:

$$f_{res} = \frac{\beta}{4\pi L^2}\sqrt{\frac{ER^2}{\rho}} \tag{4.2}$$

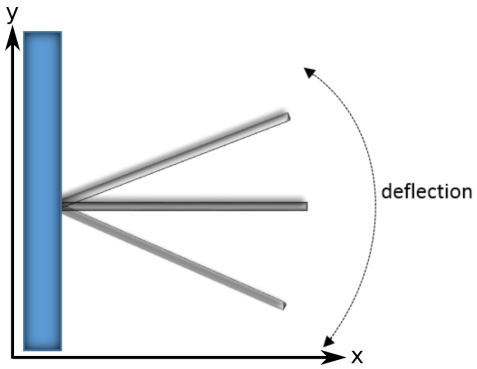

Figure 4.4 A model for fiber resonant scanning. At one end the fiber is fixed and at the other end it is free to move. With a mechanical strain induced by an applied voltage V_y the fiber end swings in the y-direction.

The frequency response is characterized by a series of peaks, with resonance of increasing

order occurring at increasing frequencies. In this equation, β is a constant, which depends on the resonance order, E stands for Young's modulus of silica, R is the fiber radius and ρ the volumetric mass density of the fiber. L stands for the fiber free-standing tip length. In Ch.5, we will describe an integrated NCF based probe, where the free-standing fiber length L=11.0 mm. The maximum fiber displacement was observed at a resonant frequency f_{res} ≈1600 Hz. We have done some preliminary studies on the double-clad (DC) NCF resonant frequency and fiber displacement amplitude. These two parameters were measured for a piece of the NCF with and without the polymer shell around it. The experiments were done in Limoges at XLIM institute.

A short piece of the NCF was fixed with a magnetic clamp on a shaker unit (Fig.4.5). This device can perform a test sample shaking proof at different frequencies. The main goal of these tests was to find an optimal length of the free-standing NCF. Ideally, we wanted to work at around 1500-1600 Hz (1500-1600 circles per second), in order to provide a sufficient number of circles for an accurate sampling over at least 200-300 μm FOVs at 8 frames/sec, preserving at the same time high deflection amplitudes.

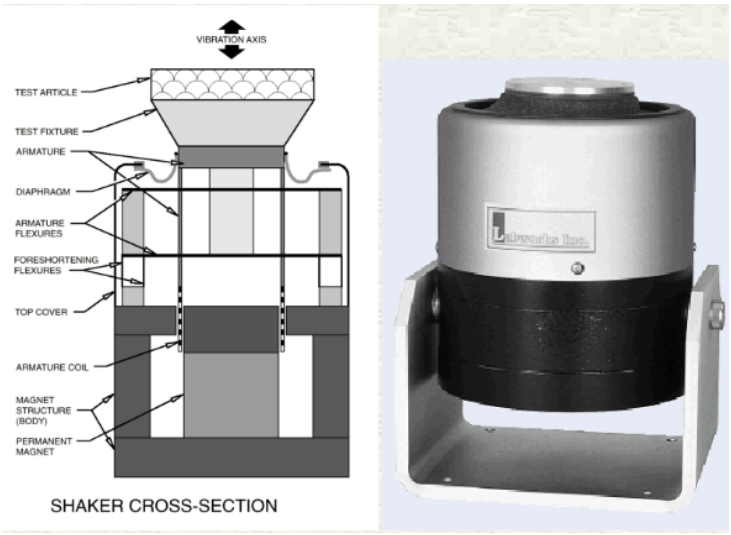

Figure 4.5 Shaker unit. This vibration inducing device was used to measure the resonant frequency of the NCF free-standing tip of different legnths. Image taken from [http://lgros.chez-alice.fr].

For the first trial, we kept the free-standing tip L=12.5 mm. The DC-NCF has a thick outer polymer shell (>400 μm) for fiber mechanical protection. However, this polymer shell alters the oscillatory behaviour of the free-standing tip, since it has a different set of parameters (ρ, E, R) as compared to a pure silica fiber. Thus, we have compared the resonant response to an external drive of the NCF of the same length with and without the polymer shell (Fig.4.6). We noticed a tendency of the NCF free-standing tip with the polymer to have lower resonance frequencies and displacement amplitudes as compared to the stripped polymer NCF. We conclude, that for the sake of higher resonant frequencies and displacement amplitudes, one needs to strip the fiber. In addition to what was said with regards of DC-NCF light confinement, when having the

polymer shell stripped, light is still kept in the silica double-clad, being surrounded by air.

From Fig.4.6, we find the resonance frequency of less than 1 KHz for 12.5 mm free-standing NCF. In Eq $(4.1.3)$, the resonance frequency is inversely proportional to the length of the free-standing tip L^2. Thus, in order to have a 1.6 kHz resonant frequency, we decided to decrease the free-standing length to 11.0 mm. This led to a resonant frequency of 1590 Hz for the free standing NCF.

Resonant driving waveforms In an ideal case, if a sinusoidal driving waveform was applied to x and y axes of the piezotube, with a phase shift of $\pi/2$ between them, a perfect circular scan would be generated (Fig.4.7). In reality, the resonator (piezotube with the free-standing fiber) is characterized by a non-symmetric behaviour caused by slight imperfections inherent to almost every stage of the probe integration (glue distribution, electrodes soldering, etc.), as well as by the piezotube quadrants of slightly different radii. An appropriate correction needs to be developed as described below.

Coming back to the ideal case, the driving waveform would swing the fiber tip with a certain displacement during the time it is applied. This voltage waveform can be analytically presented as:

$$\mathrm{V_x(t)} = \mathrm{V_{max}} \cdot \sin(2\pi \mathrm{f_{mod}} \mathrm{t}) \cdot \sin(2\pi \mathrm{f_{res}} \mathrm{t}) \tag{4.3}$$

$$\mathrm{V_y(t)} = \mathrm{V_{max}} \cdot \sin(2\pi \mathrm{f_{mod}} \mathrm{t}) \cdot \cos(2\pi \mathrm{f_{res}} \mathrm{t}) \tag{4.4}$$

Where $\mathrm{V_{max}}$ corresponds to the maximum delivered voltage and $\mathrm{f_{mod}} \ll \mathrm{f_{res}}$, with $\mathrm{f_{mod}}$ being the frequency of the slowly varying envelope. The applied voltage drives the scan during a time t:

$$\mathrm{t} \leqslant \mathrm{T_{exp}} = \frac{1}{4\mathrm{f_{mod}}} \tag{4.5}$$

with $\mathrm{T_{exp}}$ corresponding to the duration of the fiber scan expansion. The fiber tip will continue to oscillate. Depending on the quality factor Q of the resonator, it can be more or less damped. Experimentally we note that the free standing fiber oscillation lasts for some hundreds of milliseconds before the returning to the center of the scan [69]. A new scan can be only started again, when the scanning fiber tip is completely halted. A way to decrease this relaxation time is to perform active braking, with this we will show that the relaxation time can be shorten from 500 ms to 12 ms.

4.1.4 Resonant braking

Fiber active braking is governed by the same principles of a driven harmonic oscillator. A mechanical strain induced by the applied voltage forces the free-standing fiber tip to oscillate. Let's call this strain - expanding strain. After the driving voltage is removed, the oscillating tip mo-

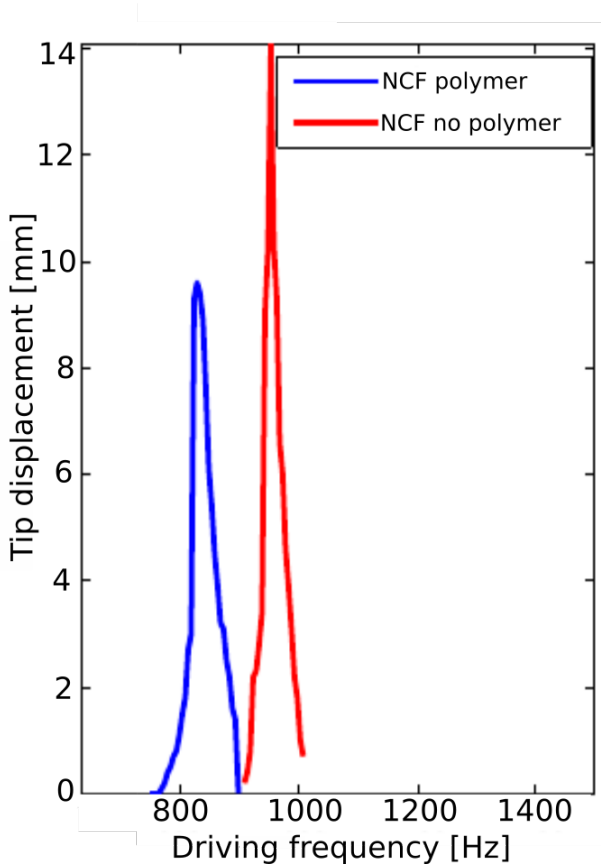

Figure 4.6 NCF resonant frequencies of a 12.5 mm free-standing NCF tip. A short piece of fiber (l=30 mm) was fixed with a magnetic clamp on a shaker unit. The curves represent the fiber deflection amplitude versus scanning frequency. The blue one corresponds to the NCF with the polymer layer around the silica double-clad (DC). The red one depicts the case of the NCF without the polymer shell.

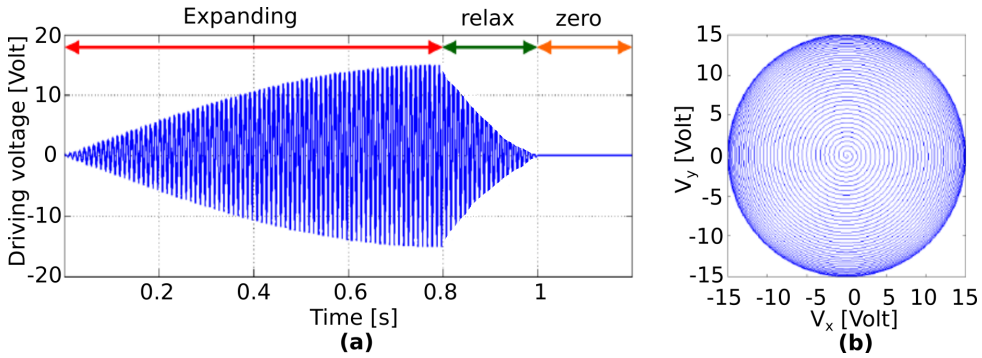

Figure 4.7 Driving voltage waveform without active fiber motion braking. During the period of expanding, the fiber filles a circular shape scan pattern with spirales, starting from the center of the circle, red arrow in (a). From 0.8 s till 1.0 s, the driving voltage removed, but the fiber end still moves, slowly decaying, green arrow (a). During the rest time, the fiber end returns to the center and stabilizes, orange arrow in (a). Afterwards, a new scanning cycle can be started (b) [69].

tion decays with its natural damping time. At this very moment, if another strain is applied with a frequency matching the natural damping frequency of the free-relaxing fiber tip (but with a 90 degrees phase lag to the expanding strain), the fiber motion can be quickly stopped. For convenience, let's call the second strain - braking strain.

The exploited motion braking procedure forecasts three main stages: 1 - fiber end at its maximum amplitude, 2 - braking strain halts the movement, 3 - the fiber tip rests during some short time needed to return to centre and to stop completely [63, 65, 66, 107, 108]. In Fig.4.8, we depict a numerical representation of driving waveforms for the fiber resonant movement braking [108]. In the very beginning, the fiber moves at its maximal displacement. At this moment, the braking strain is induced by a square-shaped driving voltage. The braking time can be reduced by increasing the braking voltage. In this work, we managed to completely stop the fiber movement in 12 ms, which at 1600 Hz takes only ~ 19 spirals. However, some corrections and additional parameters must be introduced for a good control of the fiber resonant braking, in order to avoid discrepancies between two successive scans.

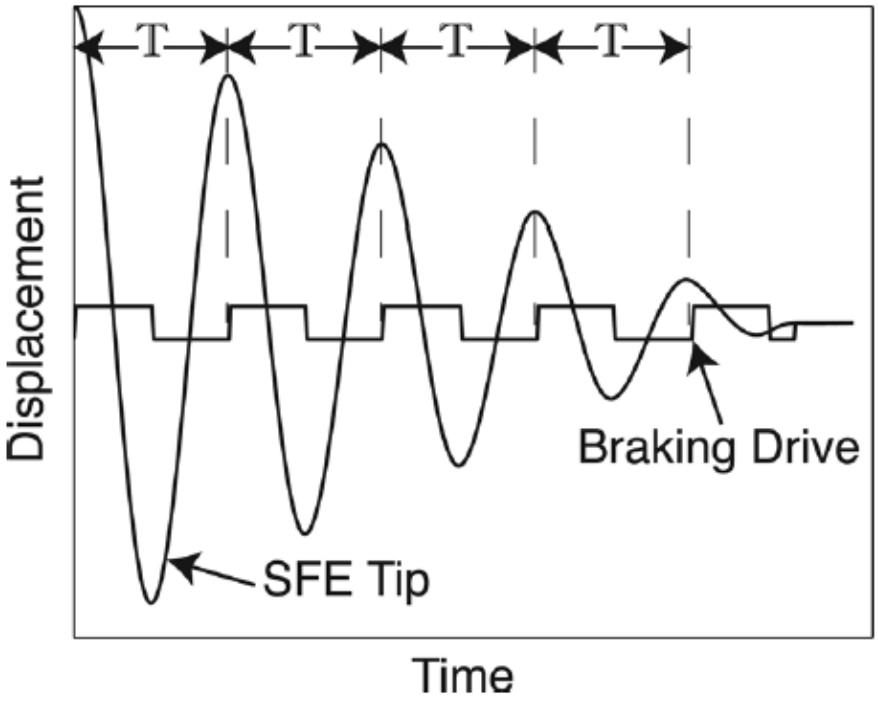

Figure 4.8 Scanning algorithm. Taken from [108].

4.1.5 The scan corrections

The theoretical principles of fiber resonant scanning seem clear, however, once it comes to practical applications, the system fails to thoroughly follow the commands. There exists a so-called transistory regime, when the fiber tip doesn't follow the driving voltage modulation curve [69].

This regime's duration is approximately equal to $\mathrm{Q}/\mathrm{f_{res}}$, as shown in [109]. It can degrade the image in the center, if assuming a perfect obeyance of the fiber tip to the drive during image reconstruction. However, an active feedback from the scan pattern can help to correct the distortions caused by the transistory regime. This feedback can be provided by a position sensing detector (PSD). The 2D displacement maps of the laser spot on the PSD are recorded and used to reconstruct the images. Besides, when driving only the y-axis, the fiber tip moves in the x-axis as well. This is caused by the fact that at the resonance the two axis are coupled. Furthermore, the resonant frequencies of the two axis are not the same, but differ by a couple of Hz, leading therefore to a non-circular scan pattern. However, there is a way to make appropriate corrections and finish with a perfectly circular scan. This difference of mechanical constants between the two axes is also present while considering a symmetric braking along the x and the y axis.

Expanding strain The coupling effect of the two axes at resonance is called whirling. When driving the free-standing fiber tip only in one axis far from the resonance, its displacement predictably occurs only along the driven axis, as can be seen in Fig.4.9a,c. In contrast, at resonance, the fiber displacement takes an elliptical shape. This effect complicates the control of the scan pattern. A well described solution for the whirling effect has been introduced [107], further developed and applied [69, 106, 109].

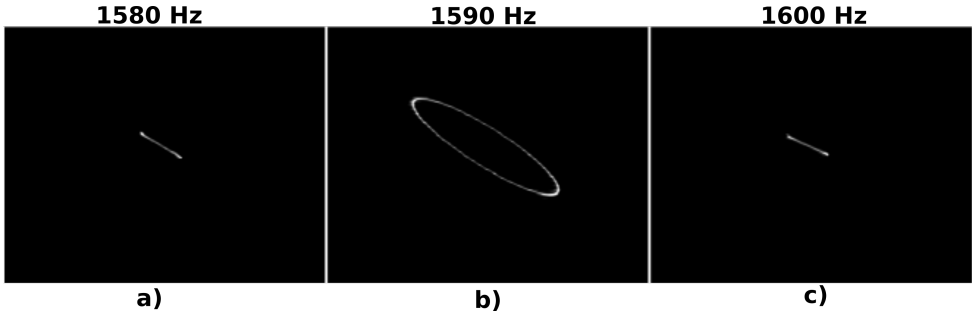

Figure 4.9 Resonant scan [69].

The mechanical resonator is composed of the fiber and the piezo, has another pair of completely decoupled axes, called eigen axes. One has to drive simultaneously both pairs of piezotube electrodes to excite the resonator along an eigen axis. The real axes (electrodes) coordinate system can be transformed into a system of so-called virtual axes rotated by an angle θ (Fig.4.10). The new coordinate system is then described by orthogonal vectors $\widehat{e_X}$ and $\widehat{e_Y}$:

$$\widehat{e_X} = \cos(\theta)\widehat{e_x} + \sin(\theta)\widehat{e_y} \tag{4.6}$$

$$\widehat{e_Y} = -\sin(\theta)\widehat{e_x} + \cos(\theta)\widehat{e_y} \tag{4.7}$$

The virtual electrodes $\mathrm{V_X}$ and $\mathrm{V_Y}$ have to be driven along the eigen directions $\widehat{e_X}$ and $\widehat{e_Y}$. In

order to drive only one virtual electrode V_X:

$$V_X(t) = \cos(\omega t) \tag{4.8}$$

with $V_Y = 0$ it is necessary to drive both real electrodes with the waveforms:

$$V_x(t) = \cos(\omega t)\cos(\theta) \tag{4.9}$$

$$V_y(t) = \cos(\omega t)\sin(\theta) \tag{4.10}$$

At certain angles θ which defines the eigen axes, the whirling effect disappeares and the fiber tip moves along a line (X or Y, Fig.4.11). An iterative process is used to determine the angle θ for driving the piezo solely along its eigen axis.

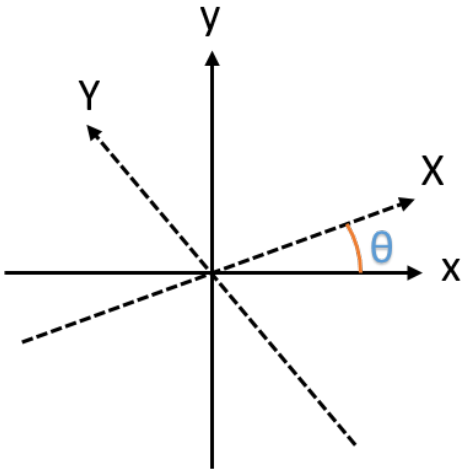

Figure 4.10 Real axes versus virtual.

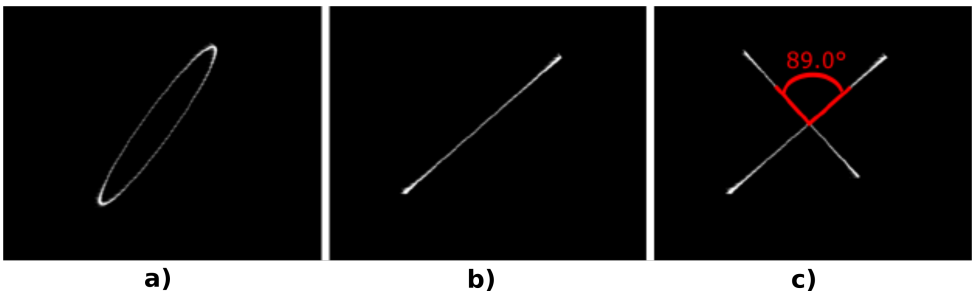

Figure 4.11 Fiber whirling motion at the resonance. The fiber end driven along the real electrode (y-axis, (a)). Whirling is compensated by driving along the virtual electrode V_Y (b). Superposed x and y axes in case of the two virtual electrodes V_X and V_Y separately driven (c) [69].

One more correction should be addressed in for the fiber resonant expanding. This one is related to a slight difference in the resonant frequency along the x and y axes. Fig.4.12

depicts the frequency response (in amplitude and phase) of a driven harmonic oscillator, whose mechanical resonant frequency differs in the x and y axes. The phase response shows a π phase shift when scanning in frequency through the resonance. At the resonance, the oscillator is 90 degrees out of phase with respect to the driving waveform. After the resonance, the phase lag becomes equal to π. If driving the fiber at a frequency residing in-between the two x and y resonances, an additional phase correction must be done. Otherwise, the angle between x and y axes will not be 90 degrees, resulting in an elliptical scan pattern.
This correction can be addressed by introducing an additional phase on one of the axes:

$$V_X = \cos(\omega t) \tag{4.11}$$

$$V_Y = \sin(\omega t + \phi) \tag{4.12}$$

It is possible to find an appropriate ϕ angle iteratively provided with a feedback on the scan shape by means of a PSD or a CCD camera.

In summary, in order to obtain a circular scan, we first find the resonant frequencies sweeping the driving frequency individually for x and y axes. Then, an appropriate value of θ must be identified, such that the orthogonal driving axes can be decoupled. If the resonant frequencies for x and y differ, a so-called relative phase ϕ has to be defined in an iterative manner and added to correct for the phase lag between the axes. In the end, if the deflection in one of the axes is stronger, we can compensate for it by slightly changing the driving waveform amplitude. Finally, it is possible to obtain a circular scan pattern (Fig.4.13).

The second stage deals with the braking corrections, which are meant to provide a minimal scan amplitude in-between two successive scans. Some of the expanding strain correction parameters are compatible with the braking ones (same θ angle). However, most of them should be separately considered.

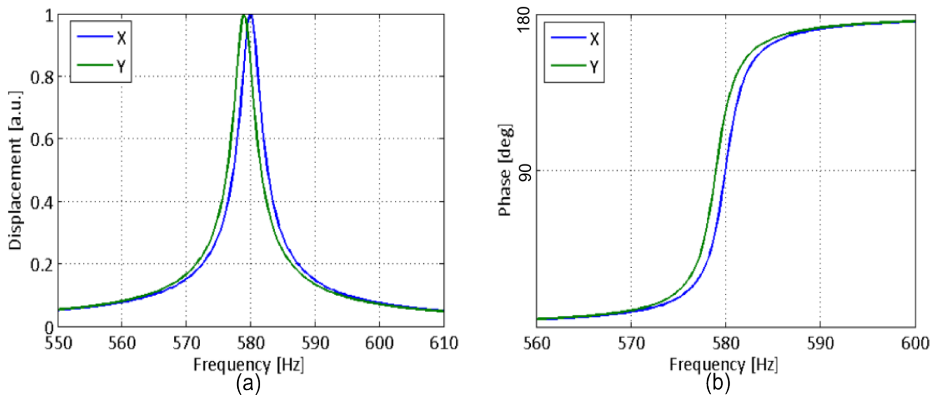

Figure 4.12 Amplitude (a) and phase (b) dependence when sweeping the frequency accross the x and y axis resonances [69].

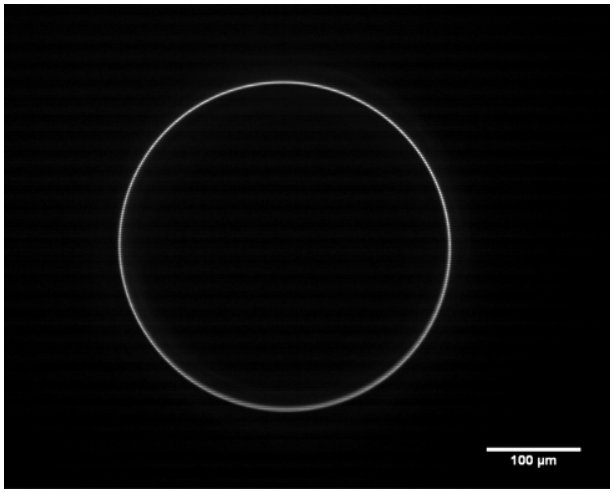

Figure 4.13 Round scan [69].

Braking strain Fiber resonant braking requires specific corrections. The θ angle remains the same as in case of the expansion strain, since the virtual electrodes of the oscillator are the same for expanding and braking. A new parameter shall be introduced which corresponds to a 90 degrees phase shift to the expanding strain called ϕ_{bphase}. Besides, in the case of braking, the two axis x and y are phase lagged in response to the braking strain. The compensation parameter for the phase difference between the x and y axis is called $\phi_{\mathrm{rel.brake}}$. These two phase parameters (ϕ_{bphase} and $\phi_{\mathrm{rel.brake}}$) are optimized in an iterative procedure.

The optimal braking times $\mathrm{t_x}$ and $\mathrm{t_y}$ can be a little different for the two axes. These times can be reduced by increasing the braking voltages $\mathrm{V_{brake}(x)}$ and $\mathrm{V_{brake}(y)}$. The final correction is meant to match the natural damping frequency of the relaxing fiber end with the braking strain frequency. Similarly to the situation with the braking times and amplitudes, the braking frequency is different for the x and y axes.

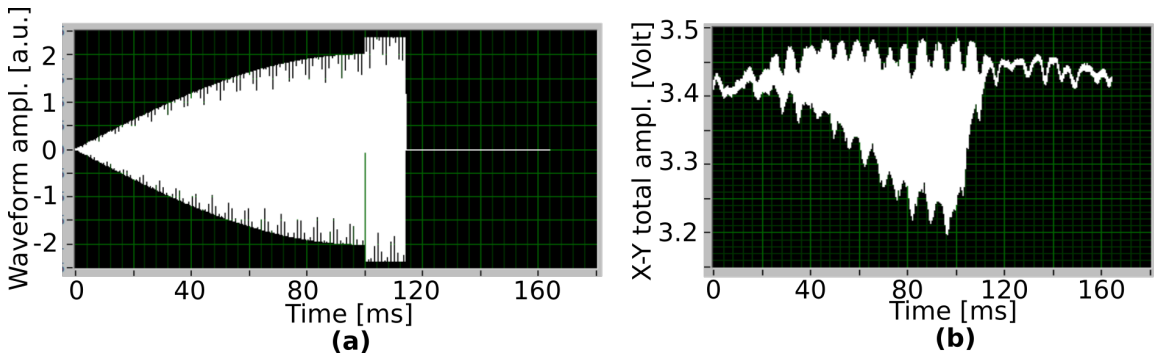

Figure 4.14 Fiber resonant braking measured with the PSD. Driving voltage profile versus the scan time (a). The sinusoidal waveform applied during imaging time (100 ms), followed by the linear profile for the braking (13 ms). The total amplitude of the scanning beam recorded by the PSD (b).

In summary, the braking procedure starts after the scan corrections have been introduced. At first, the braking voltage amplitudes ($V_{brake}(x)$ and $V_{brake}(y)$) are put equal to the amplitude of the expanding waveform. The braking times (t_x and t_y) are selected to be in the range of 10-20 ms. The braking frequencies ($f_{brake}(x)$ and $f_{brake}(y)$) are swept around the fiber resonant frequency ($f_{res} = 1600$ Hz) individually for x and y axes. By looking at the x and y axes braking amplitudes captured by the PSD, the coarse $f_{brake}(x)$ and $f_{brake}(y)$ can be found (Fig.4.15). The next step is to find the appropriate ϕ_{bphase} and $\phi_{rel.brake}$ in an iterative manner. The introduced corrections are followed by another cycle of fine tuning of the described phase and frequency parameters. Finally, the braking time and the residual amplitude can be minimized by tuning the braking voltages (Fig.4.16).

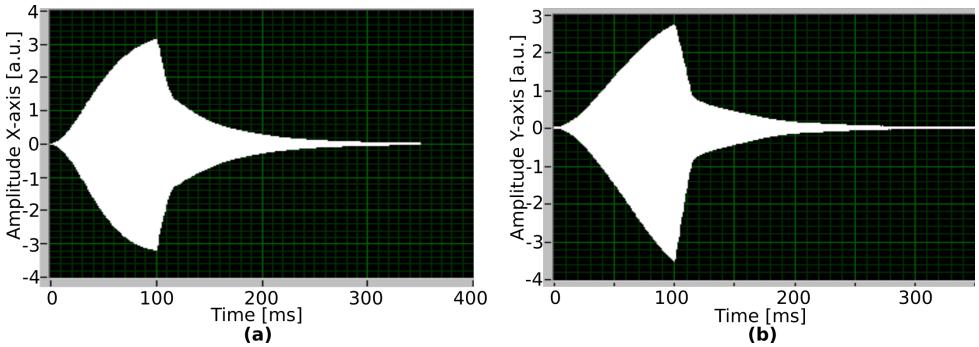

Figure 4.15 Fiber resonant braking measured with the PSD. The x and y axes fiber resonant expanding and braking is shown individually for each axis (a) and (b). The abscissa indicates time in milliseconds and the ordinate corresponds to the scan amplitude. During the expanding time of 100 ms the fiber is deflected, driven by the expanding strain. Imaging is performed from 0th until 100th ms. The braking activated from 100th ms until 113th ms.

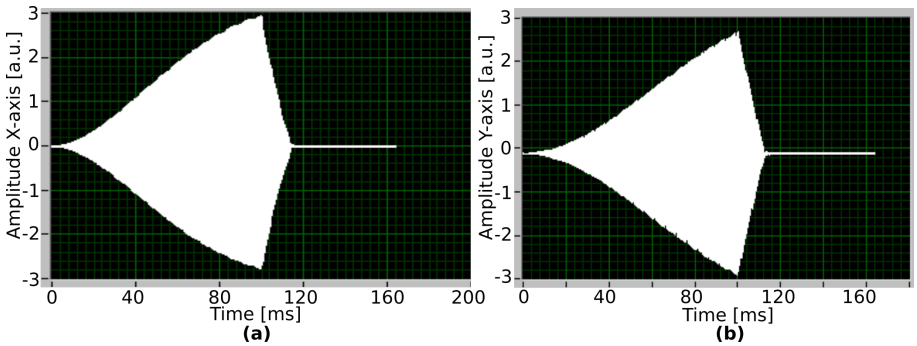

Figure 4.16 Fiber resonant braking measured with the PSD. The x and y axes fiber resonant expanding and braking is shown individually for each axis (a) and (b). The braking parameters well defined.

4.2 Hardware and software developement

The imaging control LabView programme as well as the Matlab algorithms for image reconstruction were written by Alberto Lombardini. I developed myself the high speed imaging softwares. In fact, when scanning at 8 frames/sec, the previously used LabView code was not optimal. It was working slower because of the execution of some unnecessary operations and verifications. The transmission of big data from the acquisition card to PC was not efficient as well. Thus, we had to review the main algorithm of the control code and to replace a USB (National Instruments) acquisition board by a much faster express PCIe National Instruments board.

Nevertheless, the main principles of image formation and reconstruction were maintained. This includes the simultaneous scanner driving and signal acquisition and the use of a position sensing detector (PSD) for the driving voltages mapping and calibration.

4.2.1 Open-loop imaging procedure

Generally, the fiber scan motion can be controlled with the so-called closed-loop and open-loop approaches (Fig.4.17). In the closed-loop, the scan's spatial positions are measured simultaneously with the sample generated signal collection and image reconstruction. However, there is no need to measure the positions for each successive scan. The stability and self-repeatability of the scan pattern allows to acquire only once a list of positions assigned to appropriate pixels of an image (open-loop). This set of positions is stable and can be used for a whole day of imaging. However, the scanner's frequency response may slightly drift with time because of temperature change. Thus, a day-to-day system calibration is usually required.

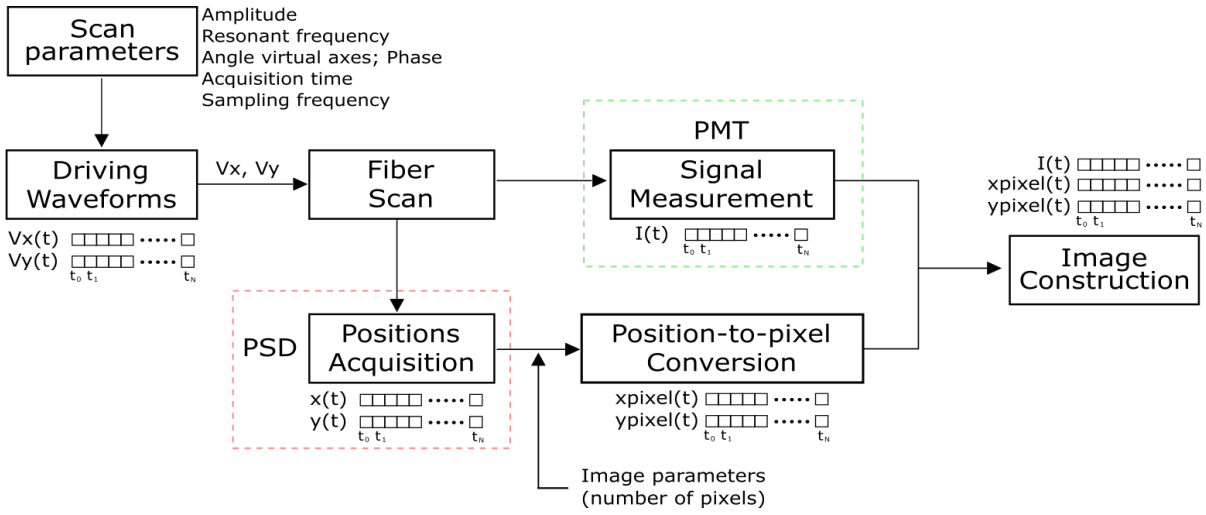

Figure 4.17 A schematical representation of the image construction algorithm. The first operation entitles the laser beam's spatial positions measurement and conversion to pixels. This list is then used to construct an image based on the signal captured by the detector (PMT).

4.2.2 Data acquisition device

Our data acquisition device (DAQ) executes two operations: voltage driving waveforms generation and simultaneous signal acquisition. At the beginning of my PhD work the used National Instruments USB acquisition card (NI-USB6351) could only drive two piezotube electrodes, as this board possessed only 2 Analog Output (AO) channels. The first demand for the DAQ was 4 AO channels, which would double the scanning amplitude once driving all 4 electrodes at the same time. The second and the more important requirement was the type of data transfer. USB acquisition boards of X-series (National Instruments) can transfer maximum 32 MB/s at USB 2.0 and 250 MB/s at 3.0. In comparison, a PCIe 6363 express board (National Instruments) employs another data transfer mechanism called Direct Memory Access (DMA). With this board the maximum of the data transfer speed attains 4 GB/s. Besides, this board has 4 AO channels and 16 analog input (AI) channels. To conclude on the chosen PCIe 6363 acquisition board:

- Max sample rate for 1 AI channel: 2.0 Msamples/s
- Max sample rate for 3 AI (positions acquisition) channels: 0.66 Msamples/s
- Max sample rate for 1 AO channel: 2.86 Msamples/s
- 4 AO channels
- 16 AI channels
- Data transfer: DMA (gather-scatter), max 4 GB/s.

4.2.3 Imaging software

The custom-written LabView software controlling the NI board was developed by Alberto Lombardini inspired by a Labview program of Patrick Ferrand (Institut Fresnel) [110].

The software performs two main tasks: scan pattern calibration and imaging. It synchronizes the driving voltage waveforms (scan generation) and the signal acquisition. This is done by an internal analogue trigger (NI board), which starts all the tasks at the same time. The sampling rate of the board is defined by the pixel clock. When working with analog signals (one-time voltage measurement), the sampling rate should be the highest possible, since it improves the signal to noise ratio (SNR). In contrary, digital channels store the number of delivered transistor-transistor logic (TTL) pulses (given by detected photons). Thus, the SNR does not depend on the sampling rate. However, the readout frequency should be high to keep up with the signal excitation speed to provide the correct intensity-pixel attribution [69].

For the fast frame/rate scanning, to speed up the imaging software, we had to remove all the computation operations from the main loop. All the intensity vectors built up and image display had also to be done outside the main loop. To increase the main loop execution speed, the Enqueue logic was used. Briefly, it works based on a so-called first-in first-out (FIFO) principle. The elements to read by the main loop are put in a queue, where the first added element is read

first an so on. This improvements in combination with a PCIe X-series (National Instruments) board have permitted to equalize the signal acquisition speed with the scan physical rate.

Positions acquisition and calibration The fiber tip trajectory is read out with help of a position sensitive detector PSD (PDP90A, Thorlabs). The beam from the fiber output is focused on the detector sensitive area of 9×9 mm^2. Three recorded analogue signals Δx, Δy and Σ represent the fiber spatial position in x-y axes, with Σ being the sum of the two. To provide correct position measurements avoiding detector's saturation, Σ voltage should be under 4V (Fig.4.18). The beam positions are retrieved using the equations:

$$\mathrm{x} = \frac{\mathrm{L_x} \cdot \Delta \mathrm{x}}{2 \cdot \Sigma}, \quad \mathrm{x} = \frac{\mathrm{L_y} \cdot \Delta \mathrm{y}}{2 \cdot \Sigma} \tag{4.13}$$

Where x and y correspond to the detected beam positions, L_x and L_y represent the size of the detector sensitive area (9 mm). If the three signal are acquired simultaneously at 250 kHz, it means that one measurement is taken every 4 μs. When imaging at higher sampling rates (1 MHz), we interpolate the position vectors, assuming them to be linear. Such that if the signal intensity is measured every 1 μs, it is attributed to a unique scan position. Resuling in a finer spatial sampling.

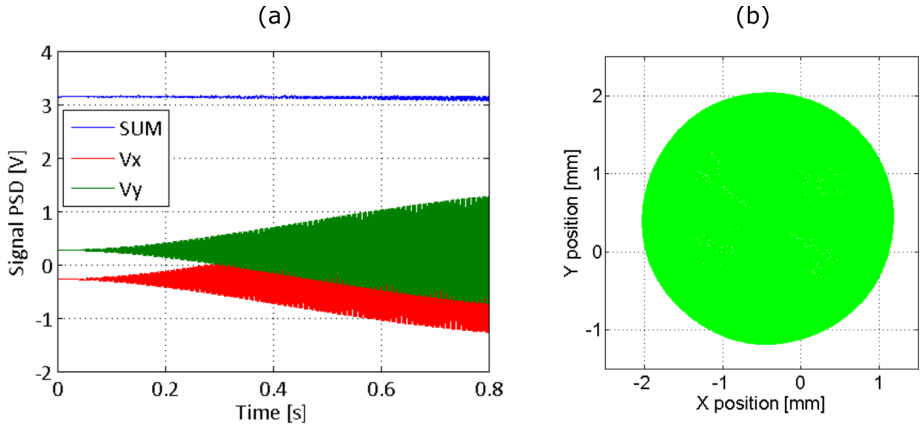

Figure 4.18 The PSD detected voltage traces. (a) The red and green curves correspond to x and y positions on the detector. The blue curve depicts the total incident intensity used for x-y signals normalization. The beam position in x-y plane (b). Image taken from [69].

Image reconstruction The image reconstruction is done *a posteriori* in a custom-written Matlab software. The number of pixels in an image can be chosen by the user. In order to avoid unsampled (empty) pixels, the number of pixels $\mathrm{N_{pixels}}$ should be selected in accordance with a relation: $\mathrm{f_{res}} \cdot \mathrm{T_{exp}} = \mathrm{N_{pixels}}$, where $\mathrm{T_{exp}}$ corresponds to the expanding wave duration (described in Eq.4.5). The excitation spot spatial coordinates measured with the PSD are stored

as a list of x-y scan coordinates transformed into pixels. The same scan pattern is reproduced on the sample. The nonlinear signal collected either by photon counters (PMTs) or analog detectors, is transferred to the NI board. Then an intensity vector which has the same size as the two spatial coordinates vectors is created. The synchronization between scan generation and signal acquisition allows for correct signal intensity attribution to corresponding pixel at any time t of the scan.

In resonant spiral scanning, the fiber tip moves slower in the centre and faster at the edge leading to unequal signal sampling. Uneven sampling in the centew of the image and at the periphery requires intensity normalization (Fig.4.19). For this purpose, we build two matrices: one with measured intensities and the other one with the number of measurements done for each pixel (sampling). After the vectors read-out, the intensity values are normalized by the pixel sampling matrix. A normalized image of a binary USAF-1951 resolution chart demonstrates the performance of the reconstruction procedure.

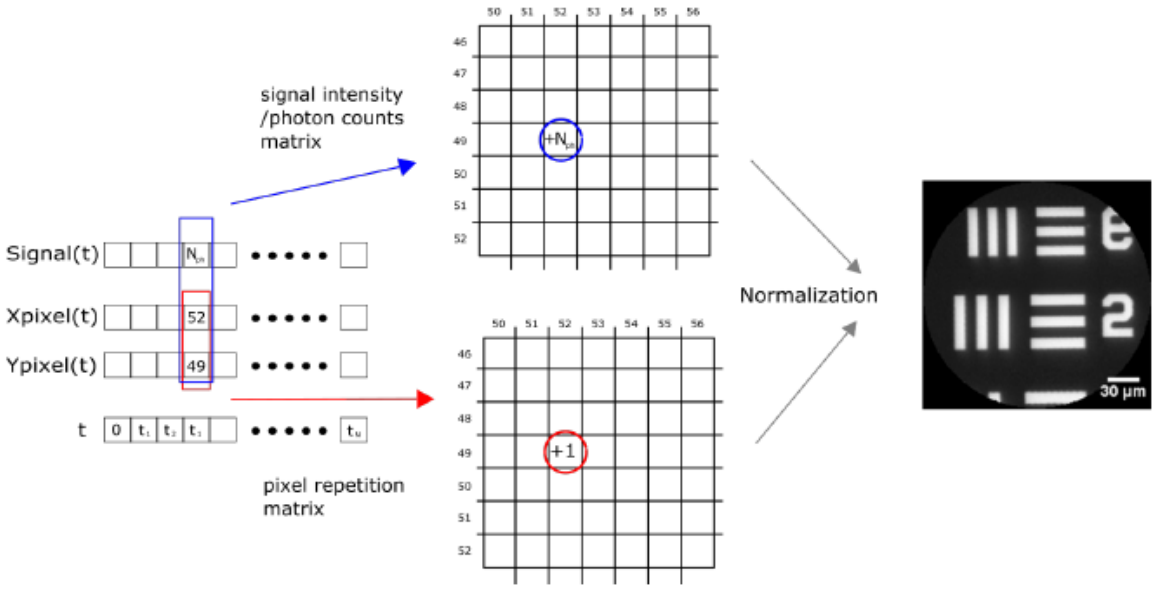

Figure 4.19 Image reconstruction algorithm. A pixel list is built from the spatial scan coordinates measured with the PSD. The measured nonlinear signal intensities are assigned to the pixel coordinates and normalized for each pixel. An example of normalized image from a USAF chart [69].

4.2.4 Voltage amplification

The NI board delivers 20 V peak to peak only: in order to achieve large FOVs we employ voltage amplifiers. Thus, we have ordered E-835.00 (DuraAct, Physik Instruments) broadband (>4 kHz) amplifiers, which can transform the NI board generated $\pm$10 V into -100 V and +250 V correspondingly. These amplifiers have been enclosed in a box (Fig.4.20). A simple and safe to use 5-pin adaptor terminates the 4 amplifiers output voltage and ground (Fig.4.21).

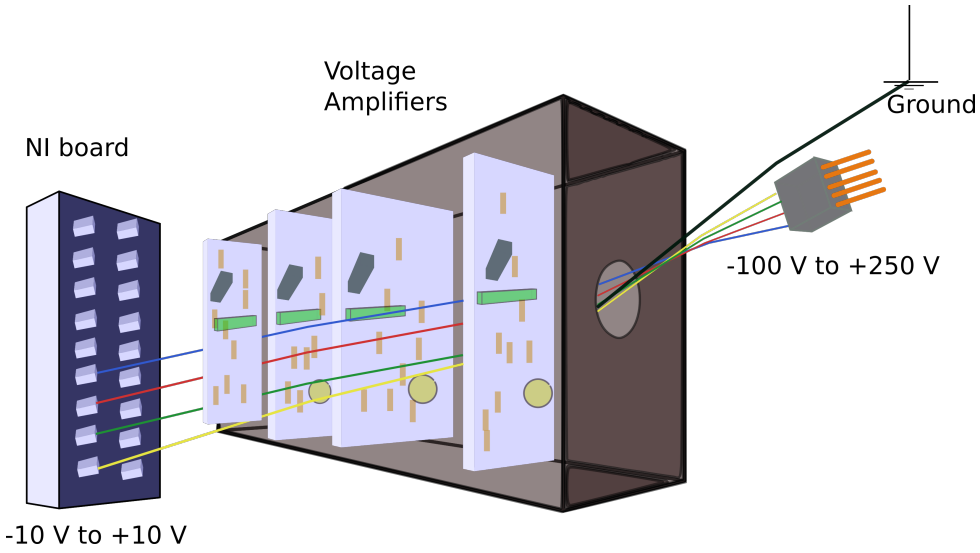

Figure 4.20 A schematic view of 4 voltage amplifiers (E-835.00 from PI) enclosed in an isolated box.

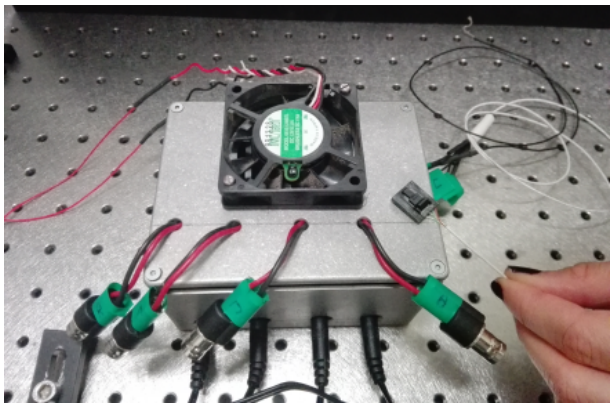

Figure 4.21 A photograph of 4 voltage amplifiers (E-835.00 from PI) enclosed in an isolated box with ventilation.

Off-axis aberrations We have examined the off-axis degradation of the focal spot for different FOVs. Since, if the beam intensity profile is changing along the scan area, this will result in a reduced sample excitation at the periphery. Thus a signal reduction at the circumference can be seen, once doing imaging in homogeneous solutions like fluorescein, for instance. From Fig.4.22, we can deduce that on the optical axis (center) the spot looks diffraction limited with the intensity profile represented by the Airy disk. Up to 250 μm away from the centre, the focused spot does not change. However, at 350 μm and further the beam profile degrades and becomes asymmetric. We can estimate a minimum aberration-free area of 500 μm diameter, which becomes a $\sim$315 μm circular FOV with M=0.63 of the mini-objective magnification [69].

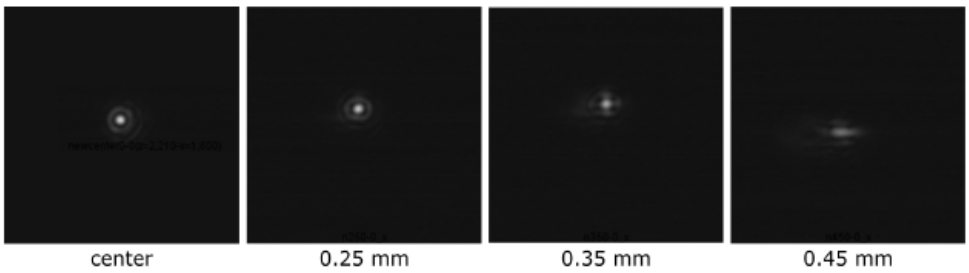

Figure 4.22 Off-axis abberation of the focal spot. The fiber is moved laterally with respect to the mini-objective. The beam intensity profile degrades significantly after being moved by more than 350 μm [69].

4.3 Conclusion

In conclusion, the demand for the scanning speed and signal collection increased miniaturized endoscope has been met. Starting with a new 1.5 mm outer diameter miniature piezo-electric tube, we have developed a methodology and a technology to generate, control and correct a spiral scan of the fiber tip. The high frame scan condition was fulfilled by developing the fiber motion resonant braking. All the necessary corrections for the scan repeatability were described. A custom-made software and the appropriate hardware were implemented. With the developed scanner, the mechanical properties of the NCF, as its resonant vibration frequency were studied and characterized. This resulted in an imaging endoscope performing images with a resolution of 0.8 microns over a field of view of 350 microns with a speed of 8 frames/s. In the next chapter we will incorporate this scanning unit into a 2.2 mm diameter distal endoscope probe and present the first CARS imaging results.

Chapter 5

Design and assembling of a prototype

We dedicate this chapter to the integration of a miniaturized portable probe, whose working principle was described in Ch.4. The integrated probe design was conceived at XLIM institute (Limoges, France). As a result of our collaboration with Frederic Louradour and Marc Fabert, we were able to tailor their technological know-how to our particular demands dictated by the desired design of a probe. In Sec.5.1, we recall the main requirements for the probe. We will discuss the importance of the silica microsphere sealing on the fiber core in Sec.5.2. Then we will move to the probe integration protocol (Sec.5.3). And finally, we will present the results of the first tests of the integrated probe in Sec.5.4.

5.1 Miniature scanner design requirements

In order to access different hollow organs with the endoscope distal part as thin as possible, we have scaled down the size of its components without negative consequences on the imaging performance.

Piezo-electric tube The endoscope we described in Ch.2 consists of a piezotube of 3.2 mm external diameter. In order to miniaturized the probe, we have chosen to use a quartered piezo-electric tube (microtube, PI, Germany) of 1.5 mm (outer diameter, OD), 0.9 mm (inner diameter, ID) and 10 mm length.

Mini-objective external shell We have already described the custom-designed mini-objective in Sec.2.3. There are four 2-mm thick lenses in this mini-objective that have to be stacked up in its assembly. The only requirement for this mini-objective is to have the possibility to be dismounted when needed. We have retained a biocompatible metal tube holding the mini-objective

and threaded into the probe body. With this design, the mini-objective is easily accessible for cleaning or replacement.

5.2 Silica microsphere sealing on the fiber

The silica microsphere focuses a 20 μm diameter modal area from 30 μm fiber core into 1 μm spot, increasing the core NA from 0.02 to 0.4. With this we have shown (Ch.3) that it is possible to perform high resolution imaging over >300 μm FOVs. Such a glass microsphere can be attached to the fiber core just by simple pressure between the fiber output facet and the targeted microsphere deposited on a substrate. The microsphere is then held inside the core by electrostatic forces. It remains in the core even at high deflections of the fiber tip during imaging. Nevertheless, for the integrated probe, in order to make sure the microsphere remains firmly attached to the the fiber core, we have fused it to the fiber core by means of a CO_2 laser splicing system. This task was done at IRCICA institute (Lille, France) in collaboration wih Alexandre Kudlinski and Damien Labat (IRCICA).

Laser splicing CO_2 lasers are frequently used for glass materials processing including optical fibers. A typical CO_2 laser emits at 9.4 μm. This electromagnetic radiation can be absorbed by glass and transformed into heat, which in turn will melt the glass.

We used the LAZERMaster LZM-100 Laser Splicing System provided by Association France Laser (AFL). With help of the LZM-100, optical fibers can be spliced, tapered, etc. A CO_2 laser used in this system provides a good control on the heat affected area. Thus, we were able to slightly melt the silica microsphere, preserving its spherical shape for an aberration-free focusing at the fiber output. At the same time, the fiber cladding glass tubes structure surrounding the core was not affected by the heat.

A view of the microsphere sealing is shown in Fig.5.1. The NCF with the microsphere sealed in its core appears from the left hand side. The CO_2 laser is focused over a 300 μm area (from x and y directions). A single mode fiber (SMF) on the right serves as a local heat source in front of the microsphere. The effect of local heating in SMFs appears when a high power radiation incident to the fiber reaches a certain threshold [111]. If the optical power exceeds the threshold, the fiber absorption will be strongly increased due to the thermal effect and it will fuse in the opposite direction to the applied illumination. However, if the optical power limit is not broken, the fiber will absorb the radiation transforming it into heat and transfer the generated heat forward (on the glass microsphere in our case).

We had to adjust the machine parameters, for example the laser radiation intensity, its duration or the distance between the NCF and the SMF. These parameters were not the same as for the case of the previously used Kagomé fiber sealing. There are several reasons for that. First of all, the NCF had a much bigger silica double-clad, hence it was absorbing more the CO_2

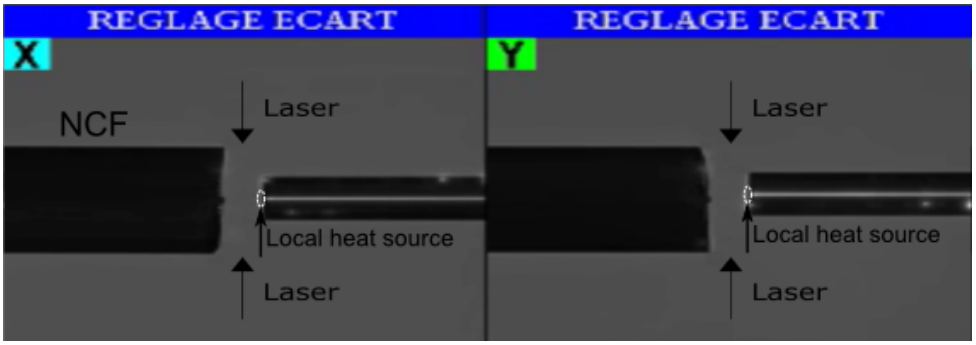

Figure 5.1 Silica microsphere sealing on the NCF core. LAZERMaster LZM-100 Laser Splicing System (AFL) with a CO_2 laser provides a perfect control on the sealing procedure. Minimal exposure time and radiation intensities chosen for a careful microsphere attachment. Two orthogonally placed cameras give a good lateral overview on the local heat source SMF and the NCF with the microsphere on its core.

laser light. Secondly, the structure around the fiber core in the NCF and the Kagomé fiber differ significantly. We tuned the parameters such as the laser radiation intensity and duration up to the point, where the microsphere is fuses to the glass tubes around the fiber core, but with its spherical frontal shape well preserved. The final result is presented in Fig.5.2a. The focal spot made by the sealed microsphere was less than 1.5 μm (see Fig.5.2b). SEM photographs of the NCF cross-section (Fig.5.3a and Fig.5.3b) demonstrate the quality of the sealing.

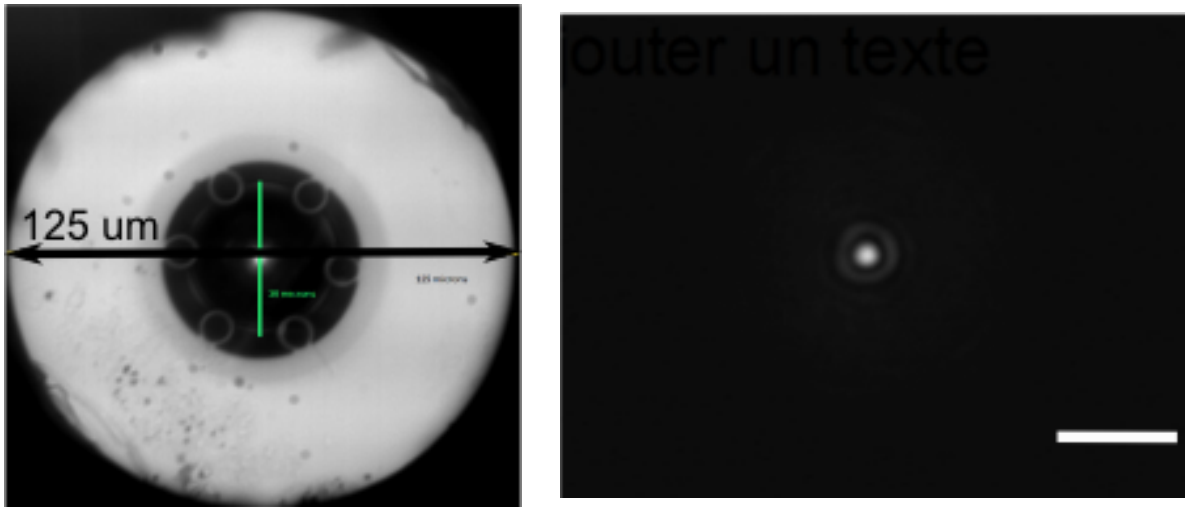

(a) **(b)**

Figure 5.2 Wide-field microscope image of the NCF and the focusing microsphere sealed in the NCF double-clad structure (a). A PSF formed by the sealed microsphere at 800 nm (b). Scale bar : 5 μm.

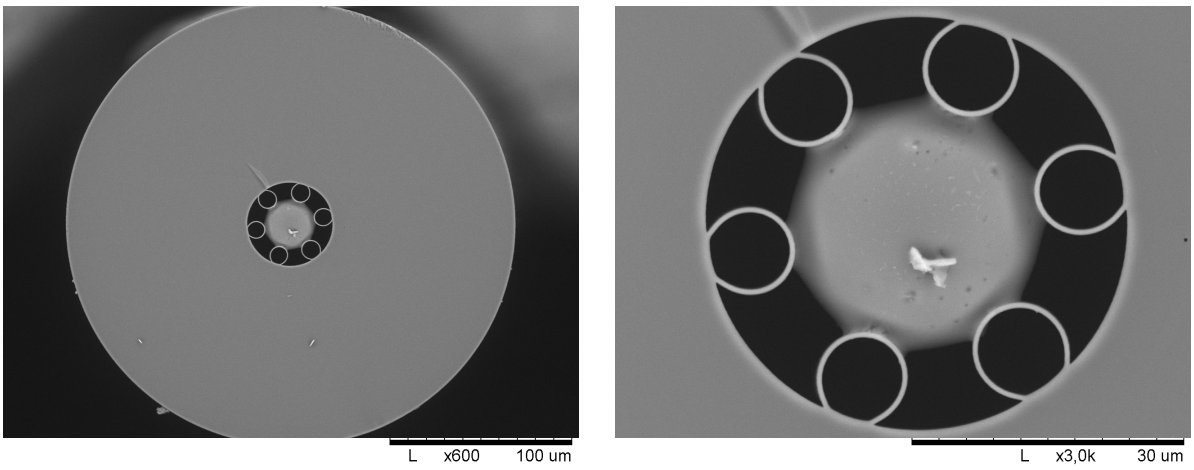

(a) **(b)**

Figure 5.3 SEM photographs of the NCF with the focusing microsphere attached by the CO_2 laser sealing (a) and zoom on it (b).

5.3 Portable miniaturized probe

The integration of a portable light-weight miniature probe was executed at XLIM institute (Limoges) in collaboration with Frederic Louradour and Marc Fabert. Marc Fabert conceived its final design and developed a detailed protocol for the integration procedure. With him we performed the manual assembly of the probe.

Assembling protocol The probe integration procedure requires high concentration and care, because of the irreversible nature of many steps. First of all, the NCF fiber to be integrated in the endoscope probe, comes already with a sealed focusing microsphere on the fiber front facet. It results that the fiber end cannot be re-cleaved in case of unwanted damage.

The assembling procedure starts by checking if the fiber passes well through two concentric ceramique holders which are meant to keep the fiber threaded in the center of the piezotube (Fig.5.4). The DC-NCF with a protecting polymer layer on top has a diameter of 450 microns. It passes through the back-support ceramique holder with 550 μm hole. We strip the polymer shell over 11 mm at the distal end of the fiber. The stripped fiber tip of 250 μm should pass through the front holder and remain centered in the piezotube.

In the meantime, we soldered four slim electric cables to the piezotube's electrodes. The electrode terminals have to be clean and flat, to fit the final enclosing metal tube and to avoid crosstalk among the electrodes. We also glued the mini-objective in a removable objective part. The metal tube of this mini-objective has been designed in such a way that only the very distal lens is glued. The rear most lens is held on a little nib made in the mini-objective metal tube. To assemble it, we just stack the second and third lenses on it, finishing by the fourth (last one)

which is glued to the metal tube with a UV glue.

Next, we glue the big back-support ceramique holder to the piezotube. The four electric cables should be straight, dipped into pre-designed little canals on the holder surface. It is critical to maintain the back-support and the piezotube as straight as possible. Otherwise, this angle will be conveyed until the final result, and may degrade the performance of the probe.

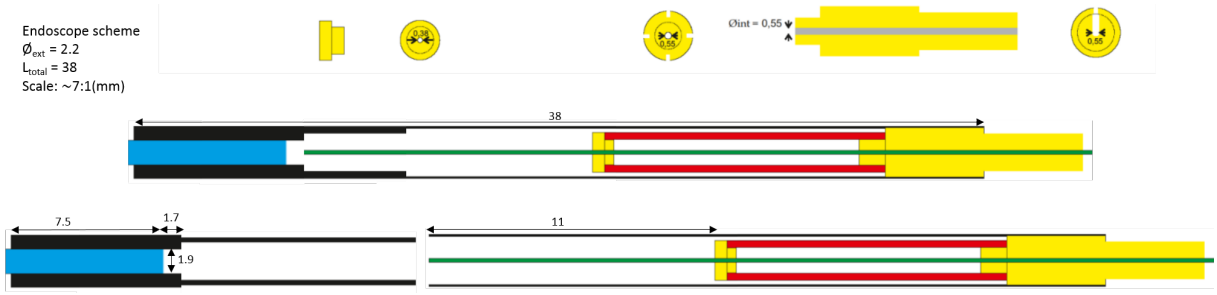

Figure 5.4 Integration scheme of the portable miniature probe. The distal outer diameter and the rigid length are: 2.2 mm and 38 mm respectively. The NCF scanning tip is 11 mm long.

The rigid length of the compact miniature probe (see Fig.5.5) doesn't exceed 40 mm with 2.2 mm distal outer diameter. This size factor is suitable for entry into conventional colonoscope and gastroscope working channels [112].

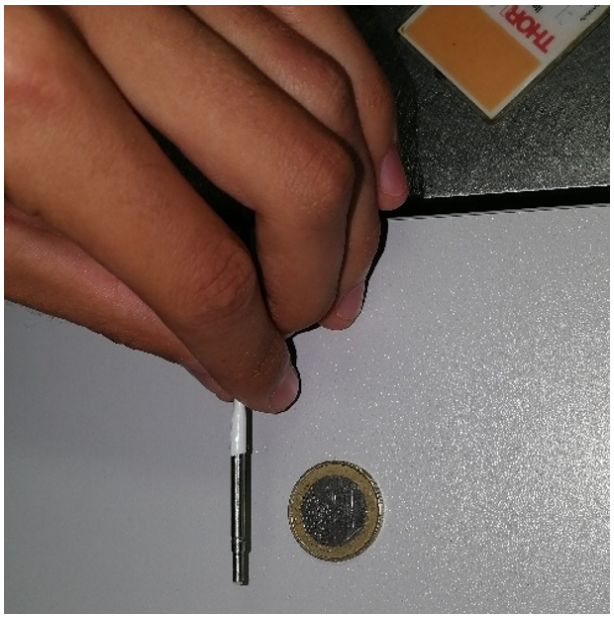

Figure 5.5 Integrated probe.

Assembly constraints The integrated probe described above results from several trials and corrections. We describe below the most crucial steps.

- **Soldering the electrodes**: It is important to make very smooth and flat solderings to avoid a crosstalk between the axes of the piezotube. Inadequate soldering will complicate individual axis control, leading to uncontrolled scan forms.
- **Concentricity of all the elements**: This is the most critical part of the probe assembling. Starting from the back-support ceramic holder, the fiber threaded into the piezotube and the mini-objective,– everything should be on the same axis. An example of the probe with an angle between the fiber with the focusing microsphere and the mini-objective is shown in Fig.5.6. We clearly see a line intead of a point on a CCD camera.
- **Voltage on the piezotube** : the piezotube described in Ch.4 can induce a displacement of the fiber tip of up to 1 mm at 75 V (peak-to-peak). With the mini-objective magnification of 0.63, it will make a $\sim$600 μm circular scan on the sample. However, the NI board generated 10 V can be amplified by the voltage amplifier (PI, Germany) by up to -100 and +250 V. If the driving voltages exceed $\pm$100 V, the fiber may touch the board of the metal sheath or, in the worst case, the focusing microsphere may be detouched from the fiber core.

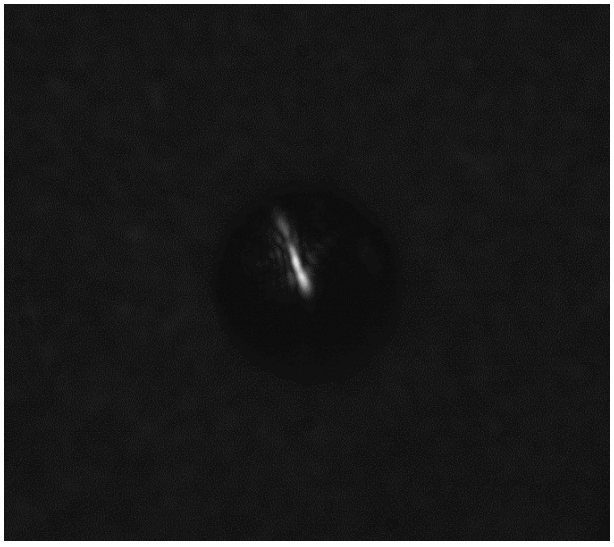

Figure 5.6 Example of an aberrated focal spot in case of an angle between the fiber and the mini-objective.

5.4 Integrated probe performance

In this section, we will show the results of basic imaging performance tests of the integrated probe. This includes imaging of the USAF-1951 transmission chart and CARS vibrational imaging of 5 μm polystyrene beads in forward and epi-detection.

Image of the focal spot Fig.5.7a) shows the focal spot of the pump beam (800 nm) on a CCD camera (Thorlabs), whereas the 1040nm focused spot is shown in Fig.5.7b). Both beam have a symmetric round shape geometry.

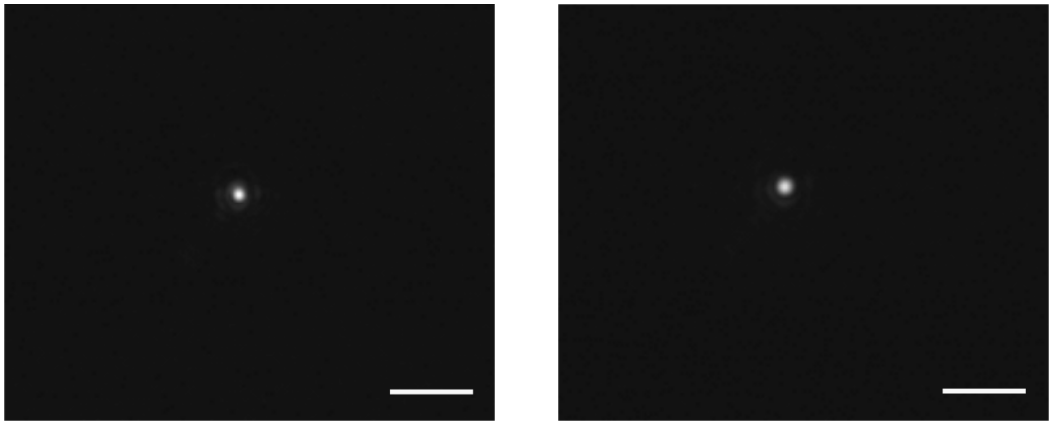

(a) **(b)**

Figure 5.7 Focal spot after the complete integration. Focal spot created by the integrated probe at 800 nm (a) and 1040 nm (b) of the laser beam propagated through the probe's NCF. Scale bar: 10 μm.

5.4.1 Imaging of calibrated samples

After having checked the focal spot quality, we can precisely measure the FOVs for different voltages applied to the piezotube. At the same time, it allows us to verify the scan conformity at different deflection amplitudes and different frame rates. We perform transmission imaging of a negative USAF-1951 chart. As can be seen in Fig.5.8, even at a speed of 8 frames/sec the scan remains stable and self-reproducible. We have selected the element 5 from the group 5. After the pixel-to-micron conversion, we find the FOV = $\sim$200 μm at 40 V (peak-to-peak) applied to the piezotube.

5.4.2 CARS imaging

We show here that the designed probe can perform 8 frames/sec CARS imaging. On a glass standard coverslip we deposited a solution of 5 μm polystyrene beads generating a very strong CARS signal at $\sim$2850 cm^{-1}. We still use the Coherent Discovery laser to provide the 800 nm and 1040 nm pump and Stokes beams. Fig.5.9a) shows a CARS transmission image of the beads with 12 mW total average power on sample with a neutral density filter before the detector (PMT). The epi-detected signal (Fig.5.9b) was excited with 8 mW of the pump (800 nm) and 4 mW of the Stokes (1040 nm) average power.

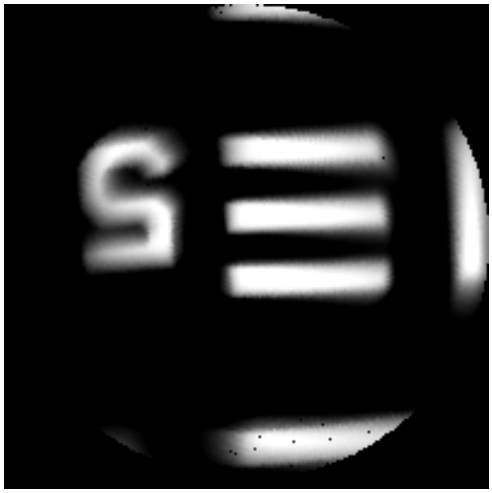

Figure 5.8 USAF-1951 negative transmission chart imaging (group 5, element 5).

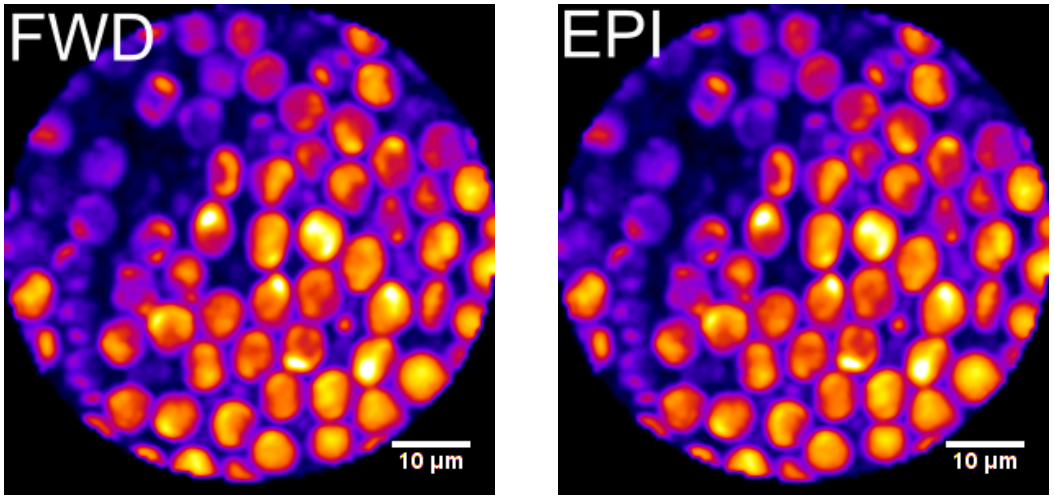

(a) **(b)**

Figure 5.9 CARS imaging of 5 μm polystyrene beads at 8 Hz speed acquired with the developed fiber endoscope probe. Total average power on the sample was 12 mW for both forward (FWD) (a) and epi-detected (b) CARS signals. However, a neutral density filter was placed in front of the detector (PMT, Hamamatsu), when FWD collecting.

Ex-vivo CARS imaging of mouse spinal cord A 1-mm thick and 2-mm long piece of mouse spinal cord was placed on a thick microscope glass plate (1 mm) and covered by a 100 micron coverslip. The sample was illuminated with 800 nm pump and 1040 nm Stokes beams. CARS images of myelin sheaths were obtained at 8 frames/sec scanning speed (Fig.5.10).

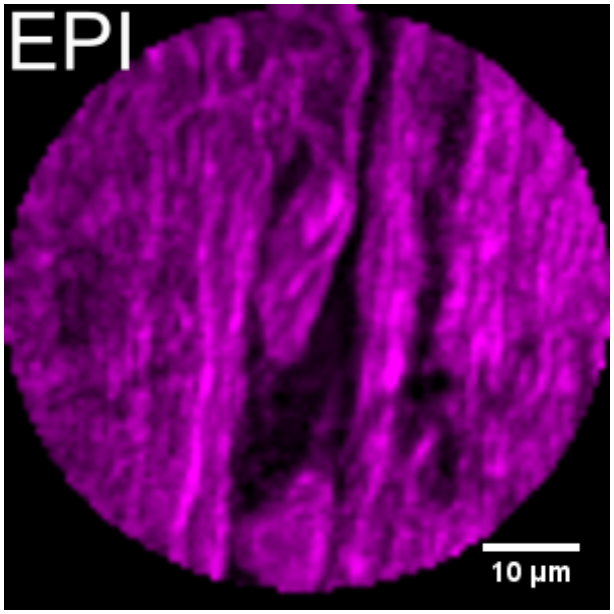

Figure 5.10 Spinal cord ex-vivo CARS image (epi-detection). Power: λ_{pump}=12 mW, λ_{Stokes}= 12 mW. Scanning speed: 8 frame/s. 10x averaged; 1.25 s total acquisition time.

5.5 Summary and conclusions

In this chapter, we have described the steps to integrate the portable probe. We have fulfilled the requirements for miniaturization and system robustness by introducing an improved probe design with a small (1.5 mm OD) piezotube and by sealing a focusing microsphere at the NCF fiber output facet. The final result is a 37 mm x 2.2 mm cylindrical probe performing high quality imaging with a resolution of 0.8 microns over a field of view of 250 μm at a maximum speed of 8 frames/s. We finally demonstrated that this probe can perform CARS imaging of 5-μm polystyrene beads and ex-vivo mouse spinal cord through the DC-NCF.

In the next chapter, we present the results of TPEF brain fluorescence imaging in an alive mouse with our miniaturized endoscope. We targeted the activity of GFP labelled neurons in mouse hippocampus.

Chapter 6

In-vivo deep imaging of GFP-labeled neurons

This chapter is dedicated to the application of the NCF endoscope for TPEF imaging of green fluorescent protein (GFP) labelled neurons in mouse hippocampus. We will describe the current challenges faced when recording the neuronal activity in live mice (Sec.6.1). Specifically for in-vivo imaging we will design and develop a vertically oriented translation platform enabling high precision lateral and axial displacement of the endoscope (Sec.6.2). The mouse preparation, skull surgery and maintenance during the imaging procedure is presented in Sec.6.3. We will discuss the results obtained after TPEF calcium imaging of an anaesthetized mouse (Sec.6.2.1).

6.1 Optical neuroimaging

In the beginning of 70es, O'Keefe and Dostrovsky studied the behaviour of a rat with hippocampal damage, which revealed the spatio-temporal mapping function of hippocampus [113]. Electro-physiology recording of the animal's reaction to its spatial orientation, has shown that depending on the direction of movement a specific group of neurons responsible for this orientation was activated. This brought the scientists to a conclusion that the mammalian brain is provided with the information about the environment surrounding by hippocampus neurons.

Recently, the advances in optical imaging combined with genetically encoded fluorescent markers have allowed to overcome the limits of electrophysiology [114]. TPEF microscopy [50] has enabled high resolution, intrinsic sectioning imaging of brain which have led to the discoveries of complex mechanisms occurring in mouse brain [115, 116]. The TPEF neuroimaging of the hippocampus has been performed in-vivo with the use of a cranial glass window with a removal of the upper cortical layers which can increase the imaging depth limited by light attenuation and scattering in brain tissue (Fig.6.1). The necessary alteration of the cortex structure has been circumvented when reducing the objective's effective NA [117]. By underfilling the

back-aperture of a high NA (1.0) objective, TPEF imaging of the hippocampal CA1 region has been performed.

It has been proposed to move the excitation wavelength towards 1300 nm and 1700 nm [118, 119]. This permitted to reduce tissue scattering and enabled three-photon excitation (3PE) using a new generation of calcium indicators [118, 120]. A recent study has reported an unprecedented depth (∼1 mm) by 3PE imaging in the hippocampus pyramidal layer of an intact mouse brain [121] (Fig.6.1). Furthermore, multi-color TPEF and 3PE neuroimaging [122] have allowed to benefit from the rapid development of genetically encoded calcium indicators [120]. The axial scanning has become accessible with the application of electrowetting lenses in a miniaturized TPEF microscope [123].

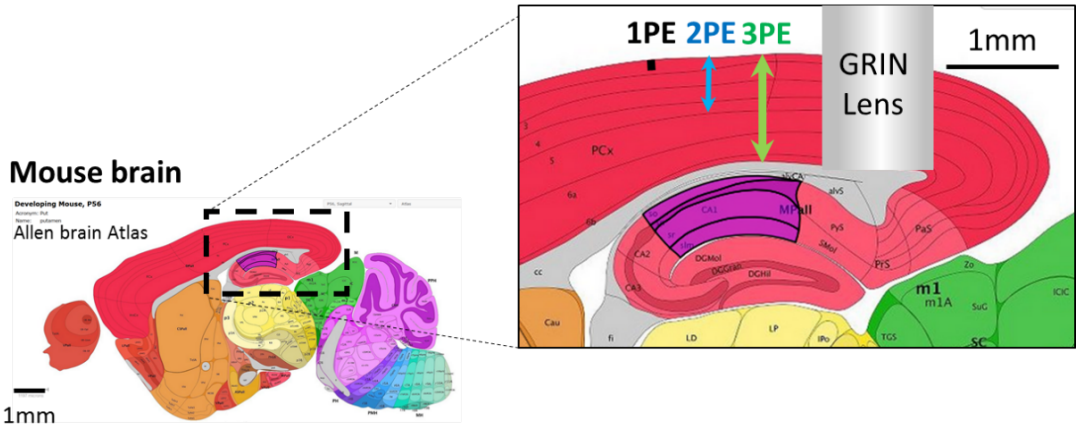

Figure 6.1 Imaging depth into the mouse brain using 1-photon (OPE – black), 2-photon (TPEF – blue) and 3-photon (3PE – green) fluorescence. A GRIN lens (1 mm) illustrated in the same graph is typically used for deep brain imaging (the GRIN lens can be inserted at any depth).

In spite of these advances, brain imaging becomes impossible when going deeper than the photon transport (TMFP) mean free path [124]. At such depths the incident photons cannot preserve the information about their initial direction heavily complicating energy conservation and focusing [125]. For the purpose, to increase the imaging depth, gradient index GRIN lenses have been used [126–130]. Their outer diameter varies from 500 μm until 2 mm (Fig.6.1 and Fig.6.2). These lenses are used in combination with long-working distance microscope objectives, relaying the focal spot deep into the brain. So far, most of in-vivo hippocampus imaging has been done with relay GRIN lenses [127, 130]. Higher depths are also achievable, shown in lateral hypothalamus [131] and arcuate nucleus [132]. Nowadays, the hippocampus function has been investigated in head-restrained (Fig.6.2a,b) and freely moving (Fig.6.2c,d) mice [131, 133] mostly with the GRIN lenses based miniaturized OPE fluorescence microscope [129, 134]. This device dedicated to neuronal activity imaging in behaving mice was commercialized (Inscopix, US) (Fig.6.2 d). The major part of TPEF advances have been combined in a miniaturized microscope based on Micro-Electro-Mechanical Systems (MEMS)

mirrors [135]. The authors have demonstrated high resolution (0.64 μm spatial and 3.35 μm axial) and frame rate (40 frames/s) in-vivo cortex imaging of a freely behaving mouse.

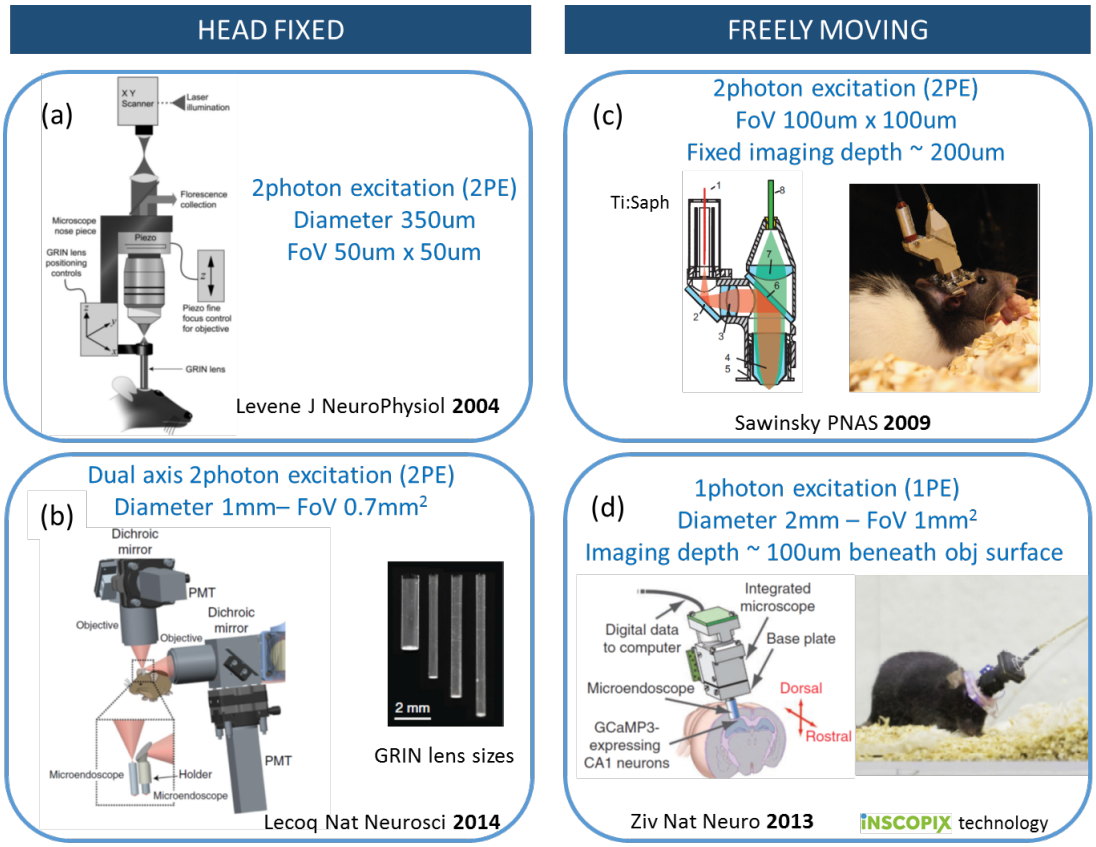

Figure 6.2 Common solutions employing GRIN lenses for in-vivo brain imaging. Head-fixed geometry (a,b) [127, 136], miniaturized microscopes for freely moving experiments (c,d) [130, 137]. OPE and TPE have been demonstrated (d), only OPE: (a, b, c). A commercialized OPE (Inscopix Inc.) head-mounted miniaturized microscope often used in neuroscience (d). Inset in b shows GRIN lenses diameters.

The described above solutions have pushed the *in-vivo* visualization of mouse brain activity. However, they still lack many important features inaccessible for these complicated setups working in OPE regime.

- The first complication comes from the difference of the mouse behaviour in restrained head experiments (Fig.6.2 a,b). The place cells activity alteration was reported in a head-fixed mouse as compared to the case when the animal was freely moving being able to express socially activity, signs of anxiety or fear [138, 139].
- Second, OPE deep brain imaging lacks optical sectioning which in combination with background fluorescence limits the investigation of the activity in densely populated brain layers. This drawback can be suppressed using TPE, however the latter requires a bench top setup and head fixation (Fig.6.2 b), with a single exception reported on a head-fixed miniaturized microscope limited by a fixed penetration depth (Fig.6.2 c) [137]. With reduced photo-toxicity

and photo-bleaching TPEF approach remains much more advantageous for *in-vivo* calcium flow dynamics in axons and spines.

- Most of the described above imaging solutions rely on Micro-Electro-Mechanical Systems (MEMS) mirrors for sample scanning. Despite the MEMS's capability to scan fast over the sample area (>60 Hz), these systems remain very complicated to fabricate. The complex architecture, fragility and high cost handicap their application in miniaturized probes. Inversely, piezotube based endoscopes perform equally good, at the same time being very robust, simple and cost-effective [140].

6.2 NCF endoscope for TPEF imaging of GFP-labelled neurons

In this section we will address some of the challenges related to neuroimaging. We will use the scanning tip endoscope developed during this PhD thesis for the application in mouse hippocampus TPEF imaging of calcium indicators (GCaMP6). These are commonly used GFP-based Ca^{2+} probes which can be genetically encoded [141].

6.2.1 Ex-vivo imaging of mouse brain

Mouse brain slices will be tested for the endoscope capability to efficiently excite and collect a TPEF signal coming from GFP-labelled neurons. The ex-vivo experiments on brain slices are done in the setup presented in Ch.2 (Fig.2.2). The samples were prepared at Institut de neurobiologie de la méditeranée (INMED). The GFP viral infection and the mice treatment will be discussed more in Sec.6.3. Herein, we will compare the collection by the NCF and Kagomé fiber based probes of the signal emitted by neurons.

Samples preparation After extraction, the brain is immersed in a solution of ACSF (an artificial cerebrospinal fluid) composed in mM of: 126 $NaCl$, 3.5 KCl, 1.2 NaH_2PO_4, 26 $NaHCO_3$, 1.3 $MgCl_2$, 2.0 $CaCl_2$ and 10 D - glucose, pH 7.4 which allows to conserve the brain. Then it is glued onto the platform of a vibratum, a device which allows to accurately dissect tissue with a blade. Thus, it is possible to obtain very thin slices (<100 μm) with a very smooth surface. The thin slices are kept in the solution which is described above. In order to use the brain slices for TPEF endoscopic imaging, they are sandwiched between microscope thick glass plate (~ 1 mm) and thin coverslip (100 μm) with an adhesive spacer.

Imaging through Kagomé fiber Mouse brain slices were first imaged through the Kagomé fiber endoscope. The signal was collected in reflection by the Kagomé fiber double clad and also in transmission through a microscope objective (0.6 NA, 60x).

The samples were excited with 100 fs pulses at 920 nm with a low average power on sample (30 mW). In the transmission mode, a strong TPEF signal coming from GFP-stained neurons was collected (Fig.6.3a). At the same time, the emitted signal collected and delivered by the Kagomé

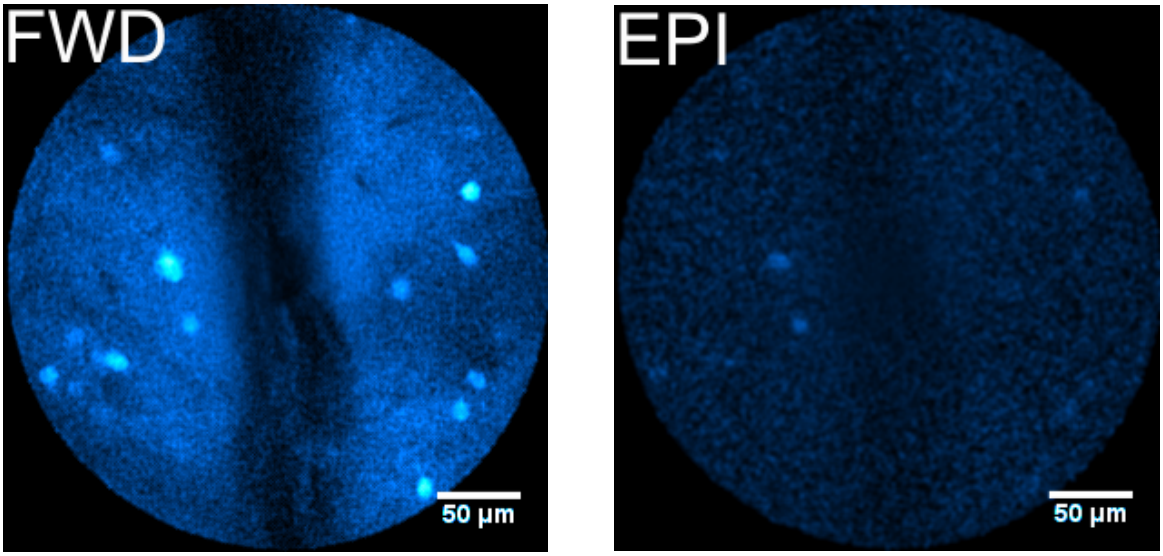

(a) (b)

Figure 6.3 Kagomé fiber endoscope brain slices TPEF imaging. An image of GFP labeled neurons collected by a microscope objective in the transmission mode (a). Power: P=30mW (λ=920 nm). The same sample area excited with P=80 mW (λ=920 nm), the epi-collected signal (b). The images were 10 times averaged. Scanning speed: 0.8 frame/sec. Filters: bandpass (550/100 nm), shortpass ($\lambda_{cut-off}$ =760 nm)

fiber was very weak due to the fiber core losses at the emission wavelength (520 mn). Only few the most bright neuron cells can be observed in the epi-detection (Fig.6.3b).

Imaging through NCF In contrary to the Kagomé fiber case, the DC-NCF (increased double-clad with the lossy fiber core, Fig.3.9a) collected signal is much stronger. A mouse brain slice of 100 μm excited with 920 nm is shown in Fig.6.4a). Many neurons spread over a FOV of >300 microns can be seen with a high contrast. In a zoomed image individual axons stemming from the neuron body can be observed (Fig.6.4b).

In Fig.6.5, we show a 100 μm depth stack of TPEF images. All the white spots represent individual neuron cells. The dark spots appear at the location of neurons which do not generate any light, being non-labelled or bleached.

6.2.2 A new DC-NCF with the core improved signal collection

The DC-NCF fiber integrated into a portable probe (Ch.5) can transmit the excitation light through the hollow fiber core in a broad spectral range (700-1050 nm). However, the emission

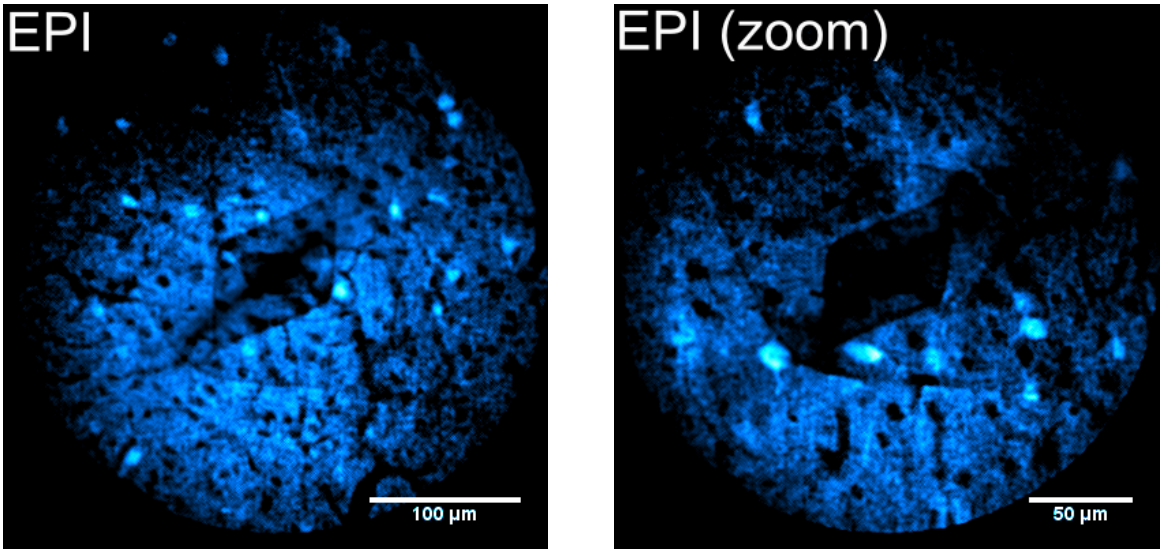

(a) **(b)**

Figure 6.4 Brain slices TPEF, imaged with the NCF endoscope (a), the same area zoomed (b). Power: P=80mW (λ=920 nm). The images 10 times averaged. Scanning speed: 0.8 frame/sec. Filters: bpass (550/100 nm), shortpass ($\lambda_{cut-off}$ =760 nm)

signal coming from GFP-labelled neurons (λ_{peak}=520 nm) will experience high propagation losses, if it is captured by the NCF fiber core (Fig.3.9a). This is a critical point, as the expected signal collected over a large FOV (<200 μm) at 8 frame/sec rate will be weaker as compared to the case of lower imaging rates (1 frame/sec). The high scanning speed with the scan spread over a big area leads to minuscule pixel dwell times (<2 μs), resulting in a very low SNR in an individual imaging frame.

Due to a less complicated NCF design (Fig.3.1a) as compared to the Kagomé fiber (Fig.2.5a), the NCF fiber core transmission can be re-designed to a desirable spectral range [142]. Together with our colleagues at IRCICA Lille we have redesign a new NCF optimized for neuroimaging. This fiber has been already presented in Fig.3.9b). It features a core that transmits both the excitation 100 fs pulse at 920 nm and collects the generated 450-600 nm light from fluorophores (Fig.6.6). On the top of that this new fiber design includes a double clad (DC) for improved back collection efficiency. All together this new DC-NCF performs better than previously fabricated fiber for GFP tagged neurones.

The difference between the new NCF probe with the one described in Ch.5 is that the scanner and the mini-objective have not been yet encapsulated in a metallic tube. In this free-space configuration the mini-objective and the piezotube (Fig.6.7) will be held separately in a vertical position to allow for the mouse positioning.

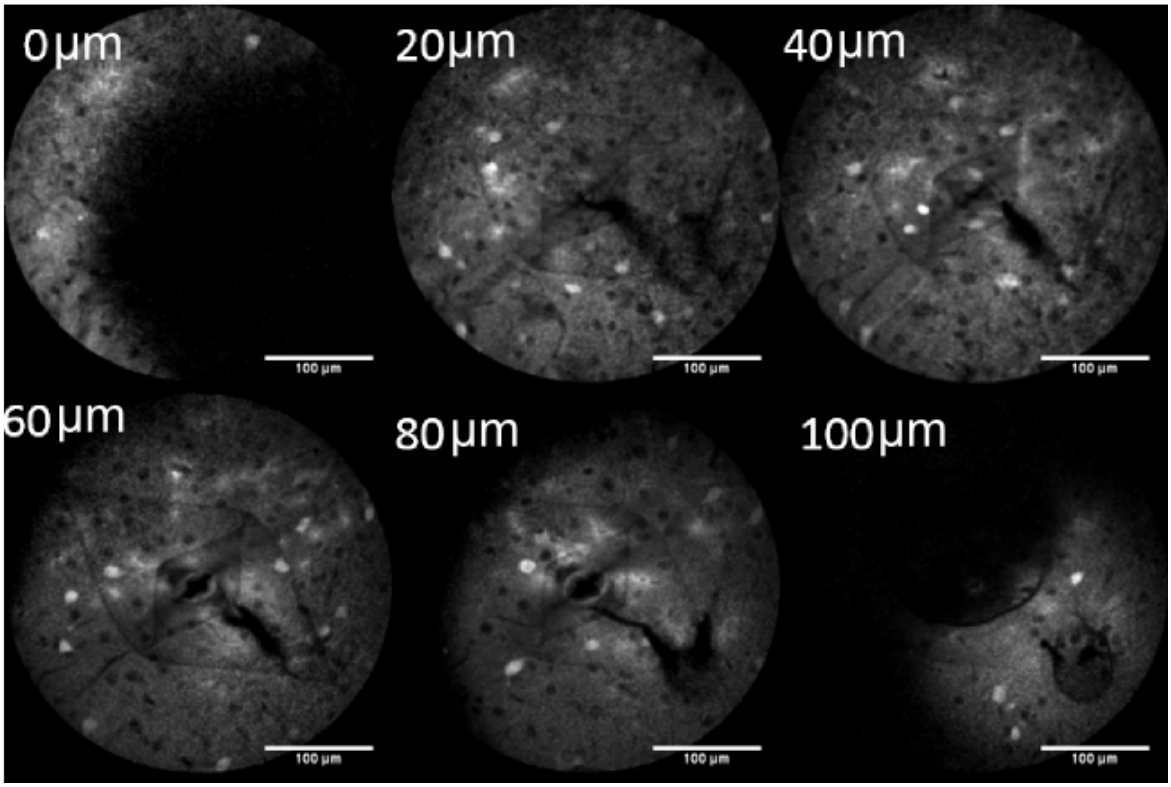

Figure 6.5 Ex-vivo GFP labelled neurons from mouse hippocampus. 100-μm depth TPEF images taken with the NCF endoscope. Excitation: P=80 mW sample (λ=920 nm). Every image was 10 times averaged. Scanning speed: 0.8 frame/sec. Filters: bandpass (550/100 nm), shortpass ($\lambda_{cut-off}$ =760 nm).

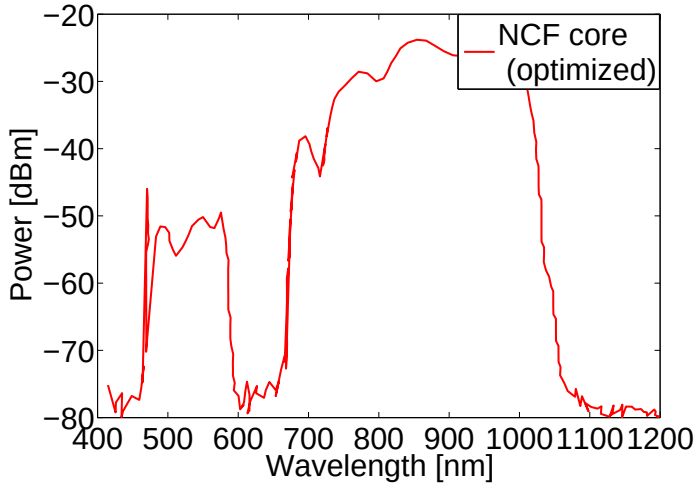

Figure 6.6 The NCF fiber core transmission. The fiber core characterized by two spectral bands: 480-580 nm and 700-1000 nm, can efficiently deliver the TPE (GFP) beam and back-collect the emitted signal.

Figure 6.7 A new open-space configuration scanner based on the improved NCF.

6.2.3 3D positioning

A free access graphic software (FreeCad) was used to design a vertically oriented platform for the NCF endoscope. This platform is intended to support a living mouse for in vivo brain activity measurements. 3D sketches of all opto-mechanical components from Thorlabs, for instance, can be easily downloaded from the corresponding site. The vertically oriented setup (Fig.6.8) consists of a 1.5 inch pedestal post with a post mounting clamp and a breadboard fixed on it (Thorlabs). With a micro-positioner (MAX313D, Thorlabs) translation stage fixed on the breadboard, the NCF endoscope can be 3D translated on the sample during imaging. A lab jack translation mount (L490/M, Thorlabs) located below the endoscope is used for the mouse placement and coarse positioning.

6.2.4 Bimodal imaging

With the optimized NCF endoscope TPEF imaging of GFP-labelled neurons can be performed over a 300 microns FOV. An additional display control is needed to coarsely guide the endoscope onto the desirable location. The mouse has a cranial window with a metallic cannula in its skull through which the hippocampus can be imaged. Thus, to facilitate the probe insertion into the imaging cannula on the mouse head, a high-frame digital microscope (AM73915MZT, Dino-lite) was used (Fig.6.9). With its tunable magnification ranging from x10 until x220 and very long working distances WD: 60-12 mm correspondingly, the digital microscope helps to guide the probe in a well-controlled manner (Fig.6.10 and Fig.6.11).

The bimodal combination of the digital microscope with the NCF endoscope (Fig.6.11) enables a rapid imaging position adjustment, needed for the observation of different layers and

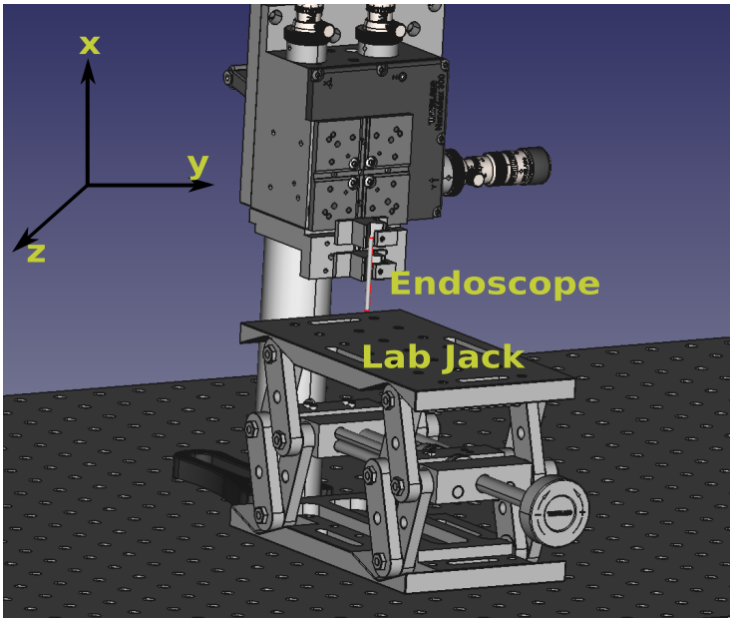

Figure 6.8 Illustration of the vertical platform for the NCF probe and a lab jack translation mount (L490/M, Thorlabs). The lab jack is intended to support a living mouse for brain activity imaging.

Figure 6.9 Digital microscope (AM73915MZT, Dino-lite) (a), Dinolite macro-positioning holder (b). Images taken from [www.dino-lite.eu].

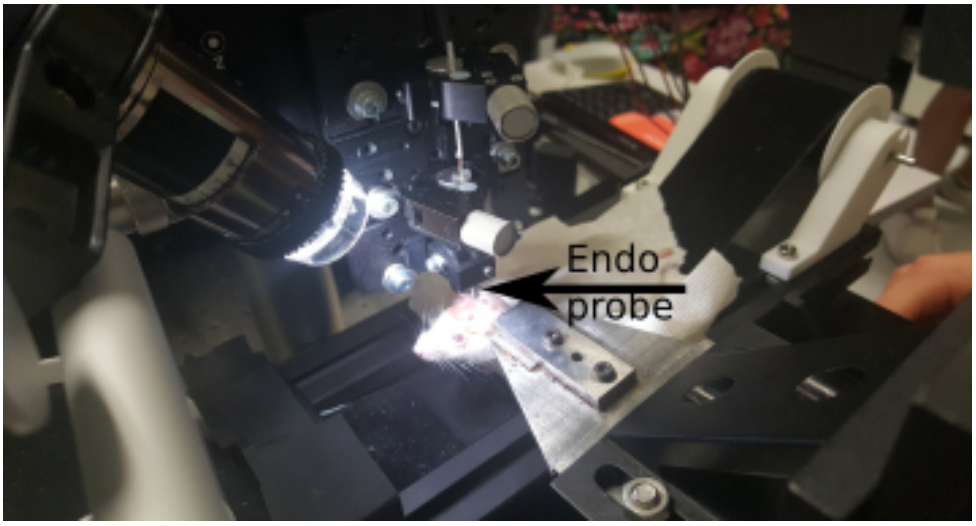

Figure 6.10 The bimodal imaging setup consisting of the digital microscope and the endoscope.

areas of mouse hippo-campus.

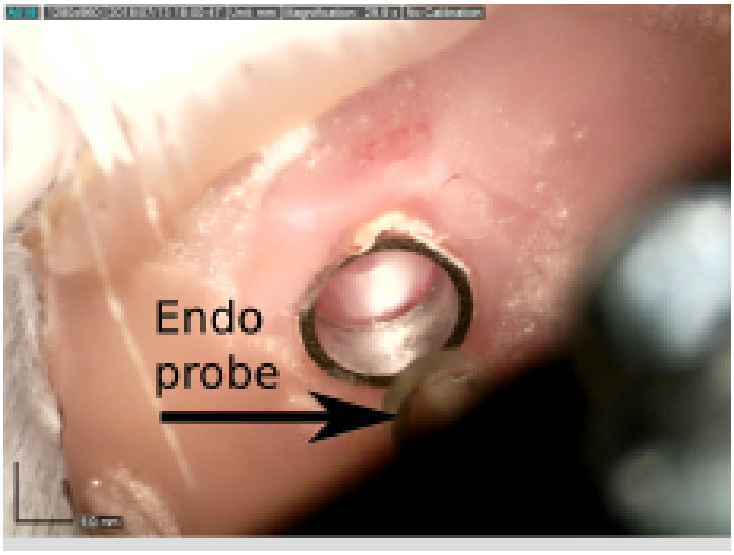

Figure 6.11 An image of the endoscope and the metal cannula attached to the mouse skull. The photo is taken with the digital microscope during the insertion of the endoscope.

6.2.5 Scan calibration

For the correct image reconstruction the endoscope calibration has to be routinely performed every day (Sec.4.2). Thus, while developing a vertical imaging setup, to facilitate the calibration procedure, a little add-on removable unit for the probe calibration has been designed in FreeCad (Fig.6.12). The laser beam collected by a microscope objective (60x, 0.6 NA) was further trans-

lated by a 90 degrees mirror (Thorlabs) and focused with a tube lens (150 mm, Thorlabs) onto the position sensitive detector (PSD). The whole platform with the post holding the objective and the mirror with the lens, as well as the PSD can be easily removed after the calibration is finished.

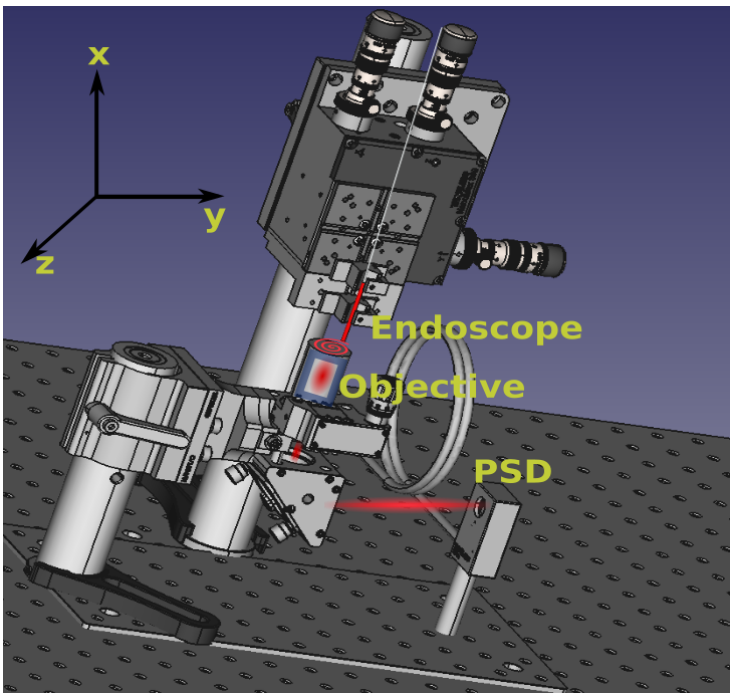

Figure 6.12 Vertically positioned endoscope probe at the calibration stage. The fiber position is measured by the PSD.

6.3 Mouse preparation for imaging

The mice follow a long process of viral infection, skull surgery and training before the imaging procedure. For this, a precise protocol has been developed by Vilette *et al.* inspired from Dombeck *et al.* [103, 116]. Two months after the birth, the mouse is viral injected. The virus carries the fluorophore to the neural cells composing the pyramidal layer of the hippocampus. After one week of incubation, a skull surgery is performed. The mouse is trained to sustain the stress induced by the imaging process.

Mouse surgery The surgery is performed to implement a cranial window above the hippocampus allowing for in-vivo imaging of the latter. During the surgery procedure, a part of the mouse skull is removed together with a thin cortical layer (Fig.6.13, [143]). After the application of an agarose gel, a window composed of a metallic cylinder with a glass coverslip in it, is placed

and fixed on the skull with a dental cement (Fig.6.11). With this window, an observation of different layers of the hippocampus can be performed (Fig.6.11).

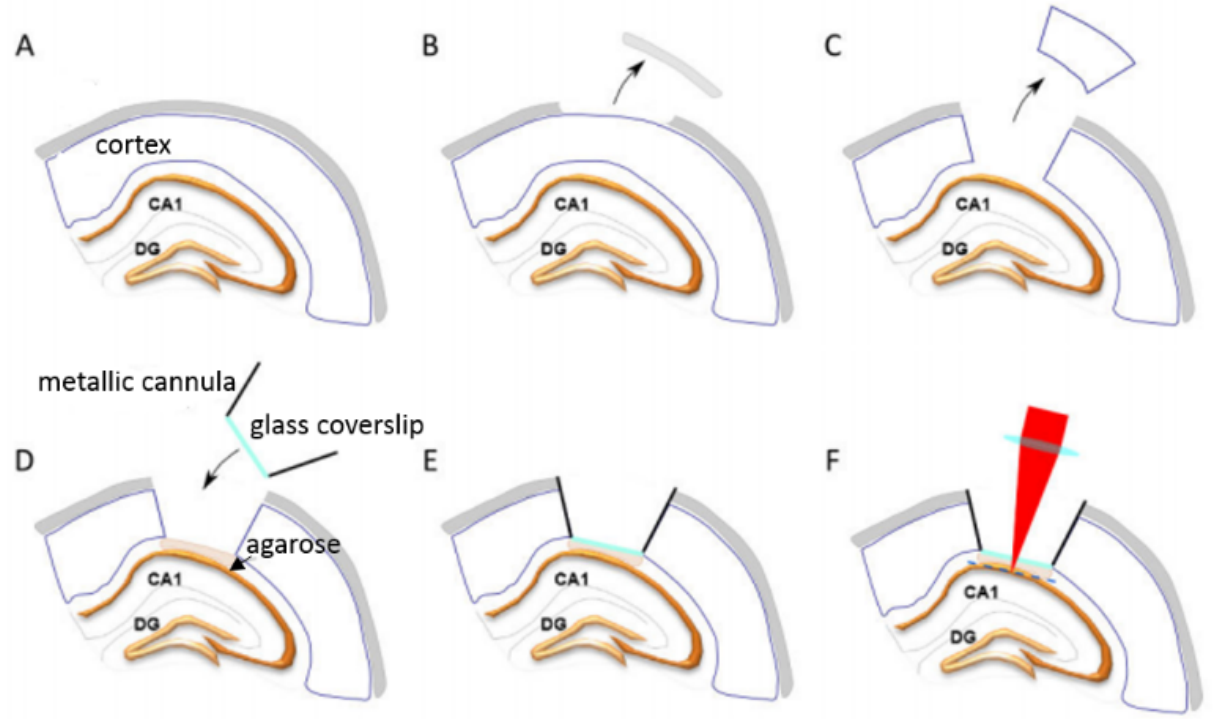

Figure 6.13 Schematic representation of different stages of the mouse cranial surgery. Hippocampus is located at 1 mm depth under the skull surface. A piece of the skull is removed (B) followed by the removal of a 1-mm^3 volume of the cerebral cortex (C). The created space is filled with an agarose gel and covered with a glass coverslip embedded in a metallic cannula. The mouse can withstand the imaging procedure after some training (F) [143].

6.4 In-vivo TPEF imaging of calcium indicators

A recent study of CA1 region in mouse hippocampus has been performed with a TPEF microscope through a cranial window [103, 116]. The researchers showed that the cortex layer removal does not affect the properties of hippocampus function. Dombeck *et. al* have studied the neuronal circuit dynamics during behaviour of a mouse with head-restrained. This method allowed to observe simultaneously a large group of CA1 neurons in transgenic mice. The experiments showed the correlation between the physical location of neurons and their virtual spatial zones of responsibility. The findings of Vilette *et. al* about recurring hippocampal sequences demonstrated the importance of the hippocampus for the spatiotemporal cognition.

Genetically encoded calcium indicators (GECIs) expressing GCaMP facilitate long-term in-vivo imaging of neurons [144]. Different modifications of GCaMP indicators have improved the range of fluorescence signal [145, 146].

In this section, we will apply the NCF endoscope for TPEF GCaMP6 imaging of mouse hippocampus neurons. The anaesthetized mouse was placed on the lab jack and the NCF endoscope was inserted in the metallic cannula (Fig.6.10 and Fig.6.11). In the beginning, a 920 nm excitation beam was used with moderate average powers (50 mW). However, this power had to be doubled to provide a good TPEF signal at high depths where hippocampal neurons are located (Fig.6.13). Different imaging depths were inspected, in order to find an area with a group of neurons. We found a layer with three very bright neuron cells (Fig.6.14 a). Three series of acquisition (10 minutes duration) were performed over the selected area at 8 frame/sec imaging speed. A projection mask was applied on the location of the neurons permitting to measure the signal intensity in the area of a neuron for every 125 millisecond (Fig.6.14 b). A stack of raw 4300 images was recorded and analysed (Fig.6.15). However, we tend to think that this was not an activity event produced by hippocampal neurons. In anaesthetized mice the CA1 activity is much weaker as compared to the behaviour state [147–149]. The next step in this experiment will be to integrate the developed TPEF fast scanner into a stainless metal tube as we did in Ch.2 and perform the same imaging procedure in an awake mouse. For this purpose, a higher output power might be needed for an efficient excitation of deep hippocampal layers and a fast power control to dim the beam during the piezo braking time.

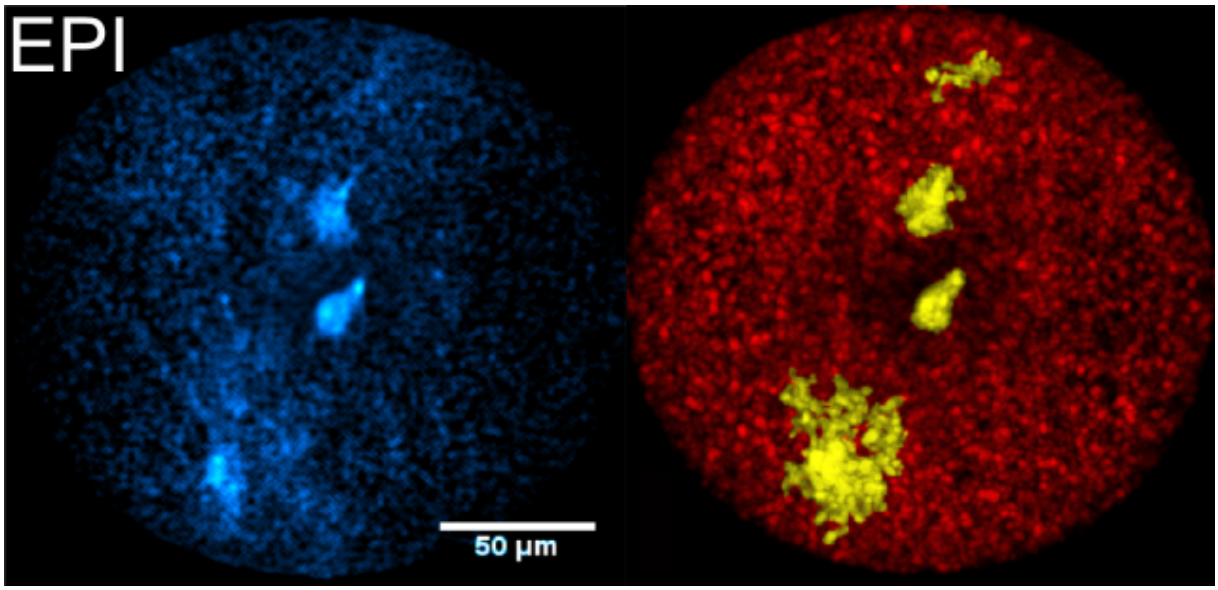

Figure 6.14 An area with three bright neurons. TPEF image taken (50x averaged) with the NCF endoscope (a). A projection mask used to separate the location of the neurons and measure the signal intensity only within the masked area (b). Excitation: 920 nm (100 mW average power). Filters: shortpass (700 nm cut-off), bandpass (520/40 nm). Imaging speed: 8 frame/sec.

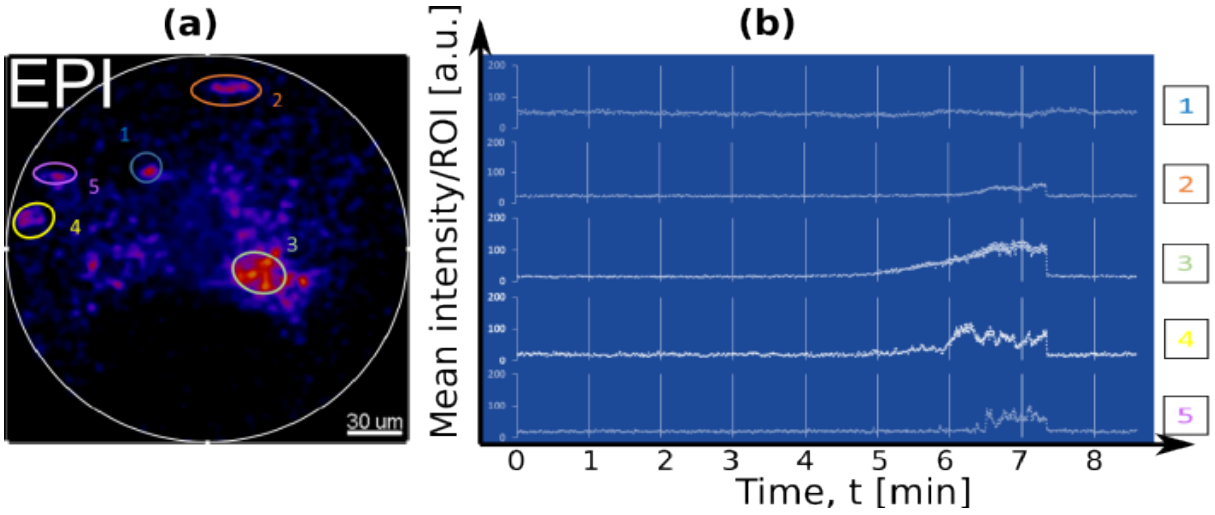

Figure 6.15 An area with five bright neurons. TPEF signal acquired with the NCF endoscope with 8 frame/sec rate (raw images) (a). Time traces from a region of interest (ROI) selected out of 4300 image frames (b). Power=120 mW.

6.5 Conclusions

We have successfully performed in-vivo mouse hippocampus TPEF imaging of calcium indicators expresses by transgenic mice. In this work by means of the NCF-based endoscope with an optimized fiber, we provided a reliable imaging device, which enables high resolution and speed inspection of mouse intact brain. The NCF-endoscope allows for large FOV, high contrast imaging of GFP-labelled neurons deep in mouse hippocampus. Our simple piezotube technology offers a high stability performance and minimizes the potential cost of such systems. Those qualities will permit to replace bulky bench-top and miniaturized TPEF microscopes by a single-fiber portable probe of 2.2 mm of the outer diameter and <30 mm rigid length.

6.6 Future perspectives

We have developed a miniature, scanning tip endoscope for CARS, SHG and TPEF multimodal imaging of unstained tissues over large FOVs. An active motion braking was developed that enabled to increase the imaging speed up to 8 frames/sec. This endoscope is based on a novel DC-NCF, whose effective DC area in combination with the improved fiber core transmission have significantly increased the contrast of every raw imaging frame (125 ms) as compared to our previously designed endoscope based on a Kagomé HC DC fiber. This collection efficiency improvement together with the reduction of the distal endoscope diameter down to 2 mm allowed to perform *in-vivo* imaging in a mouse hippocampus. We demonstrated the capability of the developed probe to record neural activity in CA1 with high spatial and temporal resolution.

The availability of a reliable, miniature size, portable and robust TPEF endoscope will significantly simplify deep-brain neuroimaging. The broad spectral transmission range of the NCF hollow-core can also be used to excite multiple endogenous markers, such as green and red fluorescent proteins, thus permitting dual-colour brain imaging. Moreover, CARS, SHG and THG can be used as additional valuable contrasts for label-free imaging in mouse brain. We would like to describe possible improvements related to neuroimaging:

- **Modified design** TPEF imaging of hippocampal neurons can be performed with the NCF endoscope in freely behaving mice. This, however, will require a stable fixation of the miniaturized probe on mouse skull. A modified design of the endoscope probe (Fig.6.16 b) can be particularly suitable for freely moving brain imaging experiments. The mini-objective lens can be oriented with 90 degrees angle to the scanning fiber, and the beam could be reflected from the fiber end onto the mini-objective with a miniature mirror. The animal would have the endoscope fixed on the head but also on its back such that this probe would be less cumbersome to carry.

- **Scanning speed, power control and medical compatibility** The mouse movement and the need of rapid recording of the intensity change from calcium indicators requires high speeds scanning. For this purpose, the achieved 8 frames/sec speed can be further increased. It is possible to obtain higher frame rate by decreasing the imaging period and the braking time. Besides, a precise power control during the piezo braking time (10 ms) will reduce photobleaching and provide a more accurate data when monitoring the small intensity variations from an individual neuron cell.

The possibility to perform high speed and resolution CARS, SHG and TPEF (intrinsic) endoscopy opens the door for in-vivo imaging of the digestive system. However, the application of the developed NCF endoscope by practitioners and biologists will require a friendly-user control software and a simple calibration procedure. The current endoscope by itself can enter into the user port of gastric endoscopes whose diameter is around 3 mm however special care should be taken to ensure that the high voltage used in the piezo is compatible with human in vivo

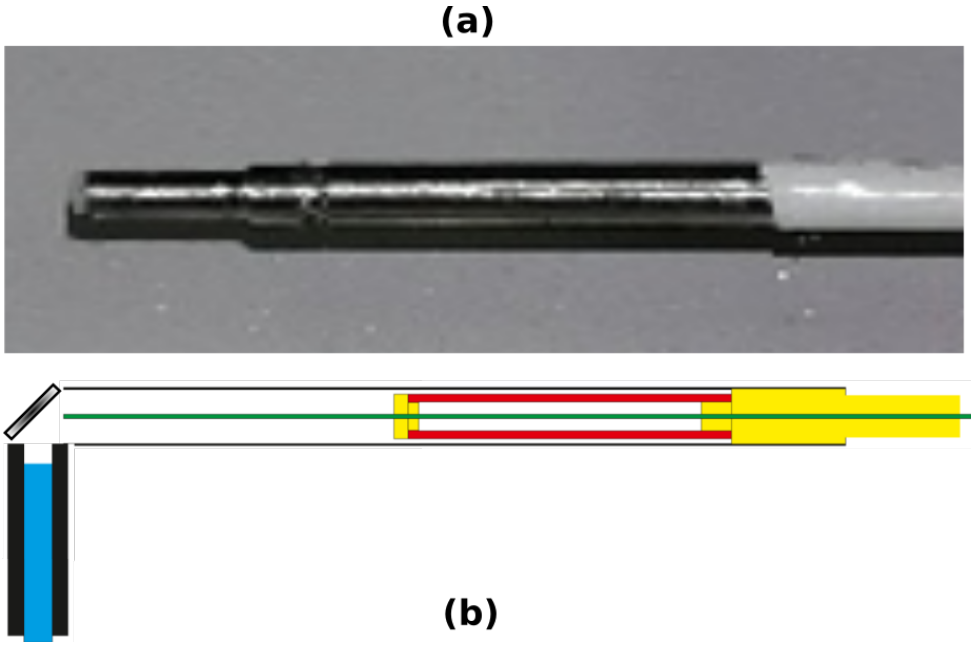

Figure 6.16 Miniaturized endoscope probe. Current design of the probe (a) and flipped-tip modified endoscope for freely-moving imaging (b).

imaging. There is also the issue of being able to decontaminate the endoscope and future work has to address the possibility to enter the full endoscope into an autoclave.

- **Automatization of the calibration procedure** The piezotube based scanning-tip endoscope has to be calibrated in a day-to-day routine. The parameters for a symmetric scan and efficient braking are usually retrieved iteratively, which requires 1-hour of time for an experienced user. Thus, an algorithm for an automatic search and calibration of the endoscope probe will be necessary for practical use. The first attempt to develop such an automatic calibration procedure has been carried out during this PhD work. We have implemented a program loop which can iteratively sweep the values of the scanning parameters and find the ones fitting the demanded specifications. This work has to be continued, including the control of the braking parameters.

There is much to expect from the future development of such endoscope, its relatively simple design and robust piezo based technology is expected to be an advantage over more complicated scanning schemes using micro electro-mechanical systems. The implementation of hollow core fibers allows for a variety of illumination scheme ranging from CW to advanced pulsed schemes. All together the designed and fabricated probe is expected to find applications in various fields such as material science, biology, pharmacology and biomedical optics.

Bibliography

[1] N.S. Claxton. *Laser Scanning Confocal Microscopy. Encyclopedia of Medical Devices and Instrumentation.* 6 edition, 2006.

[2] W. Denk, JH. Strickler, WW. Webb. Two-photon laser scanning fluorescence microscopy | Science. http://science.sciencemag.org/content/248/4951/73, 1990.

[3] Rafael Yuste. Fluorescence microscopy today. *Nature Methods*, 2(12):902–904, December 2005.

[4] Andrew Folick, Wei Min, and Meng C. Wang. Label-free imaging of lipid dynamics using Coherent Anti-stokes Raman Scattering (CARS) and Stimulated Raman Scattering (SRS) microscopy. *Current Opinion in Genetics & Development*, 21(5):585–590, October 2011.

[5] Wei Min, Christian W. Freudiger, Sijia Lu, and X. Sunney Xie. Coherent Nonlinear Optical Imaging: Beyond Fluorescence Microscopy. *Annual review of physical chemistry*, 62:507–530, 2011.

[6] Christian W. Freudiger, Wei Min, Brian G. Saar, Sijia Lu, Gary R. Holtom, Chengwei He, Jason C. Tsai, Jing X. Kang, and X. Sunney Xie. Label-free biomedical imaging with high sensitivity by stimulated Raman scattering microscopy. *Science (New York, N.Y.)*, 322(5909):1857–1861, December 2008.

[7] Andreas Volkmer. Vibrational imaging and microspectroscopies based on coherent anti-Stokes Raman scattering microscopy. *Journal of Physics D: Applied Physics*, 38(5):R59, 2005.

[8] P. A. Franken, A. E. Hill, C. W. Peters, and G. Weinreich. Generation of Optical Harmonics. *Physical Review Letters*, 7(4):118–119, August 1961.

[9] William Mohler, Andrew C. Millard, and Paul J. Campagnola. Second harmonic generation imaging of endogenous structural proteins. *Methods (San Diego, Calif.)*, 29(1):97–109, January 2003.

[10] D. Yelin and Y. Silberberg. Laser scanning third-harmonic-generation microscopy in biology. *Optics Express*, 5(8):169–175, October 1999.

[11] Boyd, R. "*The Nonlinear Optical Susceptibility*". *Nonlinear Optics (Third Edition)*. 2007.

[12] Maria Göppert-Mayer. über Elementarakte mit zwei Quantensprüngen. https://onlinelibrary.wiley.com/doi/full/10.1002/andp.19314010303, 1931.

[13] Warren R. Zipfel, Rebecca M. Williams, and Watt W. Webb. Nonlinear magic: Multiphoton microscopy in the biosciences. *Nature Biotechnology*, 21(11):1369–1377, November 2003.

[14] Peter T. C. So, Chen Y. Dong, Barry R. Masters, and Keith M. Berland. Two-Photon Excitation Fluorescence Microscopy. *Annual Review of Biomedical Engineering*, 2(1):399–429, 2000.

[15] Aikaterini Zoumi, Alvin Yeh, and Bruce J. Tromberg. Imaging cells and extracellular matrix in vivo by using second-harmonic generation and two-photon excited fluorescence. *Proceedings of the National Academy of Sciences*, 99(17):11014–11019, August 2002.

[16] Paul J. Campagnola and Leslie M. Loew. Second-harmonic imaging microscopy for visualizing biomolecular arrays in cells, tissues and organisms. *Nature Biotechnology*, 21(11):1356–1360, November 2003.

[17] Sergey V. Plotnikov, Andrew C. Millard, Paul J. Campagnola, and William A. Mohler. Characterization of the Myosin-Based Source for Second-Harmonic Generation from Muscle Sarcomeres. *Biophysical Journal*, 90(2):693–703, January 2006.

[18] Daniel A. Dombeck, Karl A. Kasischke, Harshad D. Vishwasrao, Martin Ingelsson, Bradley T. Hyman, and Watt W. Webb. Uniform polarity microtubule assemblies imaged in native brain tissue by second-harmonic generation microscopy. *Proceedings of the National Academy of Sciences*, 100(12):7081–7086, June 2003.

[19] Warren R. Zipfel, Rebecca M. Williams, Richard Christie, Alexander Yu Nikitin, Bradley T. Hyman, and Watt W. Webb. Live tissue intrinsic emission microscopy using multiphoton-excited native fluorescence and second harmonic generation. *Proceedings of the National Academy of Sciences*, 100(12):7075–7080, June 2003.

[20] P. J. Campagnola and C.-Y. Dong. Second harmonic generation microscopy: Principles and applications to disease diagnosis. *Laser & Photonics Reviews*, 5(1):13–26, January 2011.

[21] Y. Barad, H. Eisenberg, M. Horowitz, and Y. Silberberg. Nonlinear scanning laser microscopy by third harmonic generation. *Applied Physics Letters*, 70(8):922–924, February 1997.

[22] Jeff A. Squier, Michiel Müller, G. J. Brakenhoff, and Kent R. Wilson. Third harmonic generation microscopy. *Optics Express*, 3(9):315–324, October 1998.

[23] Müller, Squier, Wilson, and Brakenhoff. 3D microscopy of transparent objects using third-harmonic generation. *Journal of Microscopy*, 191(3):266–274, September 1998.

[24] Delphine Débarre, Nicolas Olivier, Willy Supatto, and Emmanuel Beaurepaire. Mitigating Phototoxicity during Multiphoton Microscopy of Live Drosophila Embryos in the 1.0–1.2 mm Wavelength Range. *PLOS ONE*, 9(8):e104250, August 2014.

[25] Rachel Genthial, Emmanuel Beaurepaire, Marie-Claire Schanne-Klein, Françoise Peyrin, Delphine Farlay, Cécile Olivier, Yohann Bala, Georges Boivin, Jean-Claude Vial, Delphine Débarre, and Aurélien Gourrier. Label-free imaging of bone multiscale porosity and interfaces using third-harmonic generation microscopy. *Scientific Reports*, 7(1):3419, June 2017.

[26] Chi-Kuang Sun, Shi-Wei Chu, Szu-Yu Chen, Tsung-Han Tsai, Tzu-Ming Liu, Chung-Yung Lin, and Huai-Jen Tsai. Higher harmonic generation microscopy for developmental biology. *Journal of Structural Biology*, 147(1):19–30, July 2004.

[27] Stefan Witte, Adrian Negrean, Johannes C. Lodder, Christiaan P. J. de Kock, Guilherme Testa Silva, Huibert D. Mansvelder, and Marie Louise Groot. Label-free live brain imaging and targeted patching with third-harmonic generation microscopy. *Proceedings of the National Academy of Sciences*, 108(15):5970–5975, April 2011.

[28] George J. Tserevelakis, Evgenia V. Megalou, George Filippidis, Barbara Petanidou, Costas Fotakis, and Nektarios Tavernarakis. Label-Free Imaging of Lipid Depositions in C. elegans Using Third-Harmonic Generation Microscopy. *PLOS ONE*, 9(1):e84431, January 2014.

[29] S. Witte, S. Witte, N. V. Kuzmin, N. V. Kuzmin, A. Negrean, A. Negrean, A. Negrean, J. C. Lodder, J. C. Lodder, G. T. Silva, G. T. Silva, C. P. J. de Kock, C. P. J. de Kock, H. D. Mansvelder, H. D. Mansvelder, M. L. Groot, and M. L. Groot. Third-Harmonic Generation Microscopy For Label-Free Brain Imaging. In *Biomedical Optics and 3-D Imaging (2012), Paper BSu4B.4*, page BSu4B.4. Optical Society of America, April 2012.

[30] N. V. Kuzmin, P. Wesseling, P. C. de Witt Hamer, D. P. Noske, G. D. Galgano, H. D. Mansvelder, J. C. Baayen, and M. L. Groot. Third harmonic generation imaging for fast,

label-free pathology of human brain tumors. *Biomedical Optics Express*, 7(5):1889–1904, May 2016.

[31] Shih-Hsuan Chia, Che-Hang Yu, Chih-Han Lin, Nai-Chia Cheng, Tzu-Ming Liu, Ming-Che Chan, I.-Hsiu Chen, and Chi-Kuang Sun. Miniaturized video-rate epi-third-harmonic-generation fiber-microscope. *Optics Express*, 18(16):17382–17391, August 2010.

[32] Andreas Zumbusch, Gary R. Holtom, and X. Sunney Xie. Three-Dimensional Vibrational Imaging by Coherent Anti-Stokes Raman Scattering. *Physical Review Letters*, 82(20):4142–4145, 1999.

[33] Haim Lotem, R. T. Lynch, and N. Bloembergen. Interference between Raman resonances in four-wave difference mixing. *Physical Review A*, 14(5):1748–1755, November 1976.

[34] Ji-Xin Cheng and Xiaoliang Sunney Xie. *Coherent Raman Scattering Microscopy*. CRC Press, April 2016.

[35] Feruz Ganikhanov, Conor L. Evans, Brian G. Saar, and X. Sunney Xie. High-sensitivity vibrational imaging with frequency modulation coherent anti-Stokes Raman scattering (FM CARS) microscopy. *Optics Letters*, 31(12):1872–1874, June 2006.

[36] Eric O. Potma, Conor L. Evans, and X. Sunney Xie. Heterodyne coherent anti-Stokes Raman scattering (CARS) imaging. *Optics Letters*, 31(2):241–243, January 2006.

[37] Andreas Volkmer, Lewis D. Book, and X. Sunney Xie. Time-resolved coherent anti-Stokes Raman scattering microscopy: Imaging based on Raman free induction decay. *Applied Physics Letters*, 80(9):1505–1507, February 2002.

[38] Ji-Xin Cheng, Lewis D. Book, and X. Sunney Xie. Polarization coherent anti-Stokes Raman scattering microscopy. *Optics Letters*, 26(17):1341–1343, September 2001.

[39] Chi Zhang and Ji-Xin Cheng. Perspective: Coherent Raman scattering microscopy, the future is bright. *APL Photonics*, 3(9):090901, July 2018.

[40] R. Paschotta. Article on 'propagation constant' in the Encyclopedia of Laser Physics and Technology, 1. edition, Wiley-VCH,. October 2008.

[41] G.P. Agrawal. Nonlinear Fiber Optics, 5th edn. https://www.abebooks.co.uk/book-search/title/nonlinear-fiber-optics/author/agrawal-govind-p/, 2012.

[42] L. F. Mollenauer, R. H. Stolen, and J. P. Gordon. Experimental Observation of Picosecond Pulse Narrowing and Solitons in Optical Fibers. *Physical Review Letters*, 45(13):1095–1098, September 1980.

[43] Sarah Saint-Jalm, Esben R. Andresen, Patrick Ferrand, Abdelkrim Bendahmane, Arnaud Mussot, Olivier Vanvincq, Géraud Bouwmans, Alexandre Kudlinski, and Hervé Rigneault. Fiber-based ultrashort pulse delivery for nonlinear imaging using high-energy solitons. *Journal of Biomedical Optics*, 19(8):086021, August 2014.

[44] F. Luan, J. C. Knight, P. St J. Russell, S. Campbell, D. Xiao, D. T. Reid, B. J. Mangan, D. P. Williams, and P. J. Roberts. Femtosecond soliton pulse delivery at 800nm wavelength in hollow-core photonic bandgap fibers. *Optics Express*, 12(5):835–840, March 2004.

[45] Charles H. Camp Jr and Marcus T. Cicerone. Chemically sensitive bioimaging with coherent Raman scattering. *Nature Photonics*, 9(5):295–305, May 2015.

[46] Ji-Xin Cheng and X. Sunney Xie. Vibrational spectroscopic imaging of living systems: An emerging platform for biology and medicine. *Science (New York, N.Y.)*, 350(6264):aaa8870, November 2015.

[47] L. Gao, F. Li, M. J. Thrall, Y. Yang, J. Xing, A. A. Hammoudi, H. Zhao, Y. Massoud, P. T. Cagle, Y. Fan, K. K. Wong, Z. Wang, and S. T. Wong. On-the-spot lung cancer differential diagnosis by label-free, molecular vibrational imaging and knowledge-based classification. *Journal of biomedical optics*, 16(9):096004–096004, September 2011.

[48] Minbiao Ji, Spencer Lewis, Sandra Camelo-Piragua, Shakti H. Ramkissoon, Matija Snuderl, Sriram Venneti, Amanda Fisher-Hubbard, Mia Garrard, Dan Fu, Anthony C. Wang, Jason A. Heth, Cormac O. Maher, Nader Sanai, Timothy D. Johnson, Christian W. Freudiger, Oren Sagher, Xiaoliang Sunney Xie, and Daniel A. Orringer. Detection of human brain tumor infiltration with quantitative stimulated Raman scattering microscopy. *Science translational medicine*, 7(309):309ra163, October 2015.

[49] Daniel A. Orringer, Balaji Pandian, Yashar S. Niknafs, Todd C. Hollon, Julianne Boyle, Spencer Lewis, Mia Garrard, Shawn L. Hervey-Jumper, Hugh J. L. Garton, Cormac O. Maher, Jason A. Heth, Oren Sagher, D. Andrew Wilkinson, Matija Snuderl, Sriram Venneti, Shakti H. Ramkissoon, Kathryn A. McFadden, Amanda Fisher-Hubbard, Andrew P. Lieberman, Timothy D. Johnson, X. Sunney Xie, Jay K. Trautman, Christian W. Freudiger, and Sandra Camelo-Piragua. Rapid intraoperative histology of unprocessed surgical specimens via fibre-laser-based stimulated Raman scattering microscopy. *Nature Biomedical Engineering*, 1(2):0027, February 2017.

[50] Fritjof Helmchen and Winfried Denk. Deep tissue two-photon microscopy. *Nature Methods*, 2(12):932–940, December 2005.

[51] Mihaela Balu, Gangjun Liu, Zhongping Chen, Bruce J. Tromberg, and Eric O. Potma. Fiber delivered probe for efficient CARS imaging of tissues. *Optics Express*, 18(3):2380–2388, February 2010.

[52] Xu Chen, Xiaoyun Xu, Daniel T. McCormick, Kelvin Wong, and Stephen T. C. Wong. Multimodal nonlinear endo-microscopy probe design for high resolution, label-free intra-operative imaging. *Biomedical Optics Express*, 6(7):2283–2293, July 2015.

[53] Pascal Deladurantaye, Alex Paquet, Claude Paré, Huimin Zheng, Michel Doucet, David Gay, Michel Poirier, Jean-François Cormier, Ozzy Mermut, Brian C. Wilson, and Eric J. Seibel. Advances in engineering of high contrast CARS imaging endoscopes. *Optics Express*, 22(21):25053–25064, October 2014.

[54] François Légaré, Conor L. Evans, Feruz Ganikhanov, and X. S. Xie. Towards CARS Endoscopy. *Optics Express*, 14(10):4427–4432, May 2006.

[55] Aleksandar Lukic, Sebastian Dochow, Hyeonsoo Bae, Gregor Matz, Ines Latka, Bernhard Messerschmidt, Michael Schmitt, and Jürgen Popp. Endoscopic fiber probe for nonlinear spectroscopic imaging. *Optica*, 4(5):496–501, May 2017.

[56] Brian G. Saar, Richard S. Johnston, Christian W. Freudiger, X. Sunney Xie, and Eric J. Seibel. Coherent Raman scanning fiber endoscopy. *Optics letters*, 36(13):2396–2398, July 2011.

[57] Brett Smith, Majid Naji, Sangeeta Murugkar, Emilio Alarcon, Craig Brideau, Peter Stys, and Hanan Anis. Portable, miniaturized, fibre delivered, multimodal CARS exoscope. *Optics Express*, 21(14):17161–17175, July 2013.

[58] Benjamin A. Flusberg, Eric D. Cocker, Wibool Piyawattanametha, Juergen C. Jung, Eunice L. M. Cheung, and Mark J. Schnitzer. Fiber-optic fluorescence imaging. *Nature Methods*, 2(12):941–950, December 2005.

[59] David R. Rivera, Christopher M. Brown, Dimitre G. Ouzounov, Watt W. Webb, and Chris Xu. Use of a lensed fiber for a large-field-of-view, high-resolution, fiber-scanning microendoscope. *Optics Letters*, 37(5):881–883, March 2012.

[60] Wenxuan Liang, Gunnsteinn Hall, Bernhard Messerschmidt, Ming-Jun Li, and Xingde Li. Nonlinear optical endomicroscopy for label-free functional histology *in vivo*. *Light: Science & Applications*, 6(11):e17082, November 2017.

[61] P. Zirak, G. Matz, B. Messerschmidt, T. Meyer, M. Schmitt, J. Popp, O. Uckermann, R. Galli, M. Kirsch, M. J. Winterhalder, and A. Zumbusch. Invited Article: A rigid coherent anti-Stokes Raman scattering endoscope with high resolution and a large field of view. *APL Photonics*, 3(9):092409, August 2018.

[62] Eric J. Seibel and Quinn Y. J. Smithwick. Unique features of optical scanning, single fiber endoscopy***. *Lasers in Surgery and Medicine*, 30(3):177–183, March 2002.

[63] Guillaume Ducourthial, Pierre Leclerc, Tigran Mansuryan, Marc Fabert, Julien Brevier, Rémi Habert, Flavie Braud, Renaud Batrin, Christine Vever-Bizet, Geneviève Bourg-Heckly, Luc Thiberville, Anne Druilhe, Alexandre Kudlinski, and Frédéric Louradour. Development of a real-time flexible multiphoton microendoscope for label-free imaging in a live animal. *Scientific Reports*, 5:18303, December 2015.

[64] Yuying Zhang, Meredith L. Akins, Kartikeya Murari, Jiefeng Xi, Ming-Jun Li, Katherine Luby-Phelps, Mala Mahendroo, and Xingde Li. A compact fiber-optic SHG scanning endomicroscope and its application to visualize cervical remodeling during pregnancy. *Proceedings of the National Academy of Sciences*, 109(32):12878–12883, August 2012.

[65] Youbo Zhao, Hiroshi Nakamura, and Robert J. Gordon. Development of a versatile two-photon endoscope for biological imaging. *Biomedical Optics Express*, 1(4):1159–1172, November 2010.

[66] Cameron M. Lee, Christoph J. Engelbrecht, Timothy D. Soper, Fritjof Helmchen, and Eric J. Seibel. Scanning fiber endoscopy with highly flexible, 1 mm catheterscopes for wide-field, full-color imaging. *Journal of Biophotonics*, 3(5-6):385–407, June 2010.

[67] Mon Thiri Myaing, Daniel J. MacDonald, and Xingde Li. Fiber-optic scanning two-photon fluorescence endoscope. *Optics Letters*, 31(8):1076–1078, April 2006.

[68] Yicong Wu, Yuxin Leng, Jiefeng Xi, and Xingde Li. Scanning all-fiber-optic endomicroscopy system for 3D nonlinear optical imaging of biological tissues. *Optics Express*, 17(10):7907–7915, May 2009.

[69] Alberto Lombardini. Thesis: "Nonlinear optical endoscopy with microstructured photonic crystal fibers", 2016.

[70] K. Hirose, T. Aoki, T. Furukawa, S. Fukushima, H. Niioka, S. Deguchi, and M. Hashimoto. Coherent anti-Stokes Raman scattering rigid endoscope toward robot-assisted surgery. *Biomedical Optics Express*, 9(2):387–396, February 2018.

[71] Thomas Stone and Nicholas George. Hybrid diffractive-refractive lenses and achromats. *Applied Optics*, 27(14):2960–2971, July 1988.

[72] Sangeeta Murugkar, Brett Smith, Prateek Srivastava, Adrian Moica, Majid Naji, Craig Brideau, Peter K. Stys, and Hanan Anis. Miniaturized multimodal CARS microscope based on MEMS scanning and a single laser source. *Optics Express*, 18(23):23796–23804, November 2010.

[73] Richa Mittal, Mihaela Balu, Petra Wilder-Smith, and Eric O. Potma. Achromatic miniature lens system for coherent Raman scattering microscopy. *Biomedical Optics Express*, 4(10):2196–2206, October 2013.

[74] T. A. Birks, P. J. Roberts, P. S. J. Russell, D. M. Atkin, and T. J. Shepherd. Full 2-D photonic bandgaps in silica/air structures. *Electronics Letters*, 31(22):1941–1943, October 1995.

[75] R. F. Cregan, B. J. Mangan, J. C. Knight, T. A. Birks, P. St J. Russell, P. J. Roberts, and D. C. Allan. Single-Mode Photonic Band Gap Guidance of Light in Air. *Science*, 285(5433):1537–1539, September 1999.

[76] P. J. Roberts, F. Couny, H. Sabert, B. J. Mangan, D. P. Williams, L. Farr, M. W. Mason, A. Tomlinson, T. A. Birks, J. C. Knight, and P. St J. Russell. Ultimate low loss of hollow-core photonic crystal fibres. *Optics Express*, 13(1):236–244, January 2005.

[77] Natalie V. Wheeler, Alexander M. Heidt, Naveen K. Baddela, Eric Numkam Fokoua, John R. Hayes, Seyed R. Sandoghchi, Francesco Poletti, Marco N. Petrovich, and David J. Richardson. Low-loss and low-bend-sensitivity mid-infrared guidance in a hollow-core–photonic-bandgap fiber. *Optics Letters*, 39(2):295–298, January 2014.

[78] Y. Y. Wang, N. V. Wheeler, F. Couny, P. J. Roberts, and F. Benabid. Low loss broadband transmission in hypocycloid-core Kagome hollow-core photonic crystal fiber. *Optics Letters*, 36(5):669–671, March 2011.

[79] F. Couny, F. Benabid, and P. S. Light. Large-pitch kagome-structured hollow-core photonic crystal fiber. *Optics Letters*, 31(24):3574–3576, December 2006.

[80] F. Poletti, J. R. Hayes, and D. J. Richardson. Optimising the Performances of Hollow Antiresonant Fibres. In *37th European Conference and Exposition on Optical Communications (2011), Paper Mo.2.LeCervin.2*, page Mo.2.LeCervin.2. Optical Society of America, September 2011.

[81] Francesco Poletti. Nested antiresonant nodeless hollow core fiber. *Optics Express*, 22(20):23807–23828, October 2014.

[82] Conor L. Evans, Xiaoyin Xu, Santosh Kesari, X. Sunney Xie, Stephen T. C. Wong, and Geoffrey S. Young. Chemically-selective imaging of brain structures with CARS microscopy. *Optics Express*, 15(19):12076–12087, September 2007.

[83] Conor L. Evans and X. Sunney Xie. Coherent anti-stokes Raman scattering microscopy: Chemical imaging for biology and medicine. *Annual Review of Analytical Chemistry (Palo Alto, Calif.)*, 1:883–909, 2008.

[84] Xiaoyun Xu, Jie Cheng, Michael J. Thrall, Zhengfan Liu, Xi Wang, and Stephen T. C. Wong. Multimodal non-linear optical imaging for label-free differentiation of lung cancerous lesions from normal and desmoplastic tissues. *Biomedical Optics Express*, 4(12):2855–2868, December 2013.

[85] B. Debord, A. Amsanpally, M. Chafer, A. Baz, M. Maurel, J. M. Blondy, E. Hugonnot, F. Scol, L. Vincetti, F. Gérôme, and F. Benabid. Ultralow transmission loss in inhibited-coupling guiding hollow fibers. *Optica*, 4(2):209–217, February 2017.

[86] Piotr Jaworski, Fei Yu, Robert R. J. Maier, William J. Wadsworth, Jonathan C. Knight, Jonathan D. Shephard, and Duncan P. Hand. Picosecond and nanosecond pulse delivery through a hollow-core Negative Curvature Fiber for micro-machining applications. *Optics Express*, 21(19):22742–22753, September 2013.

[87] Andrey D. Pryamikov, Alexander S. Biriukov, Alexey F. Kosolapov, Victor G. Plotnichenko, Sergei L. Semjonov, and Evgeny M. Dianov. Demonstration of a waveguide regime for a silica hollow - core microstructured optical fiber with a negative curvature of the core boundary in the spectral region > 3.5 mm. *Optics Express*, 19(2):1441–1448, January 2011.

[88] Fei Yu, William J. Wadsworth, and Jonathan C. Knight. Low loss silica hollow core fibers for 3–4 mm spectral region. *Optics Express*, 20(10):11153–11158, May 2012.

[89] Anton N. Kolyadin, Alexey F. Kosolapov, Andrey D. Pryamikov, Alexander S. Biriukov, Victor G. Plotnichenko, and Evgeny M. Dianov. Light transmission in negative curvature hollow core fiber in extremely high material loss region. *Optics Express*, 21(8):9514–9519, April 2013.

[90] M. A. Duguay, Y. Kokubun, T. L. Koch, and Loren Pfeiffer. Antiresonant reflecting optical waveguides in SiO2-Si multilayer structures. *Applied Physics Letters*, 49(1):13–15, July 1986.

[91] Y. Kokubun, T. Baba, T. Sakaki, and K. Iga. Low-loss antiresonant reflecting optical waveguide on Si substrate in visible-wavelength region. *Electronics Letters*, 22(17):892–893, August 1986.

[92] F. Couny, F. Benabid, P. J. Roberts, P. S. Light, and M. G. Raymer. Generation and Photonic Guidance of Multi-Octave Optical-Frequency Combs. *Science*, 318(5853):1118–1121, November 2007.

[93] Frédéric Gérôme, Raphaël Jamier, Jean-Louis Auguste, Georges Humbert, and Jean-Marc Blondy. Simplified hollow-core photonic crystal fiber. *Optics Letters*, 35(8):1157–1159, April 2010.

[94] B. Debord, M. Alharbi, T. Bradley, C. Fourcade-Dutin, Y. Y. Wang, L. Vincetti, F. Gérôme, and F. Benabid. Hypocycloid-shaped hollow-core photonic crystal fiber Part I: Arc curvature effect on confinement loss. *Optics Express*, 21(23):28597–28608, November 2013.

[95] Alexey F. Kosolapov, Andrey D. Pryamikov, Alexander S. Biriukov, Vladimir S. Shiryaev, Maxim S. Astapovich, Gennady E. Snopatin, Victor G. Plotnichenko, Mikhail F. Churbanov, and Evgeny M. Dianov. Demonstration of CO_2-laser power delivery through chalcogenide-glass fiber with negative-curvature hollow core. *Optics Express*, 19(25):25723–25728, December 2011.

[96] Vladimir S. Shiryaev. Chalcogenide Glass Hollow-Core Microstructured Optical Fibers. *Frontiers in Materials*, 2, 2015.

[97] Xin Jiang, Nicolas Y. Joly, Martin A. Finger, Fehim Babic, Gordon K. L. Wong, John C. Travers, and Philip St J. Russell. Deep-ultraviolet to mid-infrared supercontinuum generated in solid-core ZBLAN photonic crystal fibre. *Nature Photonics*, 9(2):133–139, February 2015.

[98] J. H. V. Price, T. M. Monro, H. Ebendorff-Heidepriem, F. Poletti, P. Horak, V. Finazzi, J. Y. Y. Leong, P. Petropoulos, J. C. Flanagan, G. Brambilla, X. Feng, and D. J. Richardson. Mid-IR Supercontinuum Generation From Nonsilica Microstructured Optical Fibers. *IEEE Journal of Selected Topics in Quantum Electronics*, 13(3):738–749, May 2007.

[99] Ben Sherlock, Fei Yu, Jim Stone, Sean Warren, Carl Paterson, Mark A. A. Neil, Paul M. W. French, Jonathan Knight, and Chris Dunsby. Tunable fibre-coupled multiphoton microscopy with a negative curvature fibre. *Journal of Biophotonics*, 9(7):715–720, July 2016.

[100] Maciej Andrzej Popenda, Hanna Izabela Stawska, Leszek Mateusz Mazur, Konrad Jakubowski, Alexey Kosolapov, Anton Kolyadin, and Elżbieta Bereś-Pawlik. Application of Negative Curvature Hollow-Core Fiber in an Optical Fiber Sensor Setup for Multiphoton Spectroscopy. *Sensors (Basel, Switzerland)*, 17(10), October 2017.

[101] A. Urich, R. R. J. Maier, Fei Yu, J. C. Knight, D. P. Hand, and J. D. Shephard. Flexible delivery of radiation at 2.94 mm with negative curvature silica glass fibers: A new solution for minimally invasive surgical procedures. *Biomedical Optics Express*, 4(2):193–205, February 2013.

[102] Chengli Wei, R. Joseph Weiblen, Curtis R. Menyuk, and Jonathan Hu. Negative curvature fibers. *Advances in Optics and Photonics*, 9(3):504–561, September 2017.

[103] Vincent Villette, Arnaud Malvache, Thomas Tressard, Nathalie Dupuy, and Rosa Cossart. Internally Recurring Hippocampal Sequences as a Population Template of Spatiotemporal Information. *Neuron*, 88(2):357–366, October 2015.

[104] Mattia Michieletto, Jens K. Lyngsø, Christian Jakobsen, Jesper Lægsgaard, Ole Bang, and Thomas T. Alkeskjold. Hollow-core fibers for high power pulse delivery. *Optics Express*, 24(7):7103–7119, April 2016.

[105] Chengli Wei, Robinson A. Kuis, Francois Chenard, Curtis R. Menyuk, and Jonathan Hu. Higher-order mode suppression in chalcogenide negative curvature fibers. *Optics Express*, 23(12):15824–15832, June 2015.

[106] Pierre Leclerc. Thèse: "Développement d'un endomicroscope multiphotonique à deux couleurs pour l'imagerie du métabolisme énergétique cellulaire", 2017.

[107] Eric J. Seibel, Richard S. Johnston, and C. David Melville. A full-color scanning fiber endoscope. In *Optical Fibers and Sensors for Medical Diagnostics and Treatment Applications VI*, volume 6083, page 608303. International Society for Optics and Photonics, February 2006.

[108] Matthew J. Kundrat, Per G. Reinhall, and Eric J. Seibel. Method to Achieve High Frame Rates in a Scanning Fiber Endoscope. *Journal of Medical Devices*, 5(3):034501–034501–5, August 2011.

[109] Guillaume Ducourthial. Thèse: Développement d'un endomicroscope multiphotonique compact et flexible pour l'imagerie in vivo haute résolution de tissus biologiques non marqués., 2014.

[110] Patrick Ferrand. GPScan.VI: A general-purpose LabVIEW program for scanning imaging or any application requiring synchronous analog voltage generation and data acquisition. *Computer Physics Communications*, 192:342, March 2015.

[111] Paulo André, Ana Rocha, Fátima Domingues, and Margarida Facão. Thermal Effects in Optical Fibres. *Developments in Heat Transfer*, 2011.

[112] David J. Desilets, Subhas Banerjee, Bradley A. Barth, Vivek Kaul, Sripathi R. Kethu, Marcos C. Pedrosa, Patrick R. Pfau, Jeffrey L. Tokar, Shyam Varadarajulu, Amy Wang, Louis-Michel Wong Kee Song, and Sarah A. Rodriguez. Endoscopic simulators. *Gastrointestinal Endoscopy*, 73(5):861–867, May 2011.

[113] J. O'Keefe and J. Dostrovsky. The hippocampus as a spatial map. Preliminary evidence from unit activity in the freely-moving rat. *Brain Research*, 34(1):171–175, November 1971.

[114] Massimo Scanziani and Michael Häusser. Electrophysiology in the age of light. *Nature*, 461(7266):930–939, October 2009.

[115] Brian A. Wilt, Laurie D. Burns, Eric Tatt Wei Ho, Kunal K. Ghosh, Eran A. Mukamel, and Mark J. Schnitzer. Advances in light microscopy for neuroscience. *Annual Review of Neuroscience*, 32:435–506, 2009.

[116] Daniel A. Dombeck, Christopher D. Harvey, Lin Tian, Loren L. Looger, and David W. Tank. Functional imaging of hippocampal place cells at cellular resolution during virtual navigation. *Nature Neuroscience*, 13(11):1433–1440, November 2010.

[117] Masashi Kondo, Kenta Kobayashi, Masamichi Ohkura, Junichi Nakai, and Masanori Matsuzaki. Two-photon calcium imaging of the medial prefrontal cortex and hippocampus without cortical invasion. *eLife*, 6, 09 25, 2017.

[118] Nicholas G. Horton, Ke Wang, Demirhan Kobat, Catharine G. Clark, Frank W. Wise, Chris B. Schaffer, and Chris Xu. In vivo three-photon microscopy of subcortical structures within an intact mouse brain. *Nature photonics*, 7(3):205–209, March 2013.

[119] Guosong Hong, Shuo Diao, Junlei Chang, Alexander L. Antaris, Changxin Chen, Bo Zhang, Su Zhao, Dmitriy N. Atochin, Paul L. Huang, Katrin I. Andreasson, Calvin J. Kuo, and Hongjie Dai. Through-skull fluorescence imaging of the brain in a new near-infrared window. *Nature Photonics*, 8(9):723–730, September 2014.

[120] Jasper Akerboom, Nicole Carreras Calderón, Lin Tian, Sebastian Wabnig, Matthias Prigge, Johan Tolö, Andrew Gordus, Michael B. Orger, Kristen E. Severi, John J. Macklin, Ronak Patel, Stefan R. Pulver, Trevor J. Wardill, Elisabeth Fischer, Christina Schüler, Tsai-Wen Chen, Karen S. Sarkisyan, Jonathan S. Marvin, Cornelia I. Bargmann, Douglas S. Kim, Sebastian Kügler, Leon Lagnado, Peter Hegemann, Alexander Gottschalk, Eric R. Schreiter, and Loren L. Looger. Genetically encoded calcium indicators for multi-color neural activity imaging and combination with optogenetics. *Frontiers in Molecular Neuroscience*, 6, March 2013.

[121] Dimitre G. Ouzounov, Tianyu Wang, Mengran Wang, Danielle D. Feng, Nicholas G. Horton, Jean C. Cruz-Hernández, Yu-Ting Cheng, Jacob Reimer, Andreas S. Tolias, Nozomi Nishimura, and Chris Xu. In vivo three-photon imaging of activity of GCaMP6-labeled neurons deep in intact mouse brain. *Nature Methods*, 14(4):388–390, April 2017.

[122] Khmaies Guesmi, Lamiae Abdeladim, Samuel Tozer, Pierre Mahou, Takuma Kumamoto, Karolis Jurkus, Philippe Rigaud, Karine Loulier, Nicolas Dray, Patrick Georges, Marc Hanna, Jean Livet, Willy Supatto, Emmanuel Beaurepaire, and Frédéric Druon. Dual-color deep-tissue three-photon microscopy with a multiband infrared laser. *Light: Science & Applications*, 7(1):12, June 2018.

[123] Baris N. Ozbay, Gregory L. Futia, Ming Ma, Victor M. Bright, Juliet T. Gopinath, Ethan G. Hughes, Diego Restrepo, and Emily A. Gibson. Three dimensional two-photon brain imaging in freely moving mice using a miniature fiber coupled microscope with active axial-scanning. *Scientific Reports*, 8(1):8108, May 2018.

[124] Vasilis Ntziachristos. Going deeper than microscopy: The optical imaging frontier in biology. *Nature Methods*, 7(8):603–614, August 2010.

[125] Allard P. Mosk, Ad Lagendijk, Geoffroy Lerosey, and Mathias Fink. Controlling waves in space and time for imaging and focusing in complex media. *Nature Photonics*, 6(5):283–292, May 2012.

[126] Juergen C. Jung and Mark J. Schnitzer. Multiphoton endoscopy. *Optics Letters*, 28(11):902–904, June 2003.

[127] Michael J. Levene, Daniel A. Dombeck, Karl A. Kasischke, Raymond P. Molloy, and Watt W. Webb. In vivo multiphoton microscopy of deep brain tissue. *Journal of Neurophysiology*, 91(4):1908–1912, April 2004.

[128] Benjamin A. Flusberg, Axel Nimmerjahn, Eric D. Cocker, Eran A. Mukamel, Robert P. J. Barretto, Tony H. Ko, Laurie D. Burns, Juergen C. Jung, and Mark J. Schnitzer. High-speed, miniaturized fluorescence microscopy in freely moving mice. *Nature Methods*, 5(11):935–938, November 2008.

[129] Kunal K. Ghosh, Laurie D. Burns, Eric D. Cocker, Axel Nimmerjahn, Yaniv Ziv, Abbas El Gamal, and Mark J. Schnitzer. Miniaturized integration of a fluorescence microscope. *Nature Methods*, 8(10):871–878, September 2011.

[130] Yaniv Ziv, Laurie D. Burns, Eric D. Cocker, Elizabeth O. Hamel, Kunal K. Ghosh, Lacey J. Kitch, Abbas El Gamal, and Mark J. Schnitzer. Long-term dynamics of CA1 hippocampal place codes. *Nature Neuroscience*, 16(3):264–266, March 2013.

[131] Joshua H. Jennings, Randall L. Ung, Shanna L. Resendez, Alice M. Stamatakis, Johnathon G. Taylor, Jonathan Huang, Katie Veleta, Pranish A. Kantak, Megumi Aita, Kelson Shilling-Scrivo, Charu Ramakrishnan, Karl Deisseroth, Stephani Otte, and Garret D. Stuber. Visualizing hypothalamic network dynamics for appetitive and consummatory behaviors. *Cell*, 160(3):516–527, January 2015.

[132] J. Nicholas Betley, Shengjin Xu, Zhen Fang Huang Cao, Rong Gong, Christopher J. Magnus, Yang Yu, and Scott M. Sternson. Neurons for hunger and thirst transmit a negative-valence teaching signal. *Nature*, 521(7551):180–185, May 2015.

[133] Teruhiro Okuyama, Takashi Kitamura, Dheeraj S. Roy, Shigeyoshi Itohara, and Susumu Tonegawa. Ventral CA1 neurons store social memory. *Science (New York, N.Y.)*, 353(6307):1536–1541, 09 30, 2016.

[134] Yaniv Ziv and Kunal K. Ghosh. Miniature microscopes for large-scale imaging of neuronal activity in freely behaving rodents. *Current Opinion in Neurobiology*, 32:141–147, June 2015.

[135] Weijian Zong, Runlong Wu, Mingli Li, Yanhui Hu, Yijun Li, Jinghang Li, Hao Rong, Haitao Wu, Yangyang Xu, Yang Lu, Hongbo Jia, Ming Fan, Zhuan Zhou, Yunfeng Zhang, Aimin Wang, Liangyi Chen, and Heping Cheng. Fast high-resolution miniature two-photon microscopy for brain imaging in freely behaving mice. *Nature Methods*, 14(7):713–719, July 2017.

[136] Jérôme Lecoq, Joan Savall, Dejan Vučinić, Benjamin F. Grewe, Hyun Kim, Jin Zhong Li, Lacey J. Kitch, and Mark J. Schnitzer. Visualizing mammalian brain area interactions by dual-axis two-photon calcium imaging. *Nature Neuroscience*, 17(12):1825–1829, December 2014.

[137] J. Sawinski, D. J. Wallace, D. S. Greenberg, Denk Grossmann S, and J. N. D. Kerr. Visually evoked activity in cortical cells imaged in freely moving animals. *Proceedings of the National Academy of Sciences of the United States of America*, 106(46):19557–19562, November 2009.

[138] Pascal Ravassard, Ashley Kees, Bernard Willers, David Ho, Daniel A. Aharoni, Jesse Cushman, Zahra M. Aghajan, and Mayank R. Mehta. Multisensory control of hippocampal spatiotemporal selectivity. *Science (New York, N.Y.)*, 340(6138):1342–1346, June 2013.

[139] Zahra M. Aghajan, Lavanya Acharya, Jason J. Moore, Jesse D. Cushman, Cliff Vuong, and Mayank R. Mehta. Impaired spatial selectivity and intact phase precession in two-dimensional virtual reality. *Nature Neuroscience*, 18(1):121–128, January 2015.

[140] Ramin Khayatzadeh, Fehmi Civitci, Onur Ferhanoglu, and Hakan Urey. Scanning fiber microdisplay: Design, implementation, and comparison to MEMS mirror-based scanning displays. *Optics Express*, 26(5):5576–5590, March 2018.

[141] Junichi Nakai, Masamichi Ohkura, and Keiji Imoto. A high signal-to-noise Ca^{2+} probe composed of a single green fluorescent protein. *Nature Biotechnology*, 19(2):137–141, February 2001.

[142] Alberto Lombardini, Vasyl Mytskaniuk, Siddharth Sivankutty, Esben Ravn Andresen, Xueqin Chen, Jérôme Wenger, Marc Fabert, Nicolas Joly, Frédéric Louradour, Alexandre

Kudlinski, and Hervé Rigneault. High-resolution multimodal flexible coherent Raman endoscope. *Light: Science & Applications*, 7(1):10, May 2018.

[143] D. Champelovier. Thèse: Développement d'un microscope bi-photon à front d'onde optimisé pour l'imagerie calcique profonde dans le cerveau de souris., 2016.

[144] Hod Dana, Tsai-Wen Chen, Amy Hu, Brenda C. Shields, Caiying Guo, Loren L. Looger, Douglas S. Kim, and Karel Svoboda. Thy1-GCaMP6 transgenic mice for neuronal population imaging in vivo. *PloS One*, 9(9):e108697, 2014.

[145] Lin Tian, S. Andrew Hires, Tianyi Mao, Daniel Huber, M. Eugenia Chiappe, Sreekanth H. Chalasani, Leopoldo Petreanu, Jasper Akerboom, Sean A. McKinney, Eric R. Schreiter, Cornelia I. Bargmann, Vivek Jayaraman, Karel Svoboda, and Loren L. Looger. Imaging neural activity in worms, flies and mice with improved GCaMP calcium indicators. *Nature methods*, 6(12):875–881, December 2009.

[146] Masamichi Ohkura, Takuya Sasaki, Junko Sadakari, Keiko Gengyo-Ando, Yuko Kagawa-Nagamura, Chiaki Kobayashi, Yuji Ikegaya, and Junichi Nakai. Genetically Encoded Green Fluorescent Ca2+ Indicators with Improved Detectability for Neuronal Ca2+ Signals. *PLoS ONE*, 7(12), December 2012.

[147] Gregor-Alexander Pilz, Stefano Carta, Andreas Stäuble, Asli Ayaz, Sebastian Jessberger, and Fritjof Helmchen. Functional Imaging of Dentate Granule Cells in the Adult Mouse Hippocampus. *Journal of Neuroscience*, 36(28):7407–7414, July 2016.

[148] Vincent Villette, Mathieu Levesque, Amine Miled, Benoit Gosselin, and Lisa Topolnik. Simple platform for chronic imaging of hippocampal activity during spontaneous behaviour in an awake mouse. *Scientific Reports*, 7:43388, February 2017.

[149] Patrick W. Wright, Lindsey M. Brier, Adam Q. Bauer, Grant A. Baxter, Andrew W. Kraft, Matthew D. Reisman, Annie R. Bice, Abraham Z. Snyder, Jin-Moo Lee, and Joseph P. Culver. Functional connectivity structure of cortical calcium dynamics in anesthetized and awake mice. *PLOS ONE*, 12(10):e0185759, October 2017.